

1 Research Paper

2 Patton et al.

3 Submarine Paleoseismology: northern Sumatra

4 GEOSPHERE, v. 11, no. X, p. XXX–XXX

5 doi:10.1130/GES01066.1

6 13 figures; 9 tables; 10 supplemental files

7 CORRESPONDENCE: quakejay@gmail.com

8 CITATION: Patton, J.R., Goldfinger, C., Morey, A.E., Ikehara, K., Romsos, C., Stoner, J.,

9 Djadjadihardja, Y., Udrek, Ardhyastuti, S., Gaffar, E.Z., and Viscaino, A., 2015, A 6500 year
10 earthquake history in the region of the 2004 Sumatra-Andaman subduction zone earthquake:


11 Geosphere, v. 11, no. X, p. XXX–XXX, doi:10.1130/GES01066.1.

12 Received 23 April 2014

13 Revision received 23 June 2015

14 Accepted XX Month 2015

15 Published online XX Month 2015



16 **[[Note: For your supplemental files, please replace any “Appendix S #” language in the files**
17 **with “Supplemental File S#” and if possible, please add the paper’s identifying citation to a**
18 **header in each PDF file. The citation is:** 

19 “Patton, J.R., Goldfinger, C., Morey, A.E., Ikehara, K., Romsos, C., Stoner, J., Djadjadihardja,

20 Y., Udrek, Ardhyastuti, S., Gaffar, E.Z., and Viscaino, A., 2015, A 6500 year earthquake

21 history in the region of the 2004 Sumatra-Andaman subduction zone earthquake: Geosphere, v.

22 11, doi:10.1130/GES01066.1.”]]

23 ¹Supplemental File S1. Core map and core table. Core sites from the 2007 cruise RR0705 are
24 displayed with symbols designating core type and symbol size representing relative core length.
25 Terrestrial paleotsunami and paleoearthquake sites in the 2004 **Sumatra-Andaman subduction**
26 **zone (SASZ)** earthquake region are also displayed. The RR0705 cruise track line is plotted as a
27 blue line. **Shuttle Radar Topography Mission (SRTM)** topography (Smith and Sandwell, 1997)
28 underlies bathymetry provided by our collaborators from the UK, Japan, France, and Germany
29 (Ladage et al., 2006). The Chlieh et al. (2007) slip estimate for the 2004 SASZ **earthquake**, in
30 **centimeters**, is plotted as colored dots; 2004 and 2005 earthquake slip contours are plotted in
31 orange and green, respectively (Chlieh et al., 2008). Historic ruptures (Bilham 005 **["Deleted**
32 **"et al." here to match the reference list.]]**; Malik et al., 2010 **["Malik et al., 2010 is not in the**
33 **reference list. 2011 here instead?]]**)  are plotted in orange outline and labeled in orange. Please
34 visit <http://dx.doi.org/10.1130/GES01066.S1> or the full-text article on www.gsapubs.org to view
35 Supplemental File S1.

36 ²Supplemental File S2. Core geophysics and age control methods. A general overview of core
37 geophysics acquisition methods is **p**resented; **a**ge control methods are discussed. The OxCal code
38 for the regional age model is presented, followed by the output “log” file and a plot of the
39 probability density functions for this age model. Please visit
40 <http://dx.doi.org/10.1130/GES01066.S2> or the full-text article on www.gsapubs.org to view
41 Supplemental File S2.

42 ³Supplemental File S3. Stratigraphic correlations. **(A)** Regional stratigraphic correlations for all
43 cores plotted in **text** Figures 3A and 8. Symbols as in **Figure** 3H. Portions of cores that have
44 repeated section or are not relevant to this study are **in gray**. Correlated turbidites are designated
45 with **T numbers** and correspond to the green tie lines, beginning with the most recent turbidite

46 (2004), T-1. Orange correlation tie lines show correlations of strata that are either sedimentary
47 layers within turbidites or turbidites that do not have T numbers. (B) Core location map for cores
48 plotted in A; cores are plotted as orange dots. The 2004 and 2005 Sumatra-Andaman subduction
49 zone (SASZ) earthquake slip regions (Chlieh et al., 2007, 2008) are outlined and shaded in
50 orange and green, respectively. Inset map shows cores as they relate to historic ruptures and the
51 Island of Sumatra. (C) CHIRP (compressed high-intensity radar pulse) seismic profiles for each
52 core site are plotted. Please visit <http://dx.doi.org/10.1130/GES01066.S3> or the full-text article
53 on www.gsapubs.org to view Supplemental File S3.

54 ⁴Supplemental File S4. Radiocarbon age modeling. OxCal combinations (Bronk Ramsey, 2009a)
55 and single ages used to provide age control for timing of turbidite deposition (Fig. 3). Single ages
56 are calibrated as discussed in text and Supplemental File S2. (A) OxCal output for the regional
57 combine analysis. Age results in this table are direct results from the OxCal code in
58 Supplemental File S2. (B) OxCal output for the single core P_Sequence analyses. Please visit
59 <http://dx.doi.org/10.1130/GES01066.S4> or the full-text article on www.gsapubs.org to view
60 Supplemental File S4.


61 ⁵Supplemental File S5. Low-angle oblique site maps. RR0705 core locations are plotted so that
62 the geomorphology of the core sites can be evaluated with respect to preserved stratigraphy.
63 Depth contours are also plotted. Bathymetry was collected while at sea and also provided by our
64 collaborators from the UK, Japan, France, and Germany (Ladage et al., 2006). (A) Map showing
65 relative locations of cores as orange dots (Supplemental File S1). White scale bar is 50 km. (B–
66 H) Larger scale, low-angle oblique views of core sites (orange dots). Orientation arrows (in
67 white) point in the direction of north and up (vertical). Vertical and horizontal units are in



68 meters. Please visit <http://dx.doi.org/10.1130/GES01066.S5> or the full-text article on
69 www.gsapubs.org to view Supplemental File S5.


70 ⁶Supplemental File S6. Core top observations. Core top observations for cores offshore of
71 northern Sumatra are presented. (A) Cores in the 2004 **Sumatra-Andaman subduction zone**
72 **(SASZ)** earthquake region. (B) Cores in the 2005 SASZ earthquake region. Please visit
73 <http://dx.doi.org/10.1130/GES01066.S6> or the full-text article on www.gsapubs.org to view
74 Supplemental File S6.

75 ⁷Supplemental File S7. Sedimentation rates for cores 96PC, 103PC, 104PC, and 108PC in the
76 2004 **Sumatra-Andaman subduction zone (SASZ)** earthquake region. Please visit
77 <http://dx.doi.org/10.1130/GES01066.S7> or the full-text article on www.gsapubs.org to view
78 Supplemental File S7.

79 ⁸Supplemental File S8. Turbidite classification and correlation standard summary. The turbidite
80 class is presented for each **numbered (T-)** turbidite in each core displayed in Supplemental File
81 S3. The counts of each class 1 and class 2 turbidites are presented. The age model results
82 (Supplemental File S2 and S4A) are presented for each **turbidite number**. The accounting of
83 these turbidite classes, strike length of correlation, thickness for the majority of each core, and
84 notes are presented. The summary of **recurrence interval (RI)** estimates for each time period is
85 displayed. See footnotes for notation. Please visit <http://dx.doi.org/10.1130/GES01066.S8> or the
86 full-text article on www.gsapubs.org to view Supplemental File S8.

87 ⁹Supplemental File S9. **Core [c****ct?]** 96PC/TC and 26 December 2004 Sumatra-Andaman
88 subduction zone earthquake seismologic observations. (A) Cores 96PC and 96TC are plotted as
89 in **Figure 5**. (B) Core 96TC is scaled to 96PC and graphically spliced above 96PC to generate
90 this composite core 96PC-96TC. Moment release (vs. latitude) in red (Chlieh et al., 2007) and

91 relative amplitude (vs. time) in green (Ishii et al., 2007), brown (Ni et al., 2005  et al., 2005 is
92 **not in the reference list.**]), and orange (Tolstoy and Bohnenstiehl, 2006) are plotted on the
93 right, and scaled on the left, to match peaks in the loop  **[[millisecond? Should spell out]]**
94 data from composite core RR0705-96PC/TC. Thick gray tie lines correlate the beginning of
95 seismic peaks with each other and with base of peaks in the core geophysical data. Gray
96 rectangles denote the correlation of the major pulses in the core geophysical data and the maxima
97 for the seismic data. The rectangles are labeled with the latitude of the center of each slip patch
98 maxima for the Chlieh et al. (2007, **fig. 9 therein**) inversion model G-M9.15. Visit
99 <http://dx.doi.org/10.1130/GES01066.S9> or the full-text article on www.gsapubs.org to view
100 Supplemental File S9.

101 ¹⁰Supplemental File S10. Turbidite flattening summary. Core data (geophysical data, imagery
102 data) are flattened to stratigraphic horizons as in **Figures 9 and 10** using symbols as in Figure 8.
103 This effectively renders the stratigraphy on a time basis across the area, thus each turbidite
104 represents a time horizon. The vertical scales are nonlinear except for 105PC, which is the
105 reference core and is plotted at the true vertical scale. Grid below cores except 105 is the
106 flattening matrix, and shows the vertical scale changes required, bars were originally evenly
107 spaced. **Cores**  **ect?]]** 102MC and 103PC are composited together, as are 96PC and 96TC.
108 Local variability is quite high in this core set, best illustrated by the ~3 m thickness of the 2004
109 bed in 96PC; this bed is more typically 10–15 cm thick at other sites. The anomalous
110 depositional style at the site of 104PC is also illustrated well. Many turbidites that have low
111 structural complexity at other sites are interpreted as the same events in 104, but with a common
112 depositional mode with numerous laminae composing a single bed. We interpret this
113 depositional style as potentially the result of amalgamation of numerous small local failures or

114 possible headward progressive failures following the initial ground failure. Similar site effects
115 are apparent at the site of 96PC/TC, which for all events shows an expanded, sandier version of
116 what we interpret to be correlative beds seen elsewhere. The 2004 bed is the most extreme of
117 these, but all other beds at this site show a similar expanded structure. Also illustrated are periods
118 of low rates of turbidite emplacement at some sites in restricted time periods. For example, in
119 108PC, few turbidites are deposited post T-21 time, about 2800 yr ago. While the likely 2004
120 bed is present, only ~4 beds were emplaced between these times. That time interval may contain
121 other events too diffuse for robust interpretation. The turbidite sequence is older than ~2800 yr,
122 well represented, and correlated to other sites. This site either became a poor recorder of events
123 after 2800 yr ago, our preferred interpretation, or the site could alternatively have been a site of
124 lower ground motions after 2800 yr ago. Please visit <http://dx.doi.org/10.1130/GES01066.S10> or
125 the full-text article on www.gsapubs.org to view Supplemental File S10.

126 A 6500 year earthquake history in the region of the 2004

127 Sumatra-Andaman subduction zone earthquake

128 **[[4 digit numbers (including dates) should not have commas]]**

129 **Jason R. Patton¹, Chris Goldfinger¹, Ann E. Morey¹, Ken Ikehara², Chris Romsos¹, Joseph**
130 **Stoner¹, Yusuf Djadjadihardja³, Udrek³, Sri Ardhyastuti³, Eddy Zulkarnaen Gaffar⁴,**
131 **Alexis Viscaino⁵**

132 ¹*College of Earth, Ocean and Atmospheric Sciences, Oregon State University, 104 CEOAS*
133 *Administration Building, 101 SW 26th Street, Corvallis, Oregon 97331 USA*

134 ²*National Institute of Advanced Industrial Science and Technology (AIST), 1-1-1 Umezono,*
135 *Tsukuba, Ibaraki 305-8568 Japan*

136 ³*Bandan Penghajian dan Penerapan Teknologi (BPPT), 2nd Building, 19th Floor, Jl.MH.*
137 *Thamrin 8, Jakarta, 10340 Indonesia*

138 ⁴*Geotechnology LIPI (Lembaga Ilmu Pengetahuan Indonesia), Jalan Cisitua-Sangkuriang,*
139 *Bandung 40141, Indonesia*

140 ⁵*Unitat de Tecnologia Marina-CSIC, Centre Mediterrani d'Investigacions Marines i Ambientals*
141 *(CMIMA), Passeig Marítim de la Barceloneta, 37-49, 08003 Barcelona, Spain*

142 **ABSTRACT**


143 In order to investigate the possibility of a long-term paleoseismic history from offshore
144 sedimentary records in Sumatra, we collected 144 deep-sea sediment cores in the trench and in
145 lower slope piggyback basins of the Sumatra accretionary prism. We used multibeam bathymetry
146 and seismic reflection data to develop an understanding of catchment basins, turbidity current
147 pathways, and depositional styles, as well as to precisely locate our gravity cores, piston cores,
148 Kasten cores, and multicores. We use detailed physical property data, including computed
149 tomographic X-ray, gamma density, magnetic susceptibility, grain-size analysis, faunal analysis,
150 and smear slides, to evaluate the turbidite stratigraphy and sedimentology at each site. We use
151 radiocarbon age control for piggyback basin sites above the carbonate compensation depth, and
152 use ²¹⁰Pb and ¹³⁷Cs to evaluate the timing of the most recent sedimentary deposits. Using well-
153 log correlation methods and radiometric age control, we test for potential correlations between
154 isolated sites in piggyback basins and the trench.

155 We find evidence for very young surface turbidites along the northern Sumatra margin,
156 most likely emplaced within the past few decades at the seafloor in both the 2004 and 2005
157 earthquake rupture zones, with no overlying hemipelagic sediment. Based on the young soupy
158 deposits, lack of oxidation, and ²¹⁰Pb and ¹⁴C age determinations, we interpret the uppermost



159 turbidite in 21 cores within the 2004 rupture area to have been deposited within a few years of
160 collection in 2007, and most likely as a result of the 2004 moment magnitude (M_w) ~ 9.2
161 earthquake. The likely 2004 turbidite has a distinctive stacked structure of three major fining-
162 upward sequences observed at several basin and trench sites, similar to the pattern of moment
163 release in the 2004 earthquake. We observe rapid die out of the 2004 and 2005 deposits with
164 distance from the slip zones, from local sources of sediment supply, and in the segment boundary
165 between the slip zones.

166 Many individual turbidites show strong similarities between isolated sites, as well as
167 having similar emplacement times. Based upon radiocarbon age control and lithostratigraphic
168 correlations between isolated basin and trench core sites, we interpret that 43 turbidites can be
169 linked spatially over a distance of ~ 230 km within the southern portion of the 2004 rupture zone.
170 Sampling at deep-water sites isolated from terrestrial and shallow-water sediment sources, as
171 well as potential storm or tsunami wave triggers, limits potential mechanisms for initiating
172 turbidity currents to plate boundary, crustal, or slab earthquakes. Other potential triggers, such as
173 tectonic oversteepening, random self-failures, gas hydrate destabilization, are unlikely to be
174 correlative between any two isolated sites. The most probable explanation for the similarity of
175 timing, turbidite sequences, and individual turbidite structure in isolated basin and trench
176 stratigraphic sequences is a seismogenic origin.

177 The mean interseismic time for probable strong to great (magnitude > 8) earthquakes in
178 the 2004 rupture region for the past 6.6 ± 0.14 k.y. is 160 yr for 43 events. The ages of 8 of the
179 10 uppermost deposits, spanning the past ~ 1500 yr, are largely consistent with the terrestrial
180 paleoseismic and/or tsunami records in Thailand, Sumatra, India, and the Andaman Islands,
181 suggesting either coincidence or a common origin. The mean interseismic time from the turbidite

182 record for this same period is 170 yr, comparable to the ~210 yr recurrence for regional tsunami.
183 The turbidite record is not well matched to 6 microatoll ages of rapid subsidence  uplift from
184 northern Simeulue Island for the ~1100 yr period of overlap; only 2 or 3 of 6 have permissive
185 temporal overlap. The turbidite record, at 180 yr (6 events), compares reasonably well to the
186 average for all events on northern Simeulue of 220 yr, and is identical to the tsunami interval of
187 180 yr for the same time period (6 events). Of the 43 correlated turbidites in the 2004 earthquake
188 region, 13 are well correlated in our cores along strike lengths of 150 km or greater, and satisfy
189 criteria for robustness; 24 turbidites correlated along a shorter strike distance may represent other
190 plate boundary earthquakes of shorter spatial extent and may include beds sourced from crustal
191 and slab earthquakes.

192 INTRODUCTION

193 Following the 26 December 2004 moment magnitude (M_w) ~9.2 Sumatra-Andaman and
194 11 March 2011 Tohoku-Oki subduction zone earthquakes and tsunamis, geologists have been
195 reevaluating global models of subduction zone earthquake recurrence (e.g., Ruff and Kanamori,
196 1980; Shimazaki and Nakata, 1980). Given the short record of historic earthquakes (a few
197 centuries) and the knowledge that many subduction zones have  at earthquake (i.e., $M > 8$)
198 return periods that span multiple centuries, it has been difficult to properly document,
199 characterize, and develop new models of their recurrence (Wesnousky, 1994; Murray and Segall,
200 2002; Satake and Atwater, 2007; Stein and Okal, 2007; Hindle and Mackey, 2011; Schlagenhauf
201 et al., 2011; Colella et al., 2012; Kagan et al.  12[[Added "et al." here to match the
202 reference list. O.K.?]]; Parsons, 2012; Parsons et al., 2012; Béjar-Pizarro et al., 2013; Davis et
203 al., 2013; Goldfinger et al., 2013a; Heki and Mitsui, 2013; Ide, 2013; Kopp, 2013; Ninis et al.,
204 2013). Many aspects of subduction zone seismogenesis have been evaluated to understand the

205 size, timing, and contributing factors that control the outcome of future great earthquakes (Chlieh
206 et al., 2008; Ruff and Kanamori, 1980; Wiseman and Bürgmann, 2011); parameters include
207 lower plate age, convergence rate, fault coupling ratio, seismicity, b-value, sediment thickness,
208 geodesy, and other factors. Paleoseismology can reveal the temporal and spatial behavior of a
209 fault through multiple earthquake cycles by using longer time spans than possible with historical
210 and instrumental records (McCalpin and Nelson 1996 [[Added to match the reference list.
211 O.K.?]]; Goldfinger et al., 2012a). Proxies for earthquake magnitude found in the paleoseismic
212 record may eventually provide some measure of the cycling of energy accumulation and release
213 (stress and strain) through time (Goldfinger et al., 2012a, 2013a). Submarine (and sublacustrine)
214 paleoseismology is advantageous for this purpose because the sedimentary record, while it
215 includes secondary evidence for earthquakes (McCalpin, 2009), can commonly preserve very
216 long records in great detail and provides expanded opportunities for testing spatial and temporal
217 patterns (Goldfinger et al., 2012a, 2013a).

218 Strong ground shaking from earthquake rupture has been inferred to trigger turbidity
219 currents that may deposit a very long record of past earthquakes in the form of turbidites
220 (Dallimore et al., 2005; Enkin et al., 2013; Goldfinger et al., 2003, 2008, 2012a; Inouchi et al.,
221 1996; Karlin and Seitz, 2007; Noda, 2004; Noda et al., 2008 [[Change O.K.?]]; Rajendran et al.,
222 2008; Shiki et al., 2000; Nakajima and Kanai, 2000; St-Onge et al., 2004, 2012). Triggering by
223 earthquakes, however, is far from unique; other available mechanisms must be distinguished
224 from earthquakes, or otherwise filtered from the sedimentary record in order to develop a
225 paleoseismic history. Methods to accomplish this have been developed for more than three
226 decades by combining evidence from sedimentology, tests of synchronicity, stratigraphic
227 correlation, and analysis of nonearthquake triggers. Together these criteria can be used to





228 develop a reliable earthquake record for sublacustrine and submarine fault zones (Adams, 1990;
 229 Karlin and Abella, 1992, 1996; Karlin et al., 2004; McHugh et al., 2006; Moernaut et al., 2007;
 230 Goldfinger et al., 2012a; Gràcia et al., 2010, 2012; Poudroux et al., 2012; Barnes et al., 2013;
 231 Smith et al., 2013; Van Daele et al., 2014, 2015, Polonia et al., 2015), **although there has been**
 232 **dissent (Atwater et al., 2012, 2014; Atwater et al., 2012 is not in the reference list. Should**
 233 **this be “Atwater and Griggs, 2012; Atwater et al., 2014”?)];** Sumner et al., 2013; Talling,
 234 2014).

235 **We** describe our initial results from a submarine paleoseismic investigation conducted
 236 offshore of Sumatra in the region of the 26 December 2004 $M_w \sim 9.2$ earthquake (Ishii et al.,
 237 2005; Subarya et al., 2006; Chlieh et al., 2007; Stein and Okal, 2007). We introduce the geologic
 238 setting and our resulting rationale for examining the stratigraphic record for evidence of
 239 earthquakes, mixed sources, or the lack thereof. Building on an initial examination of styles of
 240 sediment transport (Patton et al., 2013a), we closely examine the marine turbidite stratigraphy
 241 and event timing to test for the possibility of regional synchronous deposition suggestive of
 242 earthquakes.

243 **Sumatra-Andaman Subduction Zone Plate Boundary Seismicity**

244 The 26 December 2004 $M_w \sim 9.2$ earthquake that struck Sumatra and the Andaman–
 245 Nicobar Islands (e.g., Park et al., 2005) resulted in a tsunami that inundated coastal communities
 246 around the Indian Ocean, killing **more than** 220,000 people. This earthquake was followed by the
 247 M_w 8.7 Nias earthquake in March 2005 (e.g., Hsu et al., 2006; Briggs et al., 2006), and by
 248 earthquakes in 2007 (e.g., Konca et al., 2008) and 2010 (Bilek et al., 2011; Newman et al.,
 249 2011). These earthquakes all ruptured sections of the megathrust between the subducting India-
 250 Australia plate and the overriding Burma-Sunda microplate (Fig. 1). The 2004–2010 earthquake

251 series may constitute a repeating rupture series (Sieh et al., 2008). The 2004 and 2005 events
 252 were the first great subduction earthquakes in this region to be analyzed using advanced
 253 seismological and geodetic techniques.

254 Historic Sumatra-Andaman subduction zone (SASZ) earthquakes in the 2004 rupture
 255 zone (A.D. 1679, 1762, 1847, 1881, and 1941; Chhibber, 1934; Newcomb and McCann, 1987;
 256 Bilham, 2005; Malik et al., 2011) were much smaller (magnitude < 8.0) than the 2004
 257 earthquake (Fig. 1). Historic earthquakes farther south along the margin were also generally of
 258 smaller magnitude (north to south: 2002 M_w 7.3; 2010 M_w 7.8; 2008 M_w 7.4; 1861 M 8.6; 1907
 259 M_s 7.6; 1984 M 7.2; 1935 M_w 7.7; 1797 M_w ~8.6; 2009 M_w 7.5; 1833 M_w ~9; 2007 M_w 8.4, 7.9;
 260 2004 M 7.3; 2010 M_w 7.7; 2000 M_w 7.9; Newcomb and McCann, 1987; Rivera et al., 2002;
 261 Abercrombie et al., 2003; Natawidjaja et al., 2006; Konca et al., 2008; Sieh et al., 2008; Bothara
 262 et al. 10[[Added "et al." to match the reference list.]]; Kanamori et al., 2010; Philibosian et
 263 al., 2012, 2014). Recent investigations of secondary evidence left behind by tsunami as sand
 264 sheets in northern Sumatra (Monecke et al., 2008), Thailand (Jankaew et al., 2008), and the
 265 Andaman and Nicobar Islands (Rajendran et al., 2008, 2013), along with coral microatoll
 266 evidence (Meltzner et al., 2010, 2012), suggest that the penultimate subduction zone earthquake
 267 most likely occurred 500–700 yr ago, and an antepenultimate earthquake or tsunami in Sumatra
 268 (Monecke et al., 7[[Monecke et al., 2007 is not in the reference list.]]; Rajendran et al.,
 269 2008), the Andaman and Nicobar Islands (Rajendran et al., 2008), and India (Rajendran et al.,
 270 2007[[led "et al." to match the reference list.]] likely occurred ~900–1200 yr ago. These
 271 initial studies suggested that recurrence of M 8 earthquakes is ~500 yr within the past 1200
 272 yr.

273 **Tectonic Setting**

274 The southern 2004 rupture was centered beneath an ~150-km-wide forearc plateau, in
 275 contrast to the typical wedge structure of many accretionary margins (Moore and Karig, 1980;
 276 Henstock et al., 2006; Fisher et al., 2007). The rupture initiated near Simeulue Island and
 277 propagated updip and northwestward at 2–2.5 km/s (e.g., Ammon et al., 2005; Ishii et al., 2005;
 278 Chlieh et al., 2007, Figs. 1 and 3 therein). Moment release appears to have been concentrated in
 279 three main patches that were captured in nearly all inversion models (Ni et al., 2005
 280 **2005 is not in the reference list.**); Tolstoy and Bohnenstiehl, 2006; Ishii et al., 2007; Chlieh et
 281 al., 2007). In some of the seismologic records, there are more than three maxima (e.g., Chlieh et
 282 al., 2007, Fig. 21, showed five or six slip maxima). Offshore northern Sumatra, the location of
 283 the greatest seismic moment release (e.g., Ammon et al., 2005), the rupture propagated relatively
 284 far seaward beneath a large part of the forearc plateau and/or prism, and was not focused beneath
 285 the forearc basins, as suggested by some models that attempted to correlate basins and gravity
 286 anomalies with the seismogenic region of subduction zones (Wells et al., 2003; Song and
 287 Simons, 2003). In contrast, slip during the 2005 rupture was concentrated further downdip
 288 beneath the forearc islands and did not propagate coseismically beneath the seaward-tapered
 289 wedge. Velocity strengthening slip occurred updip and downdip postseismically over the next
 290 few months (Hsu et al., 2006).

291 **Physiography of the Sumatra-Andaman Subduction Zone**

292 The SASZ is formed by the Indo-Australia plate, which is subducting 50–70 mm/yr at
 293 ~N30E beneath the Burma microplate of Eurasia (Fig. 1; Bock et al., 2003; Subarya et al.,
 294 2007 **2007 is not in the reference list. 2006 here instead?**). The continental
 295 margin morphology in western Sumatra is dominated by the upper plate structure of a Tertiary
 296 and Quaternary accretionary prism with structural highs and forearc basins (Karig et al., 1980;

307 Fisher et al., 2007). Fold and thrust belt topography forms longitudinal, discontinuously linked
308 basins that can be isolated, drain to other basins, or drain to the trench. Canyon systems tend to
309 be short and drainage catchments are relatively small, limiting the potential areal extent of source
300 areas for turbidity currents (Graindorge et al., 2008).

301 The rarity of longer trench-normal canyon systems is likely due to the lack of terrestrial
302 sediment sources. Most of the northern Sumatra forearc is isolated from Sumatra by a broad
303 unfilled forearc basin that traps sediment and isolates the outer forearc (Matson and Moore,
304 1992; Sieh and Natawidjaja, 2000). Some exceptions are the canyons that lead to Simeulue
305 (2.6°N) and Nias (1.1°N) Islands. These canyons likely supply sediment from the islands to the
306 slope basins, and potentially to the trench (Ladage et al., 2006, Fig. 2 therein). Sediment input to
307 these canyons may include turbidity currents or hyperpycnal flows related to cyclones, high
308 swell from the Southern Ocean, or tsunami waves. The northern limit of such potential influence
309 is 2°N, the northernmost basin that could conceivably receive sediment from Simeulue Island.
310 The subdued or absent trench-parallel channel systems offshore Sumatra (Patton et al., 2013a)
311 are likely due to the low late Pleistocene sedimentation rate and the interruption of the trench by
312 subducting features. Regional transport in the trench from northern sources is thought to be cut
313 off from Himalaya-derived sediment by a large landslide at 14°N (Moore et al., 1976) and the
314 intersection of the Ninetyeast Ridge with the subduction zone trench (Bandopadhyay and
315 Bandyopadhyay, 1999; Fig. 1).


316 The trench deepens southward from 4.5 to 6.5 km from 5°N to 7°S, and is filled with
317 sediment several kilometers thick in the north from the Nicobar fan (a southeastern extension of
318 the Bengal fan; Patton et al., 2013a), partially burying lower plate structures that trend across the
319 trench (Dean et al., 2010; Graindorge et al., 2008). The outer forearc is sedimentologically



320 isolated from northern Sumatra by a longitudinal forearc basin, which is composed of the Aceh,
321 Simeulue, Nias, Pini, Siberut, and Bengkulu Neogene forearc subbasins (Matson and Moore,
322 1992; Sieh and Natawidjaja, 2000; Susilohadi et al., 2005; Supplemental File S1¹). Lack of input
323 from the forearc basin and from northern sediment sources results in recent sediment starvation
324 in terms of modern inputs; thus the abyssal seafloor topography is dominated by trench-
325 subparallel bending moment normal faults and north-striking fracture zones. The bathymetry of
326 the forearc high is controlled largely by the blocks of sediment as much as 4 km thick
327 (Bandopadhyay and Bandyopadhyay, 1999; Fisher et al., 2007) uplifted from the Indo-Australia
328 plate (likely by duplexing of the accretionary complex) to form the upper part of the accretionary
329 prism and marginal plateau (Fisher et al., 2007; Mosher et al., 2008[[Mosher et al., 2008 is not
330 in the reference list. 2010 here instead, or add a ref?]]; Gulick et al., 2011). While
331 throughgoing submarine canyon systems are absent, short canyon systems linking some basins in
332 short paths through the outer slope to the trench exist (Patton et al., 2013a, Fig. 1 therein). The
333 erosional style of the outer forearc is indicative of relatively high erosion rates, numerous
334 coalescing small failures, and headward canyon migration from threshold mass wasting during
335 dissection from erosional retreat (Howard, 1994, 1997). This erosion style, in turn, is consistent
336 with low-cohesion sediments and is consistent with the many basins that correct?]] do not
337 drain to the trench and have an expanded Holocene section (e.g., Lamb et al., 2006). Outer
338 forearc canyon systems have channels only on the flanks of the lower slope and these channels
339 morphologically die out in the trench, trending to the south, within tens of kilometers from the
340 canyon mouths. Limited channel development suggests moderate mixing of turbidity currents
341 dominated by proximal sedimentary processes (Patton et al., 2013a).

342 **Turbidite Paleoseismology and Rationale as Applied to the Northern Sumatra Margin**


343 Primary evidence of past earthquakes generally involves the identification of sedimentary
 344 deposits (including soils) that have been offset by fault rupture, typically found in an excavation
 345 across the fault (McCalpin, 2009). Secondary evidence of past earthquakes is interpreted from
 346 sedimentary deposits that contain evidence of fault motion from an earthquake (Atwater, 1987;
 347 Atwater and Hemphill-Haley, 1997; Goldfinger, 2009). The paleoseismology of subduction zone
 348 faults is primarily based on secondary evidence because the subduction zone fault is located in
 349 the submarine setting, where fault trenching is not yet possible. Examples of secondary evidence
 350 for subduction zone earthquakes include tsunami deposits (Hemphill-Haley, 1995), buried marsh
 351 soils (Atwater, 1987), landslides (Wilson and Keefer, 1985; Schulz et al., 2012), and turbidites
 352 (Adams, 1990; Goldfinger et al., 2003; Poudoux et al., 2012).

353 **Applicability to a Variety of Settings**


354 Turbidite paleoseismology in sublacustrine and submarine environments has been applied
 355 in numerous localities globally, under a variety of conditions of climate, sedimentation rate, and
 356 subaqueous setting (methods used in each study are listed in parentheses): Lake Baikal (whole
 357 core and surface scanning magnetic susceptibility; Lees et al., 1998a, 1998b), Ecuador
 358 (correlation of mass transport deposits, MTDs, and the comparison between return times of
 359 MTDs, turbidites, and earthquakes; Ratzov et al., 2010), Iberian margin (turbidite chronologic
 360 correlation, interturbidite hemipelagic thicknesses, core geophysics, and geochemical
 361 composition; Gràcia et al., 2010), Kumano ould this be Kumano Basin, as in the
 362 **GEBCO Gazetteer of Undersea Feature names?]]**; Japan (particle size, ¹³⁷Cs geochronology,
 363 X-ray radiography, and bulk density; Shirai et al., 2010), Lake Washington, Washington (core
 364 geophysics, X-ray radiography, and particle size; Karlin and Abella, 1992, 1996; Karlin et al.,
 365 2004), Lake Tahoe, California (sediment core isotopic correlation, anisotropic magnetic

366 susceptibility, and ^{14}C geochronology; Karlin and Seitz, 2007), Okinawa Trough, Japan
 367 (correlation of core porosity and particle size, ^{210}Pb and ^{137}Cs , and comparison of turbidite return
 368 timing; Huh et al., 2004, 2006), central Switzerland (historic earthquake timing compared to ^{14}C
 369 geochronology, high-resolution seismic data, and sedimentary structures; Monecke et al., 2006),
 370 Saguenay Fiord, Canada (biotracers, mass physical properties of sediment cores, and high-
 371 resolution seismic and sidescan profiles; Syvitski et al., 1996  **Syvitski et al., 1996 is not in the**
 372 **reference list. Syvitski and Schafer here instead?]); St-Onge et al., 2004), Canadian Arctic
 373 (sediment provenance and sediment accumulation rates; Grantz et al., 1996), **Kuril-Kamchatka Trench**
 374 **[[should this be Kuril-Kamchatka Trench, as in GEBCO gazetteer?]]** (correlation based
 375 upon lithology, sand grain composition, and ^{14}C , ^{210}Pb , and ^{137}Cs chronology; Noda et al., 2008),
 376 Lake Biwa, Japan (sedimentation rate chronology compared with historic earthquake records, X-
 377 ray radiographs, and correlation of core geophysical data, *i.e.*, density, Inouchi et al., 1996;
 378 sedimentary structures and grain-size distribution, Shiki et al., 2000), the southern margin of
 379 Japan (magnetomineralogical fabric analysis; Abdeldayem et al., 2004), Cascadia (core
 380 geophysics, confluence test, and ^{14}C chronology; Goldfinger et al., 2003; 2012a; Gutiérrez-
 381 Pastor et al., 2005a, 2005b, 2009, 2013; Enkin et al., 2013; Blais-Stevens et al., 1997, 2011;
 382 **Blais-Stevens and Clague, 2001**  **[[Corrected the listing here.]]**), the northern San Andreas fault
 383 in California (core geophysics, confluence test, and ^{14}C chronology; Goldfinger et al., 2003,
 384 2008); south and south-central Chile (high-resolution reflection seismic profiles, comparison to
 385 historic earthquakes, particle size, and X-ray radiograph computed tomography scanning;
 386 Moernaut et al., 2007; Van Daele et al., 2014), Gulf of California (Gonzalez-Yajimovich et al.,
 387 2007), the Santa Barbara basin (turbidite volume and submarine distribution in km^2 , comparison
 388 with historic flood and earthquake records; Gorsline et al., 2000), eastern Japan Sea (correlation**

389 between seismic reflection data and sediment core, ^{137}Cs chronology, and comparison with
390 historic earthquake, turbidite structure, particle size, sediment composition; Nakajima and Kanai,
391 2000), central Mediterranean (grain size, core geophysics, X-ray imagery, geochemistry,
392 mineralogy, and micropaleontology; Polonia et al., 2013a, 2013b), and Marmara Sea (^{14}C
393 chronology compared with historic earthquakes, lithological composition; McHugh et al., 2006;
394 Sarı and Çağatay, 2006; Çağatay et al., 2012; McHugh et al., 2014).


395 Earthquakes are well known as subaerial landslide triggers, with a possible minimum
396 triggering earthquake magnitude of $M \sim 5$ (Keefer, 1984). Landslide density is found to be
397 greater in areas of stronger ground acceleration (Meunier et al., 2007). Earthquake magnitude
398 thresholds for submarine landslides are less well constrained than subaerial landslides (suggested
399 as $M \sim 7.1$ in Cascadia; Goldfinger et al., 2012a, 2013a; $M 7.4$ in Japan, Nakajima and Kanai,
400 2000; $M 7.3$ in northern California and Cascadia, Wilson and Keefer, 1985; $M 5.2$ in Venezuela,
401 Lorenzoni et al., 2012), probably because the evidence of minimum values is largely lacking.
402 Black (2014) estimated a global average minimum value of Modified Mercalli Intensity (MMI)
403 5.5 for existing studies, although minimum value estimates are rare. Earthquakes are posed as
404 one of the dominant submarine landslide triggers (Ross, 1971; Almagor and Wiseman,
405 1977[[Only Almagor and Wiseman, 1991 is in the reference list. Change year here?]];
406 Hampton et al., 1978, 1996; Masson et al., 2006), with most historic examples attributed to
407 ground accelerations from earthquakes (Mosher et al., 2010).



408 Submarine landslides may transform into turbidity currents that leave behind turbidites
409 (Morgenstern, 1967; Stow and Bowen, 1980; Felix and Peakall, 2006), known as
410 seismoturbidites or seismites when earthquake triggered. Turbidity currents are turbulence driven
411 (autosuspension) sediment-rich gravity flows (Bouma, 1962; Middleton, 1967; Kneller and

412 Buckee, 2000). The sedimentary sequence of an individual deposit reflects the time history of
413 deposition from the turbidity current as it passes a sedimentary depositional setting (Baas et al.,
414 2004). The vertical structure of a turbidite is a sampling of the longitudinal velocity and density
415 structure of the causal turbidity current (Lowe, 1982; Kneller and McCaffrey, 2003). Early
416 assumptions were that turbidity currents are the result of a single impulse of sediment into the
417 system and that multiple fining-upward sequences were due to erosion of older deposits by
418 younger currents (Ericson et al., 1952[[ed "et al." to match the reference list.]]; Kneller
419 and McCaffrey, 2003). More recent studies have revealed that the input of sediment into the
420 turbidity current was not always singular, but was likely formed from a temporally
421 heterogeneous flux of sediment (Lowe, 1982; Piper et al., 1999; Nakajima and Kanai, 2000;
422 Kneller and McCaffrey, 2003; Goldfinger et al., 2008, 2012a; Gutiérrez Pastor et al., 2013).
423 Local geologic variability and hydrodynamic factors may also contribute to the longitudinal
424 variability of the turbidity current and, therefore, the vertical structure of a turbidite. For this and
425 other reasons, it is difficult to interpret the physical components of a turbidite based on a single
426 or a few cores without having core data sampled from upstream and downstream within the same
427 channel system (Kneller and McCaffrey, 1995), and within multiple systems in the case of
428 regionally triggered currents.

429 In Adams (1990) and Goldfinger et al. (2003, 2012a), eight plausible triggering
430 mechanisms for turbidity currents were suggested: storm wave loads, earthquake loads, tsunami
431 wave loads (local or distant), sediment loads, hyperpycnal flows, volcanic explosions, submarine
432 landslides, and bolide impacts. In addition to these triggers, tidal bottom currents may be
433 included in this list (Thomson et al., 2010). Of the possible landslide triggers listed in Adams
434 (1990), Sultan et al. (2004), Goldfinger (2010), and Goldfinger et al. (2012a), only bolide

435 impacts, hyperpycnal flows, tides, wave loads, and earthquakes can directly trigger submarine
436 landslides, as other phenomena may simply precondition the slope for failure (Goldfinger et al.,
437 2012a). This subset of triggers can be evaluated in terms of plausibility, expected frequency,
438 sedimentology, aerial extent, and correspondence to other evidence onshore and other factors.
439 Some suggest **that** turbidite structure is evidence that autocyclic forcing dominates turbidite
440 deposition (Kneller and McCaffrey, 2003; Dennielou et al., 2006), but they do not consider a
441 longitudinal change in sediment flux within the turbidity current. Others suggest that the
442 allocyclic forcing of turbidity currents is preserved in the turbidite structure because the current
443 flows were triggered by a shared source, possibly due to earthquakes (Goldfinger and Morey,
444 2004; Garrett et al., 2011; Goldfinger, 2011; Goldfinger et al., 2012b). Amalgamation is posed as
445 an indicator that the turbidites were deposited from multiple turbidity currents, merging and
446 forming a longitudinal structure reflected in the deposit (Nakajima and Kanai, 2000), possibly
447 from multiple slides on slopes. In Lake Biwa, Nakajima and Kanai (2000) concluded **that** these
448 multiple pulses are the results of synchronous triggering of multiple parts of the canyon system.
449 Turbidite structure is likely a combination of these multiple factors. In Goldfinger et al. (2003,
450 2007, 2008, 2012a) and Goldfinger and Morey (2004), a seismogenic trigger to Cascadia and
451 northern San Andreas turbidity currents was attributed through stratigraphic correlation of
452 turbidites with shared sedimentary structures (i.e., fingerprints), supported by a framework of
453 positionally constrained radiocarbon ages and relative age tests, demonstrating that they
454 represent synchronous deposition (Goldfinger et al., 2012a, 2013b).

455 The study of turbidite paleoseismology  **the best** developed for the Cascadia subduction
456 zone (CSZ; Goldfinger et al., 2012a, 2013a). The seminal work of Adams (1990) used a tephra
457 datum (Mazama **ash**, **ca.** 7.7 ka; Bacon, 1983; Zdanowicz et al., 1999; Klug et al., 2002; Bacon


458 and Lanphere, 2006) and a confluence of separate channels to constrain the number of turbidites
459 above the tephra in each core (confluence test; Adams, 1990). This confluence test is, in part, the
460 basis of the original case for seismogenic triggering of these turbidity currents. What also
461 contributed to the success of the work in Cascadia was the extensive research done on both the
462 turbidite systems offshore and the terrestrial paleoseismology in the region; this provided a
463 chronologic framework with which to compare the submarine results (Duncan, 1968; Nelson,
464 1968; Nelson et al., 1968; Barnard, 1973; Griggs, 1969; Carlson, 1971  **[[Only Carlson, 1967 is**
465 **in the reference list. Please advise.]]**; Nittrouer, 1978; Atwater, 1987; Atwater and Hemphill-
466 Haley, 1997; Kelsey et al., 2002). Although several alternatives have been proposed based on
467 1960s core logs (Atwater and Griggs, 2012; Atwater et al., 2014), modern bathymetric,
468 backscatter, and core data show these alternatives to be either too old, or nonexistent (Beeson
469 and Goldfinger, 2013; Goldfinger et al., 2013a, 2014b). While others suggested that the CSZ
470 might be seismogenic, using uplifted topography and rates of secular vertical motion (Adams,
471 1984), Atwater (1987) found the first geologic evidence of paleotsunami and paleodeformation
472 related to subduction zone earthquakes along the CSZ in the form of sand sheets overlying
473 coseismically subsided intertidal to supratidal deposits. Thereafter, more evidence of
474 paleodeformation, paleotsunami, and paleoliquefaction was found and compiled into a catalog of
475 paleoseismic events that had variations in space and time (Peterson and Madin, 1997; Obermeier
476 et al.,  **[[Obermeier et al., 2000 is not in the reference list. Obermeier and Dickenson**
477 **here instead?]]**; Kelsey et al., 2002; Leonard et al., 2004, 2010; Kelsey et al., 2005; Nelson et
478 al., 2006; Goldfinger et al., 2008, 2012a; Graehl et al., 2014). Onshore, it was not possible to
479 directly correlate stratigraphic evidence from site to site because the terrestrial sedimentary
480 evidence was discontinuous between sites north to south and radiocarbon uncertainties preclude

481 establishing synchronous occurrence (Nelson et al., 2006). It was not until the submarine record
482 was developed that the spatiotemporal links could be made between offshore sites, with less
483 certainty, to the existing terrestrial records (Goldfinger et al., 2008, 2012a; Witter et al., 2011,
484 2013). Unfortunately such an extensive terrestrial record for past earthquakes is not well
485 developed for the SASZ.


486 In this paper we test the plausibility of a seismogenic trigger as a source for the observed
487 turbidite stratigraphy in northern Sumatra primarily by (1) using tests for synchronous triggering
488 of sedimentologically isolated turbidite systems and (2) using sedimentologic characteristics
489 (e.g., structure) of the turbidites. We apply both lines of investigation to aid in discrimination
490 between potential seismic and nonseismic trigger sources. Radiocarbon age estimates provide
491 constraints to broadly establish the temporal stratigraphic sequences and to compare sequences
492 between multiple sites. While individual radiocarbon ages have the same temporal limitations in
493 the sea that they do onshore, in the marine environment, interevent sedimentation provides an
494 independent temporal reference that can be used in integrated age models to improve precision
495 and reduce uncertainties (Bronk Ramsey, 1995, 2009a, 2009b; Gutiérrez-Pastor et al., 2009;
496 Goldfinger et al., 2012a; Enkin et al., 2013). Lithostratigraphic correlations and radiocarbon
497 constraints can form a robust test of continuity of depositional sequences among sites
498 (Goldfinger et al., 2012a).

499 **Approach for Sumatra**

500 Our rationale in Sumatra differs from that of Cascadia in several important ways, as the
501 margin physiography and water depth range require a different approach. In general, our strategy
502 was to seek sites that were sedimentologically isolated from terrestrial sediment sources and
503 from each other. Limiting landslide trigger types is the initial filtering method we use to simplify

504 the paleoseismic problem. Isolated deep-water sites with no terrestrial or shallow-water sediment
 505 source areas eliminate storm and tsunami wave loading, hyperpycnal flow, and to some extent
 506 self-failure due to sediment accumulation, leaving crustal, slab, and plate boundary earthquakes
 507 and localized self-failures as possible trigger mechanisms. With the problem reduced to the
 508 simpler case, if turbidites can be correlated between isolated sites separated by large distances,
 509 synchronous triggering and earthquake origin is likely; otherwise no correlation  similarity of
 510 turbidite sequences is expected. Individual links are commonly subject to the uncertainties in
 511 correlation and radiometric age control, thus a large number of sites is preferred in order to
 512 improve the signal to noise ratio in the event that a coherent signal exists (Goldfinger et al.,
 513 2003, 2008, 2012a; Shiki, 1996; Gorsline et al., 2000; Nakajima, 2000; Shiki et al., 2000).

514 **METHODS**

515 We used primarily 10-cm-diameter piston and gravity cores to collect turbidite
 516 stratigraphy, supplemented with Kasten cores, box core, and multicores (the latter two are used
 517 to sample the sediment-water interface and the uppermost units with minimal disturbance); 
 518 cm² Kasten cores are useful because they provide a larger volume of sediment from which
 519 volume restricted age samples (CaCO₃ foraminiferid tests) are collected.

520 **Site Selection and Coring**

521 As in all geologic and paleoseismic investigations, selecting the best sites is critical in
 522 submarine paleoseismology (Goldfinger et al., 2014b). We use continental margin physiography
 523 to narrow the selection of sites to those most likely to preserve seismoturbidites, while seeking to
 524 exclude as many other sedimentary sources as possible. We sought core sites that would be most
 525 likely to preserve stratigraphy with deposits that have the greatest dynamic range in particle size
 526 (texture) above the background sediment particle size or density and with an expanded


527 stratigraphic section. With a large dynamic range in texture, the distinction between hemipelagic
528 mud and turbidite sediment is enhanced and vertical separation between turbidite deposits is
529 increased. This distinction is important for calculating background sedimentation rates and
530 sampling for age control. A large dynamic range in texture also helps with stratigraphic
531 correlation (discussed in the following). Core sites that are too distal have turbidites with very
532 little variation in density and particle size (Kneller and McCaffrey, 2003), making it difficult to
533 characterize the structure of any given deposit. Distal sites in an unchannelized setting may fade
534 very rapidly from local sources (Nelson et al., 1986; Baas et al., 2004, 2005; Johnson et al.,
535 2005; Goldfinger et al., 2012a, 2014a, 2014b; Patton et al., 2013a). Conversely, core sites that
536 are too proximal are commonly dominated by a series of amalgamated debrites (Bouma, 2004),
537 making interpretation problematic.

538 Our rationale for selecting core sites also considers issues of age control, sedimentary
539 isolation, and geospatial relevance to historic and prehistoric fault segments. We selected core
540 sites in slope basins due to the absence of usable radiocarbon material in cores collected in the
541 trench below the carbonate compensation depth (CCD). A benefit of these slope basin core sites
542 is that they typically have isolated submarine landslide source areas. However, this is also a
543 disadvantage for paleoseismology as most coring sites are therefore more proximal to their
544 source, which may result in noisier and less distinguishable sedimentary structure that is more
545 difficult to compare from site to site. We also collected a suite of trench cores paired for the most
546 part with basin cores to test whether these could be correlated to the basin sites that have age
547 control.



548 We initially focused our efforts on the basin-to-basin correlations because the addition of
549 radiocarbon strongly constrains stratigraphic sequence comparisons. As in Cascadia, we began

550 by correlating piston and trigger cores, then progressed to the nearest and least ambiguous sites.
551 We then addressed more and more distant and or difficult sites. While basin sites are discrete
552 spatially, trench sites have potential for along-trench transport, thus smearing the signal from
553 earthquakes (or any source) along strike. The lack of long trench-parallel channel systems in
554 Sumatra suggests that a given turbidity current will not travel a sufficient distance along the
555 trench axis and confound its association with a given earthquake by its spatial extent and position
556 alone, perhaps mitigating this problem to some extent.

557 We are not only interested in developing a chronology of earthquakes along this
558 subduction zone, but we are also interested in investigating the spatial limits of past earthquake
559 ruptures. Because most subduction zones and other major faults exhibit segmentation, and
560 segmentation in historical and paleoseismic data in Sumatra strongly suggested it, we initially
561 adopted these segments as an initial testable hypothesis. We used the proposed segments (Kopp
562 et al., 2008) to guide our core site selection, although we did not have enough spatial coverage to
563 discretely test all the segments rigorously. While this premise was untested in 2007, it has
564 subsequently been supported by onshore paleoseismic work (Jankaew et al., 2008; Monecke et
565 al., 2008; Sieh et al., 2008; Fujino et al., 2009; Meltzner et al., 2010, 2012; Dura et al., 2011;
566 Philibosian et al., 2012, 2014). We chose core sites that are within these historic and recent
567 prehistoric segments, as well as at the segment boundaries. Trench cores are more likely to
568 include records from adjacent slip regions because the trench may transport these turbidity
569 currents. The slope cores are less likely to do so, due to their smaller source areas and shorter
570 transport paths parallel to the margin. The boundaries received less emphasis because they
571 commonly have reduced earthquake slip and confusing records (Goldfinger et al., 2014a, 2014b).
572 Because the effects of earthquakes taper rapidly with distance from the fault slip (deformation:


573 Natawidjaja et al., 2004, 2006; Meltzner et al., 2006, 2010, 2012; Sieh et al., 2008; Philibosian et
574 al. 2012; ground shaking: Arias, 1970; Keefer, 1984; Wilson and Keefer, 1985; Wilson, 1993;
575 Campbell, 1997; Kayen and Mitchell, 1997; Youngs et al., 1997; Atkinson and Boore, 2003,
576 2011; Travararou et al., 2003; Sorensen et al., 2007; Boore and Atkinson, 2008; Zhao et al.,
577 2012[[Zhao l., 2012 is not in the reference list. Zhao and Xu here instead?]]; Black,
578 2014), the sedimentary evidence of these earthquakes may also be spatially limited. Sites that
579 receive sedimentary input that **was** transported in the trench would violate this spatial limit
580 premise (Black, 2014). Cores that are near segment boundaries may be difficult to correlate
581 because they may either have diminished sedimentary records (deposits with lower dynamic
582 range of density or lesser developed structure) or have records from the overlapping fault
583 segments (possibly for larger magnitude earthquakes). At a more local scale, we selected sites
584 close to local slopes and near the outlets of local canyons. Experience in Cascadia (Goldfinger et
585 al., 2012a) has shown that unchannelized flows may have short run-out distances, thus broad
586 basins were avoided. Our initial efforts have focused primarily on evidence in the region of the
587 2004 SASZ earthquake and other areas will be considered **subsequently**.

588 Multibeam mapping was essential for evaluating the physiographic setting for the
589 relevant sedimentary systems. Multibeam bathymetry and backscatter data were collected with
590 the Kongsberg EM-120 system on the R/V *Roger Revelle*, and edited on board using MBSystem
591 (<http://www.mbari.org/data/mbsystem/>) so that coring sites could be chosen in real time (Patton
592 et al., 2007; *Roger Revelle* Cruise RR0705 Superquakes07 **cruise report**,
593 <http://www.activetectonics.coas.oregonstate.edu/sumatra/report/index.html>). Prior to the cruise,
594 existing bathymetric data were compiled. Sumatra bathymetry was collected by expeditions (R/V
595 *Natsushima*—Japan Agency for Marine Earth-Science and Technology, Jamstec; HMS *Scott*—


596 UK Royal Navy and Southampton Oceanography Centre, NOCS; R/V *Marion Dufresne*—
597 *Institut Français de Recherche pour l'Exploitation de la Mer, IFREMER*; R/V *Sonne*—German
598 Federal Institute for Geosciences and Natural Resources, BGR) and shared utilizing a
599 cooperative agreement with these international institutions and the Indonesian Government
600 (Agency for the Assessment and Application of Technology, BPPT), without which our coring
601 study would not have been possible (Henstock et al., 2006; Ladage et al., 2006). The EM 120 has
602 a depth resolution of 10, 20, and 40 cm, for pulse lengths of 2, 5, and 15 ms, and covers depth
603 ranges from 20 to 11,000 m. The resulting 100 m grid cell size is a function of the best resolution
604 of the systems used. Several areas of higher (50 m) resolution data collected on the HMS *Scott*
605 are also available for the outer Sumatra forearc in the 2004–2005 rupture areas (Tappin et al.,
606 2007  **Tappin et al., 2007 is not in the reference list.]]**). After editing the raw data, we
607 visualized and rendered the bathymetric data using Fledermaus (www.qps.nl/display/fledermaus)
608 and ArcGIS (www.esri.com/software/arcgis) software applications in order to plan for potential
609 core sites. **[[ok  add sites?]]**

610 We extensively used 3.5 kHz compressed high-intensity radar pulse (CHIRP) shallow
611 subbottom profiles to survey Holocene turbidite stratigraphy in trench and slope basins to aid in
612 core site selection. We used a Knudsen 320BR (FM CHIRP mode typically sweeping 2–6 kHz)
613 at full bandwidth and data rate. These lines were heave corrected in real time using the ships'
614 PosMV320 motion sensor. We postprocessed the data using Sioseis
615 (<http://sioseis.ucsd.edu/sioseis.html>; Henkart, 2011) using band pass filtering, muting, and a
616 heave-filtering algorithm. Digital correlation processing of the CHIRP signal reduces the
617 effective frequency, improving the signal to noise ratio and boosting the effective vertical
618 resolution to ~25 cm, degraded somewhat by off-axis scatterers, vessel motion, and the water

619 column. In addition to the utility of developing a potential core site, these seismic reflection data
620 can reveal the continuity (or lack thereof) of repeated local turbidite sedimentation, local
621 faulting, and mass wasting deposits both within and between sites.

622 After we selected a core site, we typically deployed a 6.66-cm-diameter gravity corer.
623 This core was used as a reconnaissance tool due to the higher velocity that the core can be
624 deployed to the seafloor (100 m/min, versus 40 m/min for larger diameter cores). For sites where
625 good turbidite stratigraphy was found, we then deployed a 10.14-cm-diameter piston-trigger core
626 pair. Due to equipment failures (sheave bearings below deck were incapacitated due to high
627 temperatures near the equator), piston cores were mostly deployed on a railroad track constructed
628 from spare parts mounted to the stern deck using the stern A-frame. This configuration limited
629 the length of the piston corer to 2 core sections (2  10 ft, ~0.6 × 3 m), with a maximum coring
630 depth of 6.09 m. Trigger cores had a maximum coring depth of 3.05 m. The 1000–2200 kg
631 weight stand (attached to the piston corer) drives the piston core into the seafloor with greater
632 velocity than the trigger corer (possibly eroding surface sediment from the seafloor), thus core
633 tops are occasionally lost from the piston core, but typically not the trigger or multicores (unless
634 due to overpenetration). Kasten cores, box cores, and multicores collect the uppermost sediments
635 in greater volume and detail.


636 All cores were scanned for geophysical properties (multisensor core logging including
637 gamma density, low-resolution magnetic susceptibility (MS) using a loop sensor, P-wave
638 velocity, and resistivity). Cores were then split lengthwise and imaged with a GeoTek high-
639 resolution line-scan camera and described on lithostratigraphic data sheets including onboard
640 micropaleontologic, mineralogic, and tephra data collection. We adopted the sedimentary
641 terminology of laminae and beds from Campbell (1967). Subsequently, high-resolution point MS

642 data were collected from each core using a point sensor (Bartington MS2E high-resolution
643 surface sensor) at 0.5 or 1 cm intervals. Following the cruise, cores were then scanned with
644 computed tomographic X-ray techniques (CT scans) using a Toshiba Aquilion 64 slice CT unit at
645 0.5 mm voxel resolution. CT data permit a refined view of the strata and the effects of core
646 disturbance in high resolution and in three dimensions. CT data also provide densostratigraphic
647  quotes]] information (downcore variation in density) when CT imagery is used for
648 downcore line-scan analysis. Gamma and magnetic data reflect signals that average these effects
649 over a vertical distance related to the amount that the sediment is disturbed vertically. Grain-size
650 analysis was done using laser diffraction particle size measurements using a Beckman-Coulter
651 LS 13 320 laser counter (Blott and Pye, 2006) with a Fraunhofer based polarization intensity
652 differential scattering optical model. Particle size analyses are limited to a size range of 0.040–
653 2000 μm . In a limited number of cores we collected downcore X-ray fluorescence measurements
654 and superconducting rock magnetometer measurements of natural remnant magnetization.
655 Accelerator mass spectrometry (AMS) ^{14}C radiocarbon analyses, and ^{210}Pb and ^{137}Cs isotopic
656 analyses were performed for age control. We also conducted neutron activation analysis on a
657 multicore, seeking evidence of short-lived radionuclides and isotope chemistry. Core geophysical
658 methods and radiometric age analyses are further summarized in [Supplemental File S2²](#).

659 Age Control

660 Age control for stratigraphy is provided by AMS ^{14}C , ^{137}Cs , and ^{210}Pb radiometric
661 techniques. The ^{14}C data are based on decay with a half-life of 5730 yr and are useful for strata to
662 ~50,000 yr old (Stuiver and Polach, 1977; Stuiver and Braziunas, 1993; Hughen et al., 2004;
663 Fairbanks et al., 2005; Reimer et al., 2009, 2013). The ^{210}Pb data, based on a shorter half-life of
664 22.3 yr (Noller, 2000; Faure and Mensing, 2005), provide information about sedimentary

665 deposition for the past ~150 yr. The ^{137}Cs data are based on the half-life of 30.17 yr (Faure and
666 Mensing, 2005), but may have a shorter effective half-life closer to a decade (Robison et al.,
667 2003). The ^{137}Cs age data can reveal the timing of sedimentation after A.D. 1952 (Robbins et al.,
668 1978). We use ^{210}Pb and ^{137}Cs age data to constrain the timing of deposition for the most recently
669 deposited sediments. While ^{210}Pb and ^{137}Cs have similar half-lives, ^{210}Pb input is continuous,
670 while ^{137}Cs input is episodic (Faure and Mensing, 2005); the peak input for ^{137}Cs was during
671 1962–1963 as a result of fallout from above-ground nuclear testing. Nuclear accidents, like
672 Chernobyl, are an additional source of ^{137}Cs (Faure and Mensing, 2005); ^{137}Cs has been detected
673 in seawater (Alam et al., 1996) and sediments (Michels et al., 2003) in the northern Bay of
674 Bengal.

675 In order to evaluate the timing of the possible 2004 turbidite with radiometric techniques,
676 we collected sediment samples below the turbidite at 1 cm spacing. The ^{210}Pb samples were
677 prepared and analyzed at the Institut des Sciences de la Mer de Rimouski (Flynn, 1968; St-Onge,
678 2004; Levesque et al., 2006). Other ^{210}Pb samples and ^{137}Cs samples were prepared and analyzed
679 using gamma counting methods with the assistance of Oregon State University  **“Wheatcroft Lab” at Oregon State University** (Gilmore and Hemingway, 1995; Wheatcroft
680 and Sommerfield, 2005).

682 To estimate the ages of the turbidites using radiocarbon, we extract the calcium carbonate
683 tests of planktic foraminifers preserved in the hemipelagic sediment below each turbidite to
684 provide a maximum limiting age. We utilize planktic foraminiferid species because they most
685 closely represent the age of the youngest seawater, the surface water that is most closely in ^{14}C
686 equilibrium with the atmosphere. We sample below each turbidite because this is the sediment
687 closest in age to the turbidite. We typically do not use the age of the sediment above the turbidite

688 because the boundary between the top of the turbidite tail and the overlying hemipelagic
689 sediment is difficult to identify reliably, and bioturbation is also concentrated at this boundary
690 (methods outlined in Goldfinger et al., 2012a).

691 Sources of sampling error include basal erosion, sediment deformation from coring,
692 differences in stratigraphic thickness between cores, and bioturbation. Some of these factors
693 cannot be evaluated readily because of the coring-induced deformation of stratigraphic thickness
694 and sedimentary structure (aleatory uncertainty; how well the sediment cores represent the real
695 sedimentary thicknesses). Bioturbation is difficult to evaluate as a factor controlling age
696 estimates because we do not have multiple cores in a single location that have both bioturbated
697 sedimentary section and nonbioturbated sedimentary section. Erosion can be estimated in some
698 cases (Goldfinger et al., 2012a), but the tests require multiple cores at a site, and thus we are
699 unable to test this factor due to the lack of multiple cores at most sites. We attempted to estimate
700 erosion using cores that were collected nearby (<10 km); however, some of these were not good
701 candidates due to complex turbidite structure, bioturbation, or coring deformation. These
702 confounding factors made it difficult to distinguish hemipelagic sediment from turbiditic
703 sediment well enough to be useful in our interpretation.

704 Other sources of uncertainty include factors that affect some of our assumptions
705 regarding how well the sediment age actually represents the time of deposition for the turbidite.
706 Sources of this type of epistemic uncertainty include (1) changes in the age of the surficial
707 seawater at the time of deposition; (2) changes in carbon export to the seafloor (rate of
708 foraminiferid sedimentation); and (3) changes in species distribution through time. Changes of
709 the age of seawater can be affected by upwelling, which brings older water to the surface,
710 making the sediment appear older in radiocarbon years. If carbon flux to the seafloor increases

711 during the time frame that the sample thickness represents, the age determination would be
712 biased to an age representing the higher carbon flux (this would change the concentration of
713 foraminiferid tests per unit volume of sediment, biasing the age toward the time that had a higher
714 concentration of foraminiferid tests). If the species distribution changes through time (i.e., if
715 deeper shallow-water species might dominate) the age of the sediment would be different. While
716 we do not think errors 2 and 3 are significant, we do not have sufficient data to evaluate or test
717 these sources of aleatoric uncertainty. Error 1 is discussed in the following.

718 Sediment samples were removed from the cores while avoiding the 0.5 cm of material
719 nearest the core walls to avoid visible or undetected deformation and friction drag along the core
720 walls. In some cases highly irregular turbidite bases resulted in sampling an interval below the
721 basal irregularities. We corrected these ages by subtracting the time represented by the sediment
722 gap. Hemipelagic sediment samples were freeze-dried to separate clay particles to improve
723 rinsing through a sieve, washed in a dilute Calgon (sodium hexametaphosphate) solution to keep
724 the fine particles in suspension, sieved through a 125 μm stainless steel sieve, then dried in a
725 warm oven. Typically 25–50 individual planktic foraminifers (depending on size and mass) are
726 identified and removed from this dried $>125 \mu\text{m}$ size fraction using a fine sable brush moistened
727 with distilled water. Foraminiferal sample ages are determined using AMS methods at the Keck
728 AMS facility at University of California, Irvine, in collaboration with John Southon.

729 Radiocarbon age reporting follows a set of standards (Stuiver and Polach, 1977).
730 **Laboratory** radiocarbon ages are reported in years before present, B.P. (measured from **A.D.**
731 1950) with a 2 standard deviation laboratory error (Stuiver et al., 1998). We used OxCal V 4.2.3
732 to calibrate ^{14}C ages (Stuiver and Braziunas, 1993; Bronk Ramsey, 2009a, 2009b; Reimer et al.,
733 2013). We applied a marine reservoir correction to account for the marine reservoir for marine

734 radiocarbon samples. In addition to the global marine reservoir value, we apply an additional
735 regional correction (ΔR) of 16 ± 78 yr using the IntCal13 and Marine13 databases (Reimer et al.,
736 2013). Only two ΔR values are available for the Sumatra area and these (like nearly all ΔR
737 values globally) are based on latest Holocene ages (located north and south of Sumatra). Squire
738 et al. (2013) used samples along the Abrolhos Islands offshore of Western Australia and found
739 ΔR for the past 3000 yr to be stable and to range from 54 ± 30 yr; their calculations are
740 consistent with estimates made for sites between northwestern Australia and Java, 60 ± 38 yr
741 (Gillespie, 1977; Gillespie and Polach, 1979; Bowman and Harvey, 1983; Bowman, 1985;
742 Southon et al., 2002; Hua et al., 2004, and references therein; O'Connor et al., 2010). The ΔR
743 value for the Cocos Islands, eastern Indian Ocean, is 66 ± 12 yr (Hua et al., 2004). Dutta et al.
744 (2001) suggested that the variation in ΔR in the northern Indian Ocean is due to variations in the
745 thermocline ventilation rates. Hua et al. (2004) suggested that the lower values of ΔR in the
746 eastern Indian Ocean are because surface waters are influenced by seawater from the western
747 Pacific sourced via the Indonesian Throughflow. These ΔR values are stable even given the
748 increased potential variability imparted by ENSO (El Niño Southern Oscillation) and the
749 influence of the western Pacific on the Indian Ocean via the Indonesian Throughflow (McGregor
750 et al. 2008; Yu et al. 2010). The ΔR values decrease in magnitude from south to north, with the
751 lowest values at the northern and southern tips offshore the Island of Sumatra (used in our
752 analysis; Southon et al., 2002). Given the small variation in ΔR found in the eastern Indian
753 Ocean, the relations between the hydrography of these sample sites and the RR0705 core sites
754 (RR0705 core sites are located in places that are less likely to undergo upwelling-induced
755 inflated ΔR values), and the relative stability of ΔR for the past 3000 yr, we consider a maximum
756 possible ΔR of ~ 90 . This ΔR is small when compared to the absolute ages that we use as a

757 chronological framework for our stratigraphic correlations. While constraints are few for this
758 correction and do not extend far into the past, we are correlating marine sites to other nearby
759 marine sites, thus the local correlations are likely similar for each time range, even as the
760 variability from an absolute scale is unknown (absolute ages will contain additional uncertainty).

761 We used a sedimentation rate-based age model that allows estimation of turbidite
762 emplacement ages, accounting for gaps between the sample and turbidite base. We propagated
763 all uncertainties using root mean square (RMS) calculations using estimates of the uncertainties
764 at each step. This calculation included the laboratory uncertainties and resulted in the final
765 reported 95.4% error range for each radiocarbon age (see OxCal code Supplemental File S2). We
766 use a moving average hemipelagic sedimentation rate (see Supplemental File S2 for a more
767 detailed description). This calculation includes the laboratory uncertainties and yields the final
768 reported 95.4% error range for each radiocarbon age. No laboratory multipliers were applied to
769 these data because laboratories now include this uncertainty in their results that was previously
770 accounted for by the laboratory multiplier (Scott et al., 2003[[[Scott et al., 2003 is not in the](#)
771 [reference list. Delete “et al.” here?\]\]\]; Goldfinger et al., 2012a\).](#)

772 **Age Models**

773 We constructed a series of OxCal age models to incorporate stratigraphic information
774 into the age calibrations. OxCal uses Bayesian statistics to incorporate prior information (e.g.,
775 stratigraphic or age progressive information) into the age calibrations (Bayes and Price, 1763;
776 Bronk Ramsey, 2008). OxCal age models are constructed with two components: the model
777 structure (priors) and the age measurements (likelihood). Because age depositional models often
778 have many independent parameters, OxCal uses Markov Chain Monte Carlo (MCMC)
779 simulations to sample age distributions and generate a final distribution (Bronk Ramsey, 2009a).

780 We also build our OxCal age models with nested functions, such as the `Combine` `[[no quotes]]`
781 function (discussed `in the following`).

782 For our OxCal age models, we use two depositional models: Sequence and P_Sequence
783 (Bronk Ramsey, 2009a). The `Sequence` `[[no quotes]]` model considers the stratigraphic order
784 (superposition) of the ages. The P_Sequence `[[no quotes]]` model considers the stratigraphic
785 order and the relative stratigraphic depth. We use the P_Sequence model for age calibrations
786 within cores because we can make estimates of stratigraphic depth within a core. Because the
787 relative depths are different between cores (due to differences in hemipelagic sedimentation
788 rates, lack of erosion correction, and sampling errors), we cannot use P_Sequence, so we use a
789 Sequence model.

790 For the P_Sequence model, we constrain the depth by using the hemipelagic depth for the
791 samples (Bronk Ramsey, 2009a). Because turbidites represent instantaneous changes in
792 sedimentation rate, they do not reflect the long-term sedimentation rate between turbidite
793 emplacements. For this reason, we remove the depth associated with the turbidite thicknesses
794 from the sample depth information. We also use the OxCal `Date` `[[no quotes]]` function to
795 generate synthetic ages for the bases of turbidites that have no direct radiocarbon age sample
796 (Bronk Ramsey, 2001). We apply a ± 0.5 cm sampling error to the depth term in the age model.


797 For our Sequence age model (Bronk Ramsey, 2009a), we use ages from all slope cores in
798 the region of the 2004 SASZ earthquake. There are three ways in which we estimate the age of
799 the correlated turbidites: single ages, combined ages, and synthetic ages. Some correlated
800 turbidites have only a single radiocarbon age determination and this is the age we include in our
801 model. For correlated turbidites that have multiple ages, we use the OxCal Combine function
802 (Bronk Ramsey, 2001). We use our stratigraphic correlations to determine which laboratory ages

803 to consider for all age Combines. The Combine function takes the laboratory age Gaussian
 804 distributions and combines these distributions. OxCal performs tests to evaluate how well the
 805 combined ages fit their combined age distributions. We discuss ways in which we discriminate
 806 ages that do not pass these tests of best fit. The results of these tests are included in the log file
 807 (Supplemental File S2). As with the P_Sequence model, for turbidites that do not have
 808 radiocarbon age determinations, we generate synthetic ages with the OxCal Date command.

809 We also provide temporal limits to the posterior age distributions with the OxCal
 810 **Boundary** [] function (Bronk Ramsey, 2008, 2009a), a **“prior.”** [] **ould this be a**
 811 **priori, or Prior? Other functions are initial uppercase letters.**] We place a Boundary at the
 812 **beginning** [] of the model (oldest) so that the modeled age determination for the
 813 earliest age does not significantly extend into the past. OxCal boundaries exert a temporal
 814 limitation to the output probability density functions of the calibrated ages by limiting the age
 815 range of the probability density functions. We place a Boundary at the **end** [] of the
 816 model (youngest) because the sediment cannot be younger than **A.D. 2007**, the year the sediment
 817 was collected. We use these Boundary functions in the P_Sequence and Sequence age models.


818 The Combine function calculates a chi-squared test to determine if the sampled ages
 819 represent the same age population. For each Combine, a T value is given and a threshold value is
 820 given. If the T value rises above the threshold value, the Combine fails the chi-squared test. The
 821 Combine function also calculates agreement indices, as described **here**. While this is simply an
 822 analytical test that ignores geologic variability, it remains a useful filter in the absence of other
 823 prior information.


824 The P_Sequence and Sequence analyses, as well as Combine functions, use MCMC
 825 simulations to determine the degree to which the prior model agrees with the observations (in

826 terms of likelihoods) with the agreement indices, A , A_{comb} , A_{model} , and A_{overall} ; A identifies which
 827 samples do not agree with the model; A_{comb} tests whether the distributions can be combined.
 828 A_{model} tests to see if the model can be used given the ages used in the model. A_{overall} is a product
 829 of the other agreement indices. In order to pass, OxCal agreement indices should be $>60\%$
 830 (Bronk Ramsey, 2008); this represents the area of overlap of the  **able document format files**.
 831 We adopt these criteria in our age models.

832 When OxCal age Combines fail the chi-squared and agreement index tests, we remove
 833 outliers manually as an iterative process (Bronk Ramsey, 2009b). We first include all ages for
 834 potentially correlated strata. When tests fail, we examine the geologic context and manually
 835 remove the most probable outlier to examine whether failure was due to the outlier, or lack of
 836 good fit among the tested group (Bronk Ramsey, 1995, 2009b). We begin with the ages that have
 837 the lowest agreement index or are clearly older outliers.

838 **Lithostratigraphic Correlation**

839 We use integrated stratigraphic correlation techniques, including visual lithostratigraphic
 840 description (color, texture, and structure), CT image analysis, and lithostratigraphic log
 841 correlation of multisensor core logging (MSCL) geophysical data (Fukuma, 1998; Karlin et al.,
 842 2004; Abdeldayem et al., 2004; St-Onge et al., 2004; Hagstrum et al., 2004; Waldmann et al.,
 843 2011) to correlate turbidites based on the turbidite **architecture**  **notes** (Amy and Talling,
 844 2006). Stratigraphic correlation using geophysical signatures representing vertical turbidite
 845 structure is a primary tool for testing individual deposits for their areal extent, a significant part
 846 of the criteria used to discriminate seismoturbidites from other possible types. A positive
 847 correlation, regardless of the originating details, is indicative of a cogenetic origin. Downcore
 848 geophysical properties for individual turbidites are reflections of the vertical grain-size

849 distribution of the bed (Kneller and McCaffrey, 2003; Amy et al., 2005; Karlin and Seitz, 2007;
850 Goldfinger et al., 2012a). Lithostratigraphic correlation techniques have been used to correlate
851 stratigraphic units since the 1960s (Prell et al., 1986[[Added  t al." to match reference list.]];
852 Lovlie and Van Veen, 1995). In detail these fingerprints represent the time history of deposition
853 of the turbidite and, in several cases linked to plate boundary earthquakes, have been shown to
854 correlate between independent sites separated by large distances and depositional settings
855 (Goldfinger et al., 2008, 2013b). The turbidite is commonly composed of single or multiple
856 coarse fraction fining-upward stacked units termed pulses. The rarity of a fine tail (Bouma Td
857 and Te units; Bouma, 1962) or subsequent hemipelagic sediment between pulses indicates that
858 there is commonly little or no temporal separation between units. The lack of temporal
859 separation of the pulses in Cascadia has been inferred to represent deposition over minutes to
860 hours, so most likely represent subunits of a single turbidite (Goldfinger et al., 2012a). We
861 combine all these correlation tools when possible. The more tools that can be applied to an
862 individual prospective correlation, the more robust the interpretation will be.

863 The most sensitive criteria for correlating fine-grained turbidites (which may not be
864 visible to the naked eye) is the density profile (Inouchi et al., 1996), which we augment with very
865 high-resolution CT density profiles and three-dimensional CT imagery. In the RR0705 cores,
866 density and MS tend to covary with particle size; larger particles and magnetic minerals are
867 generally denser (Thompson and Morton, 1979). An exception to this is tephra; while tephras
868 have larger MS values, they are not denser than the overlying or underlying hemipelagites. The
869 other MSCL data (P-wave velocity) were less effective because the sensors do not make
870 sufficient contact with the core liner, so there are large gaps and excursions in the data.

871 Resistivity shows a longer wavelength response to the sedimentary structure than the other
872 geophysical data, so much so that we do not use this proxy (Fig. 2).

873 We verified the efficacy of the geophysical data as a grain-size proxy for the Sumatra
874 lithologies with particle size analysis (cores 96 and 55; Fig. 2). In our figures, core geophysical
875 data are plotted versus depth from left to right [gamma density, CT density, point MS (PMS),
876 MS]. Core particle size data are plotted versus depth from left to right (mean, median, mode, and
877 d10, the particle size for which 90% of the particles are larger). For these cores exclusively, we
878 plot resistivity (RES, in ohms) versus depth. Local maxima in particle size data match with local
879 maxima in the geophysical data.

880 We distinguish between multipulse turbidites and a series of closely spaced single pulse
881 turbidites with some sedimentologic and geophysical criteria. When there is hemipelagic
882 sediment between coarse pulses (lack of fine laminations, presence of oxidation), those pulses
883 are from turbidites that were deposited at different times, time separated as evidenced by the
884 hemipelagic sediment or oxidation. In some cases it is difficult to distinguish between single-
885 pulse and multipulse turbidites in this way, so we use the core geophysical data. We use the same
886 criteria developed in Goldfinger et al. (2012a), by which background sedimentation typically has
887 a lower geophysical (CT and gamma density; MS) value and the turbidites have higher values,
888 verified by direct observation, color change, lithic smear slides, and micropaleontology.
889 Turbidites that have coarser bases and fine upward have geophysical data that have larger values
890 at the base and lessen upsection until the values reach that of the background hemipelagic
891 sedimentation. When there are multiple coarse pulses, there are geophysical maxima for each
892 coarse pulse that plot above the background geophysical values. A good example is T-20 in core
893 104PC. The CT and true color (red-green-blue, RGB) imagery shows four main coarse pulses

894 and two finer pulses in the tail. The CT density plot also shows these four main and two minor
895 pulses; each of the pulses coarsen upward. The PMS data show how these pulses progressively
896 decrease in magnitude toward a background value and are the main evidence that T-20 is a
897 multipulse turbidite in core 104PC. In core 103PC, T-20 does not have the detailed structure that
898 is found in core 104PC, so we rely on the structure in core 104PC in this case.


899 We distinguish between individual single-pulse or individual multiple-pulse turbidites
900 from a series of stacked single-pulse or multiple-pulse turbidites using sedimentologic
901 characteristics. We consider characteristics of deposits within a single core, as well as these
902 characteristics from adjacent cores where they are likely correlated. Local variability is inherent
903 in these and all geologic records, thus the determination of single versus multipulse turbidites
904 may not be apparent in all examples, but is taken from the best example of each bed in a
905 correlated series. A detailed example of this was given in Goldfinger et al. (2012a or
906 2012b or both?). All correlated turbidites therefore inherit the classification from the best
907 example of turbidite beds that are correlated along strike. We list the characteristics used to
908 constrain turbidite deposition timing and sedimentation characters, and classify turbidites into
909 three categories based on the following criteria.

910 *Turbidite Classification Criteria*

- 911 1. Impulsive base (IB): coarser sediment overlying finer sediment with a sharp (<1 mm)
912 lithologic contact with fine-grained underlying sediment.
- 913 2. Erosive base (EB): evidence for an unconformity at the base of the turbidite, due to
914 erosion during turbidite emplacement; may be evident as an angular and/or irregular base.
- 915 3. Underlying hemipelagic sediment (UHS-RGB): hemipelagic sediment is lighter in
916 color than turbiditic sediment; this can be seen visually and in the RGB imagery.




917 4. Underlying hemipelagic sediment (UHS-CT): hemipelagic sediment is massive (lacks
918 laminae) and low in density; this can be seen visually in the CT imagery.

919 5. Underlying brown oxidation laminae (UBOL): oxidation of sediment at the seafloor is
920 not instantaneous and represents a time period much longer than the time required for the
921 deposition of a turbidite. If there is oxidation between two turbidite beds, they are possibly (but
922 not necessarily) the result of separate turbidity currents. Such contacts must be distinguished
923 from oxidation fronts which move through the core with time.

924 6. Geophysical property relation (GPR): at least one of the core geophysical properties
925 match the typical vertical profile of a typical turbidite-hemipelagite pair. The profile of a typical
926 turbidite shows at least one maximum associated with a density or particle size increase at the
927 base of the turbidite, with an upward decrease in value associated with the turbidite tail, and a
928 further diminishing value to a background value associated with the hemipelagite. 

929  ***Evidence for Sediment Loading Structures (SLS)***

930 We define three classes of beds based on these criteria: (1) more certainly a single-pulse
931 or a multipulse turbidite; (2) less certainly a single-pulse or a multipulse turbidite; (3)
932 indeterminately a single-pulse or multipulse turbidite (or possibly not a turbidite).

933 Category 1 includes turbidites that satisfy four of the **seven criteria**  **by 6 criteria**
934 **listed (numbered for clarity); delete “seven”?** we list. Based on these multiple criteria, we
935 find that there is a highest likelihood of the bed being a single turbidite. If three of the **seven**
936  **?** criteria we list **below**  **?** are met, then we are less certain with our interpretation
937 and place the turbidite into category 2. If fewer than two criteria are met, we place the
938 sedimentary deposit into category 3. Our preferred correlations are composed of category 1 and

939 category 2 turbidites, but not category 3 turbidites. Some beds may be included in category 3 if
940 they are incomplete, particularly at the base.

941 We make extensive use of industry techniques known as flattening and ghost tracing [no
942 quotes]] to examine turbidite sequences for correlation or lack thereof. Flattening core data to
943 particular stratigraphic horizons (Major et al., 1998) is a test of the hypothesis that the
944 stratigraphic sequences in the cores correlate and represent the same sedimentary history. This
945 hypothesis can be tested with unlimited combinations of cores and requires only the assumption
946 that the turbidite deposition consumes zero time. In practice, this is accomplished by the use of
947 ghost geophysical traces from different cores that are iteratively compared to search for the
948 presence or absence of a similar stratigraphic sequence. If correlations are found that satisfy the
949 radiocarbon temporal constraints, a proposed sequence is then flattened, that is all of the
950 geophysical and image data in the core diagram are hung [no quotes]] on proposed uniform
951 time horizons, represented by the bases and tops of each turbidite. The proposed correlation lines
952 are then horizontal, or flat. This is accomplished by changing the vertical scale of each core to
953 match a reference core. The thicknesses of the turbidites naturally vary between cores at a single
954 site and between cores from different sites for a variety of reasons. Because turbiditic and
955 hemipelagic sedimentation rates vary for cores at different sites, the thicknesses of stratigraphic
956 units also vary for those core sites. It is this variability in stratigraphic thickness that is removed
957 when several core sequences are flattened, scaling the core data to match these variations in
958 thickness and sedimentation rate and placing the cores on a time basis in the vertical axis
959 (Tearpock and Bischke, 2002) This allows the interpreter to see the stratigraphy as if there were
960 a simple pancake stratigraphy with the first-order depositional variability largely removed and
961 the characteristics of each bed emphasized

962 **Application to Sumatra**

963 We review the rationale developed for the attribution of seismogenic triggering of
964 turbidity currents in Cascadia and elsewhere modified here in our investigation of the
965 stratigraphy offshore of Sumatra.

966 Distinguishing seismoturbidites from turbidites triggered by other mechanisms can be
967 very difficult, and in some cases impossible. Two approaches can be applied, separately or in
968 concert, to make this distinction: (1) sedimentology of the deposits, and (2) correlation of
969 deposits to establish regional synchronous deposition unlikely to be caused by processes other
970 than earthquakes. The principle basis for attributing a seismogenic trigger to a regionally
971 extensive synchronously deposited bed is that regional and synchronous deposition is unlikely to
972 have been generated by a trigger other than an earthquake (Goldfinger et al., 2007, 2008, 2012a;
973 Patton et al., 2013a).

974 Radiocarbon is used to establish the chronostratigraphic framework; however,
975 radiocarbon ages cannot be used to establish synchronous deposition because the uncertainties
976 generally preclude this; they can be used to establish consistency, but not synchronicity.
977 However, synchronicity need not mean establishing the exact timing of events at multiple sites;
978 the requirement is to test whether or not the deposits were laid down at the same time. To do this,
979 we use relative age tests, lithostratigraphic correlation methods, and comparisons of turbidite bed
980 sequences at isolated sites to assess whether turbidites are likely the same turbidite, or sequence
981 of turbidites, deposited at the same time, individually or in sequences. Note that this does not
982 require a physical connection between turbidites at isolated sites, which may or may not exist.
983 Such turbidites may be deposited synchronously at isolated sites by a common trigger, without a
984 physical connection.

985 **Relative Age Tests**

986 One way to examine turbidite sequences for synchronous deposition includes the
 987 **confluence test**, **[[no turbidites]]** and Cascadia turbidites pass **this** test (Adams, 1990; Goldfinger et
 988 al., 2003, 2007, 2008, 2012a). This test poses that if the channel system has the same number of
 989 turbidites above and below a confluence, the deposits in all locations were laid in the same short
 990 period of time lasting minutes to hours (Goldfinger et al., 2012a). Because of this similarity in
 991 stratigraphy between cores in this example, the researchers conclude that the trigger for these
 992 turbidity currents likely affected a broad region (**thousands of square kilometers**). This test was
 993 applied to Cascadia (Goldfinger et al., 2012 **[[2012a 2012b or both?]]**), the northern San
 994 Andreas (Goldfinger et al., 2007, 2008), Japan (Nakajima and Kanai, 2000), and Chilean lakes
 995 (VanDaele et al., 2014). Similarity of sequences can also be compared between isolated basin
 996 sites **that**, **[[correct? not “with”]]** like the confluence test, should not have very similar
 997 sequences if the triggering mechanisms are neither regional nor synchronous.

998 **Isolated Sites and Synchronous Deposition**

999 Well-log correlations between sites in Cascadia have been used to test links between
 1000 sites. In support of findings, Goldfinger et al. (2003, 2008, 2012a) correlated turbidites in cores
 1001 that sample unique source areas (Cascadia **Seachannel** with Juan de Fuca Canyon and **Hydrate**
 1002 **ridge basin west** **[[not a formal name in GEBCO; should it be Hydrate Knolls?]]** with Rogue
 1003 **canyon** 250 km southward along strike), a correlation test independent of the confluence test that
 1004 further supports the areal extent of the trigger for these turbidites.

1005 **Controls on the Physical Structure of Turbidites and Log Correlation**


1006 The detailed depositional structure of turbidites is likely a combination of several
 1007 turbidity current forcing factors. **B**ecause turbidite deposition is a sedimentary result of the

1008 passing turbidity current, the forcing factors probably also control the structure of the turbidite.
1009 Factors that promote allocyclic forcing (i.e., sedimentation and erosion controlled by the source
1010 or input of sediment flux; Underwood et al., 2005) can include the source of the initial landslide,
1011 such as whether the turbidity current is from hyperpycnal flow or a seismogenically triggered
1012 landslide (Seilacher, 1969; Shiki et al., 2000; Mulder et al., 2003; Goldfinger and Morey, 2004;
1013 Garrett et al., 2011; Goldfinger et al., 2012a, 2012b). Factors that promote autocyclic forcing
1014 (i.e., sedimentation and erosion controlled by local or site processes) include flow dynamics, site
1015 geomorphology, and proximity (Middleton, 1967; Nelson et al., 1986; Muck and Underwood,
1016 1990; Kneller and McCaffrey, 1995; Kneller and Buckee, 2000; Baas et al., 2004, 2005; Amy et
1017 al., 2005, 2006[[Should this be "Amy et al., 2005; Amy and Talling, 2006"?]]; Dennielou et
1018 al., 2006; Felix and Peakall, 2006). These forcing factors may compete depending upon core
1019 location, local physiography, and distance to the source region of the turbidity current. If trigger
1020 source forcing dominates over a sufficiently large region, turbidites deposited by those turbidity
1021 currents that share this common forcing may also share a common turbidite structure. As a result,
1022 these turbidites may also share a common fingerprint. Although we may not yet know precisely
1023 why correlation is effective in detail, if a strong correlation can be established, it can be used to
1024 link deposits, or to show lack of evidence for links.

1025 As in prior work done in Cascadia (Goldfinger et al., 2012a), we use lithostratigraphic
1026 correlation of geophysical logs as discussed **herein** to test for potential links between basin sites
1027 with radiocarbon support, between basins and the trench (with radiocarbon in the basin only),
1028 and between trench sites that lack radiocarbon support. In addition to individual turbidite
1029 correlation, we consider sequences of turbidites, supported by turbidite mass, ages, number of
1030 coarse pulses, geophysical log signatures, and the number of turbidites above or between


1031 external chronostratigraphic datums (e.g., the Mazama ash or a Pleistocene-Holocene faunal
1032 boundary; Griggs and Kulm, 1970). Turbidite sequences may comprise a unique series of
1033 turbidites identifiable using any or all of these features. The linking of a turbidite series, as with
1034 individual turbidite correlations, was used in Goldfinger et al. (2012a) to correlate turbidites
1035 along strike; that correlation information was used to estimate the rupture length of the causative
1036 earthquakes. CHIRP subbottom profiles are used at this stage to assist in comparison of
1037 stratigraphic sequences. These subbottom profiles provide us with the ability to look deeper in
1038 the sedimentary section than is reachable by our cores. The 20–25 cm resolution of these profiles
1039 (verified with the core data) is capable of imaging many of the larger turbidite beds, to establish
1040 consistency of stratigraphy within a depocenter, and for intersite comparison.



1041 Because of the difference in basin and site effects and turbidite channel architecture
1042 between Sumatra and Cascadia (Patton et al., 2013a), the tests for seismogenic triggering are
1043 slightly different. As in Cascadia, we base our correlations largely on three factors: (1)
1044 sedimentary source isolation, (2) deposit geophysical property fingerprint, and (3) timing or age
1045 control. Sumatra cores in slope basins are isolated from each other and most of them are
1046 completely isolated from terrestrial or shallow-water sediment sources, so links between them
1047 are used as a primary way to test for regionality of triggers. Most alternate triggers, such as
1048 hyperpycnal flow and wave loads, fail this simple test because these mechanisms do not affect
1049 regions of thousands of square kilometers or hundreds of kilometers along strike.

1050 Turbidites and turbidite sequences are compared between sites using the criteria here.
1051 Turbidites and turbidite sequences that satisfy all or most of the criteria herein are considered
1052 correlated to varying degrees as indicated by the line symbols  on the plots. If turbidites can be
1053 correlated between cores across a sufficient distance with high confidence, we assign a T-number

1054 to that correlation. There are additional turbidites in our cores that fail these tests to a degree that
1055 they are not considered correlated.

1056 **RESULTS**

1057 Slope sites used in this study include cores 109, 108, 104, 103, 102, 97, 96, 95, and 90,
1058 **all of** which have isolated sediment sources. In the trench, cores 03, 05, 107, 105, 99, 98, 94, 93,
1059 and 88 receive sediment from both upstream (up trench  **notes**) in the trench and from
1060 downslope transport from the continental slope (Patton et al., 2013a). **Figure** 3 shows the
1061 possible source areas and flow relations for the cores that we primarily use for our correlations
1062 (all regional cores are shown in **Supplemental File S3³**).

1063 We placed core sites in both trench locations and continental slope basin locations. Core
1064 locations are given in Table 1 and shown in **Figures 1 and 3 and** Supplemental File S1.  The light
1065 gray (in CT imagery) sand bases of turbidites are easily identified and MSCL maxima in gamma
1066 density and **MS** correlate well with the CT density maxima (Fig. 3H). We note that the spatial
1067 resolution of the various geophysical traces varies with the thickness, volume, density, and
1068 magnetic content of the turbidites (see **discussion of** methods). The high-resolution CT data
1069 represent finer detail than do the **gamma density and magnetic data**. While all data are registered
1070 on the same vertical scale, there are some vertical differences in the apparent position of features
1071 in the cores stemming from geophysical **edge effect**,  **notes** in addition to small changes
1072 in the cores over the several years of data collection.

1073 The lithostratigraphy in the northern Sumatra slope and trench cores is dominated by
1074 turbidites interbedded with massive hemipelagic mud and less common tephtras. Bioturbation is
1075 common and core-induced deformation is observed in some cores. Turbidites are composed of
1076 coarse silt to coarse sand bases, occasional ripup clasts, and fining-upward sand and silt to clay

1077 subunits; slope cores have abundant forams. The coarse fraction is composed of mica and quartz
 1078 grains with rare mafics, consistent with a Himalaya source from the accreting Bengal and
 1079 Nicobar fans (Stow et al., 1990). Basal turbidite subunits are composed of primarily
 1080 foraminiferal hash in some piggyback basin cores. Sand subunits commonly range in thickness
 1081 from 0.5 to ~20 cm, are parallel laminated and cross-laminated, and commonly underlie massive
 1082 sand beds. Finer material is composed of silt- to clay-sized particles (Fig. 2). Primary tephras
 1083 0.5–10.5 cm thick are rare and can be correlated between sites using electron microprobe and
 1084 laser ablation inductively coupled plasma mass spectroscopy data (Salisbury et al., 2010, 2012).
 1085 Turbidite stratigraphy with these general characteristics is found in all slope basins (cores 108,
 1086 104, 103, and 96) and trench sites (cores 107, 105, 98, and 94), spanning 230 km along strike.

1087 We describe the turbidite structure in the RR0705 cores using Bouma (1962), van der
 1088 Lingen (1969), Stow (1977), and Piper (1978) fine-grained classification system divisions, and
 1089 label the sedimentary layers according to these systems (Stow, 1985; Fig. 4A). A complete
 1090 Bouma sequence (Bouma, 1962) would comprise superposed divisions Ta, Tb, Tc, Td, Te, and
 1091 F. Stow and Piper (1984) divisions fit within the Bouma division Te, in superposed order, E1,
 1092 E2, E3 or T0, T1, T2, T3, T4, T5, T6, T7, and T8. The complete sequence, for either division
 1093 scheme, is not typically found in most turbidites.




1094 We show typical turbidites, some multipulse, from cores 96PC and 108PC in Figure 4B.
 1095 Multipulse turbidites may have superposed and repeated divisions (e.g., core 108, 12–294 cm:
 1096 Tc-d, Td, Tc, T3, T6, T7) or just superposed divisions (e.g., core 108, 291–280 cm: Td, T3, T4,
 1097 T7). **[[no core designations, i.e., 108PC, etc.?]]** All multipulse turbidites have multiple maxima
 1098 in the geophysical data (commonly reflecting grain-size variations) that correspond to the
 1099 structural divisions.

1100 We analyzed 46 radiocarbon ages and 37 ²¹⁰Pb samples for the cores within the 2004
1101 SASZ earthquake region. Table 2 lists the ¹⁴C ages used in our OxCal age models and includes
1102 the laboratory age (in radiocarbon years), calibrated age (calendar yr before present, or A.D.
1103 1950, i.e., cal yr B.P.), and the moving average hemipelagic sedimentation rate for that sample.
1104 The sample name is a compilation of the cruise name, the core number and type, the sample
1105 interval (in centimeters), and the sample number. We use the sample name in OxCal to track core
1106 and stratigraphic information through the age modeling. Calibrated ages are plotted in core
1107 figures and are used to establish the framework for lithostratigraphic correlation. We found no
1108 age inversions (where older ages superpose younger ages) in these age data that span the middle
1109 to late Holocene.

1110 **Surficial Turbidite in the 2004 Rupture Zone**

1111 The uppermost turbidite in 21 cores (01GC, 05PC, 26GC, 88TC, 87PC, 87TC, 93TC,
1112 94PC, 95PC, 96PC, 96TC, 97MC, 99MC, 102MC, 104PC, 104TC, 105TC, 107PC, 108PC,
1113 108TC, and 109MC; and second uppermost turbidite in two cores (93TC and 88TC) share
1114 common characteristics suggesting recent deposition based on the lithostratigraphic descriptions,
1115 radiometric age estimates, and relative age evaluations (GC, gravity core, PC, piston core; TC,
1116 trigger core; MC, multicore; Supplemental Files S1, Se). Five cores do not appear to contain the
1117 complete uppermost deposit and just have the base of what may be the 2004 deposit (01, 26, 104,
1118 107, and 108). It is not possible to evaluate the completeness of the section in six cores due to
1119 coring deformation (05, 88, 93, 94, and 109). One core set has a complete deposit when adjacent
1120 cores 96PC, 96TC, and 97MC are composited. Two additional cores may have the entire deposit
1121 (93TC and 88TC; Supplemental File S3). Sediment in 96PC and 96TC is deformed and
1122 compressed in places, so it is difficult to assess the true thickness of the turbidite in these cores.


1123 Core 102MC may also have the entire turbidite section, though in a thinner deposit (~6 cm thick;
1124 Supplemental File S3).

1125 We use core 96  **[[labeled 96TC, 96PC above; which is correct?]]** for our discussion of
1126 the sedimentologic characteristics because it is probably complete and has the most expanded
1127 section of young uppermost deposit, though many of these sedimentologic qualities (e.g., the
1128 unconsolidated soupy nature of the uppermost turbidite) are shared in all  18 cores. We scale the
1129 TC to the PC based on common stratigraphic contacts, resulting in an estimated thickness of 308
1130 cm (Fig. 5). We could not determine if multicore 97MC included sediment missing from the top
1131 of 96TC, so we did not use this core in our composite estimate of sedimentary thickness. Core 96 
1132 **[[labeled 96TC, 96PC elsewhere; need suffix?]]** is located in an enclosed basin (Fig. 6A) and
1133 has an extensive record of the uppermost turbidite as revealed by CHIRP seismic data collected
1134 in a cross-basin transect (Figs. 6A, 6B). In this core the uppermost turbidite is described as soupy
1135 and water laden (lithologic notes, 120 cm, 170 cm; Fig. 5A). The water content was so high that,
1136 during the shipboard lithologic description, care was required to prevent the sediment from
1137 pouring out of the core when placed horizontally. The reflectivity of the RGB image is consistent
1138 with these observations (the wet sediment is shiny, especially noticeable between 5 and 10 cm).
1139 The uppermost sedimentary deposit consists of a multipulse, upward-fining, quartz-mica,
1140 medium sand to silty clay turbidite. The turbidite has three main pulses, with additional smaller
1141 pulses, as evidenced in the particle size, CT density, gamma density, CT imagery, and
1142 sedimentary texture data (Fig. 5A). The three main pulses are resolvable in these seismic
1143 reflection data (brown dots; Fig. 6B). We classify the turbidite structures (Figs. 5A, 5B) with the
1144 same system as in Figure 4A. There is little to no bioturbation in the top of the deposit, possibly
1145 indicating minimal postdepositional time before collection (Fornes et al., 2001). There is no

1146 oxidation in the surficial sediment, which may also indicate relative postdepositional time.
1147 Oxidation of surficial sediments commonly takes months to a few years (Sayles et al., 1994;
1148 Martin and Sayles, 2003) and was not present at the time of collection, 2.5 yr after the 2004
1149 earthquake. Foraminifera are absent in surficial sediment in this and other cores, indicating a
1150 probable lack of hemipelagic sediment at the surface. We see no evidence of hemipelagic
1151 material overlying the young deposit in cores 94, 96, 97, 99, 102, and 109, while cores 01, 05,
1152 26, 88, 93, 95, 99, 104, 107, and 108 are likely missing their tops and offer no constraint on the
1153 presence of hemipelagic sediment at the surface (Supplemental File S3).

1154 The base of the turbidite has some interesting characteristics that may reveal details about
1155 the nature of deposition (erosional versus depositional) and length of time of deposition (rapid or
1156 slow). The lowermost laminations include embedded mud clasts, possibly of the underlying
1157 sediment. The basal contact of the turbidite shows further evidence of the turbidite penetrating
1158 the underlying mud in scours or intrusions. The shape of the basal contact also suggests that the
1159 turbidite loaded the underlying mud (i.e., pushed downward, deforming the upper contact of the
1160 underlying mud).

1161 It is remarkable that the CT density of the coarse section of the 102MC uppermost
1162 turbidite is quite similar to the geophysical data from core 96PC (Figs. 3 and 5). In the trench,
1163 downtrench and south of the 2004 earthquake slip zone, cores 88TC and 93TC contain turbidites
1164 that also appear to have similar structure (three upward-fining subunits, reflected by the
1165 geophysical proxies) to that found in core 96PC (Supplemental File S3).

1166 We also use core 96  [96PC?] to present an example of our turbidite classification
1167 system. We plot a portion of core 96PC that has turbidites of all three classes (Fig. 5E). The core
1168 data are shown as in the other cores. The class is designated by the relative percent gray of

1169 rectangles to the left of the core imagery data. For each turbidite, we list, by number, the criteria
1170 that are satisfied. We also outline and label the locations in the core where our observations
1171 support the criteria. These criteria are color coded. Turbidite classifications are shown for this
1172 and other cores in Supplemental File S3.

1173 **Age Constraints**

1174 Core 96PC and core 102MC were among the better candidates for age dating. We did not
1175 sample beneath the uppermost turbidite in cores 108 and 104 because the CT imagery shows
1176 evidence of erosion and stratigraphic (possibly coring) disturbance. Nevertheless, there remains a
1177 thin turbidite between the radiocarbon sample and the uppermost turbidite in core 96. **[[96PC?]]**
1178 Age determinations and calibrations for these two cores are given in Table 3. We report the
1179 laboratory age (radiocarbon facility reported age), the simple calibrated age (a gap correction age
1180 model), the Sequence age (age model for within the cores for 96PC and 102MC), and the
1181 P_Sequence model (a second age model for within the core for 96PC). Core 102MC is not a
1182 candidate for a P_Sequence model because there is only one age sample. Laboratory ages are
1183 reported to 20% error and calibrated ages are reported to 95.4% error. The simple calibrated age is
1184 only constrained by the priors accounting for the correction for the thickness of the overlying
1185 hemipelagic sediment between the sample and the event base. The Sequence age is only slightly
1186 better constrained with the priors of stratigraphic order and the collection time as a boundary, so
1187 the boundary priors do not substantially affect the results. The age calibration that includes the
1188 most prior information is the P_Sequence age, including stratigraphic position and stratigraphic
1189 order. The stratigraphic position in the event-free (hemipelagic) sedimentary sequences adds a
1190 strong prior constraint and is responsible for the narrower uncertainties.

1191 We do not prefer any single age model over another, but all their uncertainty ranges span
1192 recent decades, including the year 2004. The age ranges (relative to A.D. 1950) for these three
1193 models are: calibrated model age: 20 ± 60 (A.D. 1980 ± 60 , core 96PC) and Sequence model:
1194 50 ± 160 (A.D. 1900 ± 160 , core 96PC, and A.D. 1890 ± 150 yr, core 96PC). The model ages for
1195 core 102MC result in slightly older ages of 40 ± 40 for the simple calibrated, and 50 ± 60 for the
1196 Sequence model (Table 3). The 102MC age models include a gap correction, thus if the
1197 sedimentation rate is slightly underestimated, the age results would be older, and younger if
1198 overestimated.

1199 We also used the exponential decay of ^{210}Pb activity with depth, and in the presence or
1200 absence of ^{137}Cs , indicative of deposition since 1952, to evaluate the timing of deposition for
1201 these uppermost sediments. Sediment from cores 94PC and 105PC were analyzed for ^{210}Pb and
1202 ^{137}Cs activity using gamma counting (see discussion of methods). Results are plotted in Table 4A
1203 and Figure 7. Sediments from cores 96PC, 96TC, and 102MC were analyzed for ^{210}Pb activity
1204 using the other gamma counting system (described in methods). Results are plotted in Table 4B
1205 and Figure 7. No ^{137}Cs activity was detected in core 94PC or core 105PC. The absence of ^{137}Cs
1206 can be interpreted as either decay below detection limits, implying a very young age, or simply
1207 that not enough material was initially present; the presence of ^{137}Cs in the Southern Hemisphere
1208 is reportedly patchy, so this is a distinct possibility (Alam et al., 1996).

1209 Each of the five sampling sequences show evidence of excess ^{210}Pb activity underlying
1210 the uppermost turbidite in these cores, indicating deposition within at least the past 150 yr. The
1211 spacing of samples in 94PC and 105TC was chosen simply to test for the presence or absence of
1212 ^{137}Cs and ^{210}Pb . Both cores show evidence of recent deposition. We improved our sampling
1213 strategy for analyzing the age in 96PC, 96TC, and 102MC by sampling directly beneath the

1214 turbidites in depth-adjacent sample locations. Cores 96PC and 102MC show exponential decay,
 1215 but 96TC does not, suggesting the lowermost sediment sampled in 96TC is very young and
 1216 probably mixed.


1217 **Regional Lithostratigraphy Within the 2004 Rupture Zone**

1218 In Figure 8 and Supplemental Files S3 and S10¹⁰  **[[Supplemental File S10 is cited out of**

1219 chronological order. Please call out Files S4–S9 before S10 or renumber the files. The

1220 callouts are highlighted to help with this process.]] we show the compilation of 43 turbidites


1221 across the 2004 rupture area. Figure 8 and Supplemental File S3 show these at true vertical scale;

1222 Supplemental File S10  is a working diagram with the turbidite sequence flattened to key

1223 horizons in the sequence. Tie line line-weight thicknesses and patterns on the plots reflect our

1224 confidence in individual ties based on the individual and stratigraphic sequence log correlations,

1225 age similarity, and number of sites correlated. Of these 43, 28 are found in core 108, 39 are in

1226 core 105, 36 are in core 104, 43 are in cores 102 and 103, and 17–18 are in core 96PC. **[[why no** 

1227 suffixes for core designations (PC, etc.)?]]The correlation framework is based on four primary

1228 factors: (1) the turbidites are in similar stratigraphic sequence; (2) the turbidites comprise

1229 distinctive subgroups of beds observed at multiple sites; (3) the turbidites have shared

1230 fingerprints with distinctive details; and (4) they have compatible timing based on radiocarbon

1231 ages. The turbidite structure or fingerprint varies among the turbidite beds. Those beds or

1232 subgroups of beds with particularly distinctive signatures anchor the correlation, defining the

1233 more confident ties, while others that are less distinctive but still in a consistent temporal and

1234 stratigraphic sequence are shown with lower confidence symbols. The superposition and

1235 sequence of these deposits with unique signatures provides boundary conditions within cores,

1236 between cores (PC and TC pairs) and between core sites. When turbidites can be correlated



1237 between cores 96, 103, and 104 or from 103, 104, 105, and 108, **[[why no suffixes for core**
 1238 **designations (PC, etc.)?]]** representing a strike length longer than accretionary prism faults
 1239 (Kopp et al., 2008), they are given a T-number. There may be additional correlatable turbidites,
 1240 but they do not have geophysical signatures sufficient to uniquely identify them. Figure 8 shows
 1241 that the strongest correlated deposits include regional turbidites T-1–T-12, T-16, and T-18–T-21
 1242 (boldest tie lines). Of these, key correlated beds designated T-1, T-3, T-4, T-10, T-21, T-27, T-
 1243 34, T-39, and T-42 and T-43 are the distinctive beds highlighted in Supplemental File S10, and
 1244 those to which the regional stratigraphy has been flattened. Supplemental File S10 represents
 1245 conversion of the vertical scales to time scales, with each bed representing a time horizon.

1246 Cores 104, 103, and 96 **[[should all these cores have designations, i.e., 104PC, etc.?]]**
 1247 are in sedimentologically isolated slope basins and core 105 is in the trench (Fig. 3A). Together
 1248 these cores span ~170 km of the margin. Core 104 source areas may be somewhat shared with
 1249 core 105, but a landward-vergent fold in the trench probably isolates 105 from these sources.
 1250 Figure 9 shows an example of how the turbidites are tested for correlation from core to core. For
 1251 each sequence, there are two panels: (1) the unscaled cores and (2) the flattened geophysical
 1252 properties and flattened CT imagery. The unscaled core figures are vertically clipped versions of
 1253 the main core figures, clipped to the stratigraphic section of interest. From left to right, the core
 1254 figures show gamma density (light blue), CT density (dark blue), the lithologic log, the CT scan,
 1255 and PMS (red). Green tie lines show the correlations for the bases of these turbidites, as in Figure
 1256 8. We then group each geophysical property trace from each core. Each data set has the same
 1257 range of values for the horizontal axes (gamma density = 0–2.5 g/cm⁻³ **[[not cc]]**; CT density =
 1258 0–255 dn, grayscale digital number, scaled in these figures for viewing ability; and PMS = 0–150
 1259 SI × 10⁻⁵). These geophysical data maintain their original vertical scale. The lower panel shows

1260 how geophysical data are flattened to the bases and tops of the turbidites using one core at the
 1261 fixed 100% vertical scale (note that the tie lines are horizontal). We choose one core (labeled in
 1262 purple in Fig. 9) to hold at a fixed vertical scale and then scale (flatten) the data from other cores
 1263 to that core. We do this iteratively to test possible links or lack thereof between sites. Flattened
 1264 sequences should fail to show similarities between sites and or violate age constraints if
 1265 sequences are unrelated.

1266 **Basin-Basin Comparisons**

1267 Turbidite series T-3–T-5 is correlated between cores 105, 104, 103, and 96, based on the
 1268 stratigraphic sequence shared between these cores. T-3 and T-4 are multipulse turbidites with
 1269 fine and very fine sand that fines upward to medium to coarse silt. T-3 and T-4 are both preceded
 1270 by thinner multipulse coarse to medium silt turbidites, here noted as T-5. In core 105 **[[why no**
 1271 **suffixes for core designations (PC, etc.)?]]** these turbidites comprise ~3 main upward-fining
 1272 pulses; overall, the sequence coarsens upward (each superposed bed is coarser than its
 1273 underlying bed). While the other cores have lower turbiditic sedimentation rates, the geophysical
 1274 data show a concomitant upward trend in turbidite mass (coarsening upward), with a multipulse
 1275 geophysical property trend. Cores 104 and 103 have turbidites underlying T-3 that are slightly
 1276 different (upward fining in core 104; a low mass overall for core 103, resulting in an
 1277 indistinguishable geophysical fingerprint). The two ¹⁴C ages underlying T-3 have overlap in their
 1278 error ranges.

1279 With a similarly large regional extent, we correlate T-6 and T-8 between these same
 1280 cores 105, 104, 103, and 96 **[[why no suffixes for cores?]]** (Figs. 8 and 9B). The overlying
 1281 sequence of T-3–T-5 provide an upper boundary condition for these correlations. T-7 in these
 1282 cores forms a sequence of a thin muddy turbidite overlain by a thicker and coarser multipulse

1283 turbidite. T-8 is a fine sand to silt, multipulse turbidite with upward-fining beds. Overall, the
 1284 turbidite is upward coarsening in cores 96 and 103 (each superposed bed is coarser than its
 1285 underlying bed), and upward fining in cores 105, and 104. T-6 is fine sand to silt, multipulse,
 1286 upward-fining turbidite. In core 104, the base of T-7 is a sequence of ~32 coarse silt to very fine
 1287 sand, 1–3-mm-thick, upward-fining laminations. Also in core 104, this coarser turbidite head is
 1288 overlain by a tail that has 1–3 cm coarse silt laminations interbedded with ~6 very fine sand, 1–
 1289 3-mm-thick laminations. T-7 in other cores has a similar depth-density sequence, but in 96 and
 1290 104 it has a more expanded section, so the stratigraphic details are less observable in the other
 1291 cores. The ^{14}C ages in cores 96 and 104 [[no suffixes for cores?]] have overlap in their 95.4%
 1292 error ranges.

1293 Due to the poor preservation of turbidite structure and the fine texture of turbidites T-12–
 1294 T-17 in 96PC, these turbidites are here only correlated between cores 105, 104, and 103 (Figs. 8
 1295 and 9C). These cores span ~70 km and represent a region of at least 2100 km². This turbidite
 1296 sequence shows how stratigraphic order (superposition) plays a role in addition to the
 1297 geophysical property trend fingerprints. A key turbidite is T-18, a fine sand to silt, upward-fining
 1298 multipulse turbidite. We compare the sequence T-20–T-17 in regard to the sequential upward
 1299 change in relative trends of CT density and PMS data. For PMS, T-20 has relative intermediate
 1300 values, T-19 has lowest values, and T-18 has the largest values. The gamma density sequence
 1301 begins with the lowest values for T-20, intermediate values for T-19, and the largest values for
 1302 T-18. These sequential trends match across all three cores, though the variability in trends of the
 1303 geophysical data for each deposit reflects how these proxies for grain size are imperfect. T-21
 1304 has unique sequences that are shared between cores in slope cores (96, 103, 104, and 108[[core
 1305 suffixes?]]) and trench cores (105, 03, 05; Patton et al., 2013a). T-21 is a thicker multipulse,

1306 upward-fining, fine sand to silt turbidite (Figs. 8 and 10). BMS data show a large maxima
 1307 the base of this deposit, most remarkable in cores 105 and 104, although it is in 108 and 103 as
 1308 well. In cores 108 and 105, T-21 is 60 cm and 23 cm thick respectively, with a 20-cm-thick
 1309 sandy base in each core. Core 108 has several upward-fining pulses of laminated and massive
 1310 mud that are only ~3 cm thick in core 105. The 3^{14}C age estimates underlying T-21 in cores 108,
 1311 104, and 103 overlap in each of their error ranges.

1312 In addition to the well-correlated deposits, we also describe some of the less-well
 1313 correlated or uncorrelated deposits. Some of these turbidites are well correlated between some
 1314 cores, but not in others. Between 108 and 105, T-4, T-6, and T-11 are not well correlated
 1315 possibly due to the high bioturbation in core 108. There are fewer turbidites in 108 younger than
 1316 T-21, suggesting a change in either the site or the delivery mechanisms younger than T-21 time,
 1317 making it problematic to correlate individual beds to 108 during that time span.

1318 Core 96PC bottomed in T-18, and thus T-18 is partially contained in core 96PC (Fig. 8).
 1319 Core 96PC appears to have the muddy tail for the T-18 turbidite, but this is difficult
 1320 to test since the base of the T-18 deposit is absent. If the lowermost turbidite in core 96 is T-18, a
 1321 coarse sandy base of the turbidite, as found in other cores, is missing. Considering the thickness
 1322 of the tail of this turbidite and turbidites with similar tail thicknesses in other cores, the sandy
 1323 base may be on the order of tens of centimeters, and likely stopped the penetration of core 96.
 1324 Possibly supporting this hypothesis is the seismic reflection data, which shows
 1325 an acoustically opaque deposit below the depth of the core that appears to fade upward to a depth
 1326 overlapped by the core depth (dark brown vertical line in Fig. 6B). The spatial limit of the
 1327 seismic reflection profile is designated by a yellow line in Figure 6A.

1328 Basin-Trench Comparisons

1329 The first basin to trench comparison is between core 108 in a slope basin and core 107 in
1330 the trench 44 km distant. Core 108 **[[PC, TC needed for these?]]** is in a small basin that has a
1331 25-m-high sill to the north and a 200-m-high sill to the south (Figs. 3A, 3C). This basin probably
1332 partially drains to the north, given that turbidity current flow depths may be >100 m (Muck and
1333 Underwood, 1990; Völker et al., 2008). Core 107 is in the trench axis 45 km to the southwest of
1334 core 108. The stratigraphy in cores 108PC and 108TC correlates well, with no apparent missing
1335 sediment from core 108PC. The TC has ~45 cm of repeated stratigraphic section, which happens
1336 if the core penetrates the seafloor multiple times (which may occur when the ship is heaving
1337 sufficiently). We observe that core 107 has more turbidites than in core 108, between T-3 and T-
1338 21. Core 108 **[[PC, TC needed?]]** is bioturbated in this section, possibly confounding the
1339 geophysical property representation of those deposits, making it more difficult to uniquely
1340 correlate strata. T-14 in core 108 also has an indistinct geophysical property trend, although it
1341 fines upward in both cores. Based solely on the comparison of T-14 between the two cores,
1342 this is at best a poor correlation. The correlation of T-14 between cores 108 and 107 is supported
1343 by the correlation between cores 107 and 105. **[[PC, TC or other suffix needed?]]**
1344 Moving southward, we compare strata between two trench cores, 107 and 105, **[[suffix
1345 needed?]]** 40 km apart (Supplemental Files S1 and S3). Core 107 is located in the axis of the
1346 trench at 4520 m water depth. While collecting core 107, the core tripped prematurely at ~1134
1347 m water depth. This changed the depth configuration of the PC and the TC, leaving the PC at a
1348 lower position (the PC cored sediment before the TC). T-1 is present in 107PC, but not 107TC,
1349 the reverse of the normal situation where the TC is more likely to sample the uppermost
1350 sediment. Sediment in core 107PC is highly disturbed from coring, but is sufficiently preserved
1351 to tentatively correlate with 107TC. Core 105 is located on a ≥ 20 -km-wide terrace that is ~100 m

1352 above the depth of the trench axis at a depth of 4480 m, 11 km from the trench axis, which has a
 1353 depth of 4550 m. **[[suffix needed?]]** Core 105 is west of a gently sloping, 0.5-km-high landward-
 1354 verging anticline (Henstock et al., 2006; Graindorge et al., 2008; Sultan et al., 2009) that shields
 1355 this site from direct sedimentation from higher relief bathymetry to the east. 105TC sampled ~15
 1356 cm more sediment than 105PC, so core 105 is shown as a PC-TC composite core. T-1 is
 1357 apparently present in core 105TC. The uppermost ²¹⁰Pb sample has presence of activity beneath
 1358 this young deposit (Fig. 7). The gamma and CT density data for T-2 in cores 105TC and 107TC
 1359 match nicely. While T-3 in core 107TC has a low dynamic range in turbidite texture and
 1360 geophysical property trends, we correlate the sequence of T-4 and T-5 with higher confidence
 1361 (Figs. 8 and 9; Supplemental File S3); considering the sequence above T5, this supports our
 1362 correlations of T-2 and T-3. We correlate T-7, T-10, and T-11 from cores 107–105, with higher
 1363 confidence due to shared sequences of geophysical property trends and shared patterns of
 1364 turbidite structures. In core 107, turbidites underlying T-10, down to T-14, are disturbed due to
 1365 coring and are therefore more difficult to correlate. In core 107, the turbidites underlying T-14
 1366 are muddy and have low dynamic range in density, so do not have characteristic trends in
 1367 geophysical properties. We correlate the lower turbidites in core 107 with core 105 with low
 1368 confidence. Because there are no ¹⁴C ages in the trench cores, all correlations are designated with
 1369 dashed lines in Figures 8 and 9. **[[correct? if not, describe where the dashed lines are found]]**
 1370 Cores 105 and 104 are 40 km apart; **[[no core designations, i.e., 104PC, TC, etc.??]]** core
 1371 104 is located at 3480 m water depth near the base of an ~1.5-km-tall cliff, within and near the
 1372 edge of a slope basin that is being dissected by a submarine canyon from the southeast (Fig. 3).
 1373 Cores 104PC and 104TC contain very similar uppermost stratigraphy, including the coarse sandy
 1374 base of T-1 (core 104TC also includes two sections of repeated stratigraphic section). The



1375 turbidites in core 104 are more thinly laminated than those in 105, but the geophysical property
1376 trends match well for most of these correlated turbidites. Correlations of T-3–T-8 and T-17–T-20
1377 are presented here (Fig. 9). Laminae between T-20 and T-21 are closely spaced and difficult to
1378 interpret in core 104PC. We are not certain whether these are laminations in the upper part of T-
1379 21, or separate turbidites. T-21 provides a robust anchor point and boundary condition for the
1380 underlying correlations T-22–T-37. We correlate turbidites T-22–T-34 with lower confidence
1381 due to the closely spaced finely laminated turbidites in core 104. These finely laminated
1382 turbidites are difficult to distinguish from each other within core 104. [[suffix for cores?]]
1383 Cores 104 and 103, the next trench-slope core pair, are 34 km apart. Core 103, at a depth
1384 of 3070 m, is located near the center of a 2–4-km-wide flat-bottomed slope basin that slopes
1385 upward at $\sim 1^\circ$ to the east, with no resolvable channels (Fig. 3). The basin is enclosed by a 20 m
1386 sill on the northwestern boundary, which probably permits partial flows of sediment outside of
1387 this basin. When combined with 102MC, at the same site, we correlate turbidites between cores
1388 103–102 and core 104 with high confidence, ranging from T-1–T-11, T-15, and T-17–T-21. Core
1389 103 is missing T-1, but T-1 and T-2 are sampled in core 102MC (Supplemental File S3). The
1390 lowest ~ 50 cm of 103TC contains repeated stratigraphic section. Turbidites in core 103 are much
1391 thinner overall than in core 104 (e.g., the base of T-7 is at a depth of 32 cm in core 103 and at a
1392 depth of 119 cm in core 104). In cores 103 and 104, the sequence of T-8–T-9 shows an overall
1393 upward increase in PMS values, helping to uniquely identify these correlated turbidites. The
1394 sequence T-10–T-11 also has matching and superposed geophysical fingerprints in cores 103 and
1395 104, best viewed in the PMS data. The turbidites between T-12 and T-17 are too bioturbated in
1396 core 103, and thus have weak geophysical property trends; those correlations are shown with less
1397 confidence. The sequences of T-18–T-20 also have matching and superposed geophysical

1398 fingerprints in cores 103 and 104, especially noticeable in the PMS data. The sequence of T-18–
1399 T-20 in cores 103 and 104 **[[suffix needed?]]** also shares a common densostratigraphic series
1400 visible in the CT imagery and the CT density geophysical data. This T-18–T-20 sequence
1401 demonstrates the multiproxy correlation method, using not only the flattening of core
1402 geophysical data for individual turbidites, but the entire stratigraphic sequence as well. In
1403 addition to the T-18–T-20 sequence, T-21 has a higher mass than the overlying and underlying
1404 turbidites and in some examples a distinctive simple structure, providing an anchor for those
1405 other correlations. Cores 103 and 104 **[[suffix needed for cores?]]** have very distinct PMS and
1406 CT density trends for T-27, which provide support for this correlation. There are more turbidites
1407 that appear to correlate between cores 104 and 103 than observed in other cores, but we do not
1408 assign these turbidites T numbers due to their limited areal extent. Due to the closely spaced
1409 laminations and lack of hemipelagic sediment in core 104, there are few ^{14}C ages in the lower
1410 section. This makes it difficult to temporally constrain these correlations independently.

1411 We compare cores 103 and 95–97 **[[suffix needed for highlighted cores?]]** (Figs. 3 and
1412 8; Supplemental File S3). Cores 95 and 96–97 are located in two small ($\sim 50\text{ km}^2$) enclosed
1413 basins, within a larger slope basin that partially drains to the south over a 70-m-high sill at 2250
1414 m water depth (Fig. 6A). Core 95 contains strata that appear correlated with strata in core 96, but
1415 the sediments in core 95 are quite disturbed, so we leave that core out of the correlation figures
1416 and later discussion. The overlap in stratigraphy between 96PC and 96TC and 97MC was
1417 presented here (see results discussion). Based on the downcore trend in ^{210}Pb data, the $\sim 5\text{-cm-}$
1418 thick sediment underlying T-1 in core 96TC is likely from the seafloor, and therefore likely is
1419 repeated section, probably containing sediment from the surficial mixed layer. Based on this
1420 observation, it is possible that the base of T-1 is not in core 96TC. Turbidites in core 96 are

1421 generally thicker and less bioturbated than those in core 103. In addition to the high confidence
 1422 correlations presented earlier in Figure 9, the turbidites underlying T-11 in core 96PC are more
 1423 bioturbated, thinner, and finer in texture than most overlying turbidites, contributing to the lower
 1424 confidence in our correlations between cores 103 and 96. Because T-18 is not entirely within
 1425 core 96, this correlation is less certain and untestable.

1426 Trench cores 98 and 94 **[[should this be “Cores 98TC and 94TC”? See highlighted]]**
 1427 are the southernmost trench cores in the 2004 earthquake slip region (Fig. 7). Core 98 is west of
 1428 a gently sloping 0.5-km-high landward-verging anticline, possibly isolating this core from direct
 1429 sedimentation from higher relief bathymetry to the east. Core 94 is located off axis from the
 1430 trench and downslope of several potential landslide source areas in the form of submarine
 1431 canyons, base of slope apron fan channels, and local landslide amphitheater complexes (Patton et
 1432 al., 2013a). In the trench, cores 98PC and 98TC overlap completely and neither sampled the
 1433 sediment-water interface, evidenced by core 99MC, which has the uppermost turbidite we
 1434 interpret to be T-1 (Supplemental File S3). Most turbidites in core 98 **[[TC?]]** are muddy with
 1435 low dynamic range in particle density and size. This, coupled with the lack of ^{14}C ages, leads to
 1436 less confident correlations. At the southern limit of the 2004 earthquake slip region, core 94PC
 1437 sampled the uppermost turbidite that we interpret as T-1. Core 94 is highly deformed and lacks
 1438 ^{14}C age control, so these correlations are also less certain (Supplemental File S3). However, the
 1439 very young soupy surface turbidite, the lack of surface oxidation, and ^{210}Pb age data are
 1440 compatible with our interpretation that this is likely the 2004 turbidite.

1441 Farther south, in cores 93TC and 88TC, we make moderately confident correlations with
 1442 the turbidite underlying the uppermost turbidite in these cores. We correlate these second
 1443 turbidites in these two cores to T-1 found in the cores to the north (Supplemental File S3). The

1444 geophysical property trends are almost identical between these cores and are very similar to the
 1445 geophysical fingerprint of T-1 in core 96PC; therefore the uppermost turbidite in 93TC and
 1446 88TC is likely younger than the probable 2004 deposit We tentatively interpret the uppermost
 1447 turbidite in cores 93TC and 88TC to be the result of the 2005 M 8.7 earthquake (Hsu et al., 2006;
 1448 Briggs et al., 2006).

1449 Radiocarbon Age Results

1450 Here we present the results of our age model based calibrations for deposits older than T-
 1451 1 (raw calibrated ages are in Table 2). Bayesian modeling of radiocarbon calibrations takes into
 1452 account varying degrees of stratigraphic information as prior constraints for these calibrations.
 1453 We utilize P_Sequence age models for within-core age calibrations and present these results in
 1454 Figure 8 and Supplemental File S4⁴. We use Sequence age models for the region-wide
 1455 comparison of ages between cores, and summarize these age model results in Table 5. All ages
 1456 initially considered in our model are in Table 5A. Ages that we consider in our final age model
 1457 are in Table 5B, with selection criteria discussed here. We present the P_Sequence age model
 1458 results in Table 5C.

1459 Where multiple ¹⁴C ages exist for correlated turbidites, and where ages do not suggest
 1460 erosion or other problems, we test whether they are compatible with our stratigraphic correlation
 1461 model by using the Combine function in OxCal software (Bronk Ramsey, 2008). Combined [[no
 1462 quotes]] ages for turbidites T-3, T-4, T-5, T-7, T-10, T-11, T-21, and T-27, [[are T- prefixes
 1463 correct?]] are computed with the combination of 2-5 ages (Table 5B; Supplemental File S4).
 1464 OxCal takes the laboratory ages and calculates a pooled mean laboratory age prior to calibration.
 1465 The result is a probability density function age range, based on the contribution of all combined
 1466 ages. We evaluate the Combine results using three criteria: a chi-squared test, the OxCal



1467 agreement index A_{comb} **[[subscript, as elsewhere?]]** (>60), and convergence integral C (>95)
 1468 (Bronk Ramsey, 1995, 2009a, 2009b). The Combine function is normally used with the prior
 1469 information that the samples come from either the same sample, or from the same horizon
 1470 (Bronk Ramsey, 2008). Our lithostratigraphic correlations are the basis for interpreting these
 1471 groups as coming from the same horizon, though with far less certainty than if they were from
 1472 the same bed in an outcrop. We acknowledge that our combine results may impart a shorter time
 1473 range of uncertainty than realistic given our inability to quantify erosion, bioturbation, and other
 1474 departures from a uniform age sequence.

1475 We present the results of our criteria tests for Sequence age model and how we used these
 1476 criteria to test for and manually remove **[[no quotes]]** outlier ages from our age model (Bronk
 1477 Ramsey, 2009b). Of the results shown in Table 5, **[[A, B, or C?]]** there were no chi-squared or
 1478 agreement index failures for the P_Sequence age models (Bronk Ramsey, 2009b). Sequence
 1479 age model had two failures for the age combinations (Combine function; Table **[[A, B, or C?]]**).
 1480 The Combine for T-33 initially fails the chi-squared test at 5% and with A_{comb} **[[subscript?]]** =
 1481 56.6%. For the T-33 Combine, we manually removed SUM-050 from the Combine because the
 1482 Agreement Index A was lower at 44.0%, leaving a single age calibration for the T-33 age
 1483 estimate. The Combine for T-41 initially fails the chi-squared test at 5% and with A_{comb}
 1484 **[[subscript?]]** = 17.1%. For the T-41 Combine, we manually removed SUM-044 from the
 1485 Combine because the Agreement Index A was lower at 25.8%, leaving a single age calibration
 1486 for the T-41 age estimate.

1487 **Regional Stratigraphic Correlation Summary**

1488 In general, the more certain correlations temporally span 2.8 k.y. (T-1–T-21) in core 108,
 1489 ~2.8 k.y. in core 104 (T-1–T-21), ~2.8 k.y. in cores 102/103 (T-1–T-21), and 2 k.y. in core 96

1490 (T-1–T-11; Figs. 3–18). These more certain correlations include 6 turbidites in core 108, 1
 1491 turbidites in core 104, 17 turbidites in core 103, 11 turbidites in core 96, 1 turbidite in core 98, 1
 1492 turbidite in core 94, 1 turbidite in core 93, and 1 turbidite in core 88. When we include less
 1493 confident correlations, there are 28 turbidites in core 108, 21 in core 107, 39 in core 105, 37 in
 1494 core 104, 43 in core 103, and 18 in core 96. Based on the lowermost correlated turbidite in any
 1495 given core, we find that cores 108, 107, 105, 104, 103-102, and 96 contain 65%, 49%, 91%,
 1496 86%, 100%, and 42% of these correlated turbidites, respectively. **[[no core letter designations
 1497 in the preceding paragraph?]]**

1498 We have tested potential correlations between sites within the 2004 rupture zone
 1499 iteratively using the available age control, patterns of variability in the overall sequence of
 1500 turbidites, and detailed comparisons for intrasite and intersite similarity between individual
 1501 turbidites. We find that in some cases, individual turbidite characteristics are similar enough,
 1502 within and between sites, that they may be used to track individual turbidites in a sequence. The
 1503 stratigraphic sequences with the most unique fingerprints (Goldfinger et al., 2013a) carry the
 1504 strongest correlative weight and act as anchors for our correlations (Fig. 8), supported by ¹⁴C age
 1505 control. We designate turbidites with numbers corresponding to their order down from the
 1506 seafloor. Turbidites are assigned T-numbers that designate these deposits to be regionally
 1507 correlative, counting down from the uppermost turbidite (T-1). Turbidites that have sediment
 1508 with low dynamic range (e.g., fine-grained turbidites) and nonunique sedimentary structure
 1509 (possibly with nonunique geophysical properties) are more difficult to correlate with confidence.
 1510 Because we cannot correlate these turbidites, we do not include them in this discussion.

1511 DISCUSSION

1512 2004 Turbidite

1513 We found the uppermost turbidites in cores 01GC, 05PC, 26GC, 109MC, 108PC-108TC
1514 107PC, 105TC, 104PC-104TC, 102MC, 99MC, 97MC, 96PC-96TC, 95PC, 94PC, 93TC, 88TC,
1515 and 87PC-87TC to be composed of gray sediment with a very high water content (i.e., soupy),
1516 particularly at the seabed. These represent 21 discrete examples of the uppermost young bed, of
1517 54 cores and core attempts within the 2004 region. The 2 uppermost turbidites in cores 93 and 88
1518 also share this soupy characteristic. There is no hemipelagic sediment overlying these deposits,
1519 and we do not observe oxidation in the uppermost sediment in any of these cores. This deposit, if
1520 correlated, spans as much as 500 km and 230 km, in the trench and along the slopes,
1521 respectively, and is present in cores with unique and isolated sediment source areas (Figs. 3 and
1522 6; Supplemental Files S1 and S5³). Of the remaining 33 cores within the 2004 area, cores 107TC,
1523 105PC, 103PC-103TC, 93PC, and 88PC are missing their tops; cores 98PC-98TC are
1524 indeterminate; 03TC-03PC had bioturbated and oxidized tops with no young surface bed; 10GC,
1525 11GC, 12GC, and 13KC were 55 km west of the margin, likely well out of the turbidity current
1526 extent; 15GC and 16GC were on the top of the forearc plateau and taken for other purposes.
1527 Cores 106PC-106TC are very distal control cores ~170 km west of the margin; cores 19GC,
1528 20GC, and 21GC were all 22 km west of the margin, outside axial the axial trench channel
1529 system; cores 94TC, 02GC, 03GC, 04KC, 07MC, 08GC, 09GC, 14GC, and 17KC had no
1530 recovery for various reasons. The lack of the 2004 turbidite is well explained for most these
1531 cores. Only cores 18GC, 101GC, 100MC were in a seemingly suitable mid-slope basin, yet
1532 lacked a young surface turbidite. On closer inspection, however, these cores are located in a wide
1533 flat basin of the type we have found unsuitable for unchannelized turbidity current deposition
1534 (Patton et al., 2007; Goldfinger et al., 2014a; see Supplemental File S6⁶ for supporting core top
1535 data).

1536 Oxidation of sediment provides a qualitative assessment of relative age and oxidation of
 1537 the uppermost sediment is rapid in most settings. Turbidite tails typically have relatively high
 1538 organic content compared to hemipelagic and pelagic sediments (e.g., Cowie et al., 1998),
 1539 reducing the time constant for surface oxidation. In several studies, the response time for
 1540 oxidation of the upper sediments has been quantified. Hammond et al. (1996) modeled the
 1541 reactions responsible for O₂ and NO₃ profiles in the central equatorial Pacific. The uppermost
 1542 sediments were assumed to be mixed at rates described by ²³⁴Th and ²¹⁰Pb profiles. Hammond et
 1543 al. (1996) **[[correct “They”?]]** described a dominant and more labile fraction that oxidized in
 1544 days to months, and a less labile fraction that oxidized in decades. Sayles et al. (2001) also found
 1545 response time to be short at 0.3–1.6 yr for high flux sites, and 5–80 yr for very low flux sites in
 1546 the Southern Ocean. Smith (1987) found response times of 0.1–0.2 yr for high flux sites and 1–5
 1547 yr for low flux sites, in the eastern and central North Pacific between California and Hawaii.
 1548 While detailed data on oxidation rates do not exist for Sumatra, we infer from these studies that
 1549 oxidation would most likely be apparent if the uppermost turbidite were **older than** ~5 yr at the
 1550 time of collection, which was ~2.6 yr after the 2004 earthquake. Oxidation therefore may
 1551 constrain the timing of emplacement more tightly than other methods, and suggests an age for
 1552 the surface turbidite within a few years of collection.

1553 Using the available constraints, our P_Sequence ¹⁴C age model for **the** uppermost
 1554 turbidite in core 96PC suggests a median age of 60 ± 150 calibrated yr **B.P.** **[[correct, or**
 1555 **calendar (both used in text)? B.P. is before A.D. 1950?]]** (Table 3). **The** ²¹⁰Pb age data in cores
 1556 96 and 102 are compatible with an age within the past few decades at most, as are the
 1557 radiocarbon ages (Figs. 7 and 8). We therefore interpret this young turbidite as likely the result of

1558 the 2004 earthquake, with the evidence spanning a distance of ~230 km along strike, a region of
 1559 at least 10,500 km² (Fig. 3).

1560 **There was no detectable** ¹³⁷Cs in cores 94PC and 105TC due to at least one of two
 1561 possible reasons (Table 4): either there was insufficient ¹³⁷Cs in this region of the Indian Ocean
 1562 to detect given the gamma counting methods (Wheatcroft and Sommerfield, 2005) **because**
 1563 complete or nearly complete decay had occurred, or the sediment was deposited prior to 1952.
 1564 Based on measurements from seawater (Alam et al., 1996), there may have been ¹³⁷Cs in the
 1565 seawater. In this case, the ¹³⁷Cs may not have deposited in sufficient concentration at the
 1566 seafloor. If sedimentation rates are sufficiently low, and or there was sufficient erosion, we
 1567 would not expect to find ¹³⁷Cs activity in these cores.

1568 Site conditions play an important role in proximal sites such as those in this study. Of all
 1569 cores, core 96PC has the most expanded section of what we interpret to be the 2004
 1570 seismoturbidite. The expanded stratigraphic section is possibly due to the core site, found in the
 1571 center of a 40-km-long by 7-km-wide slope basin that probably does not drain completely,
 1572 possibly causing the sediment to pond (Fig. 6A). Underlying turbidites are also thicker than
 1573 interpreted correlatives in other cores, suggesting that the reason for thicker deposits is site
 1574 related. For example, T-6 and T-7 are 23 cm and 30 cm thick in core 96, **[[96PC?]]** but only 6
 1575 and 3 cm thick in 103PC. We use the entire sedimentary section above the oldest ¹⁴C age in each
 1576 core to calculate the overall sedimentation rate (Table 6). The overall sedimentation rate for the
 1577 past 2 k.y. in core **96PC** **[[96PC?]]** is 1.93 ± 0.09 mm/yr, 0.59 ± 0.03 mm/yr in core 103PC
 1578 **[[correct?]]** (minimum **because** the 2004 deposit is absent in this core), 1.04 ± 0.03 mm/yr in
 1579 core 104PC, and 0.46 ± 0.07 mm/yr in core 108PC **[[is PC correct?]]** (minimum because while
 1580 the base is present the uppermost portion of the possible 2004 deposit is absent). The

1581 stratigraphic section in 104PC has an overall sedimentation rate similar to that of 96PC, though
1582 the higher rate at the 104 core site (compared to cores 103PC and 108PC[[correct?]]) is possibly
1583 due to the position at the base of an oversteepened slope (Fig. 3D), although persistently stronger
1584 ground motions at this site are also a possibility. Because over the past 2 k.y. the hemipelagic
1585 rate varies little along strike (Table 2; Supplemental File S7), the primary source for variation in
1586 overall sedimentation rate is likely due to differences in turbidite deposit thicknesses.

1587 **Lithostratigraphic Correlation in the SASZ 2004 Region**

1588 The correlated framework shown in Figure 8 represents a depositional history of
1589 turbidites spanning ~6.5 k.y., with a potential for a longer record based on the seismic reflection
1590 results. Our lithostratigraphic correlations are based on correlation criteria, some qualitative
1591 (including stratigraphic superposition, geophysical proxy fingerprinting, visual lithostratigraphic
1592 descriptions) and some quantitative (relative and absolute ages). When more correlation criteria
1593 are satisfied for a given turbidite bed, the confidence in bed correlation increases, and the
1594 corresponding tie line is thicker and solid. Radiocarbon age results are plotted for the sediment
1595 underlying the correlated turbidites. The map (Fig. 3A) shows the core locations and the isolated
1596 source areas for the basin cores.

1597 A key tool to distinguish multipulse turbidites that were deposited as the result of a single
1598 earthquake from stacked turbidite beds (Nelson et al., 2012) that were deposited as the result of
1599 multiple earthquakes is the presence of hemipelagic sediment and perhaps an oxidized layer
1600 between turbidites. Because oxidized layers require more time to develop than the duration of
1601 ground shaking, these layers may provide evidence that the multiple turbidites represent multiple
1602 seismogenic events. An example of this is found between T-3 and T-4 in core 105. [[suffix for
1603 core?]] However, it may be possible that these oxidized layers may be absent between

1604 seismoturbidites. Here we refer to surface oxidation, not downward-propagating oxidation fronts
 1605 (e.g., Wilson et al., 1985), which are also found in our cores. A second line of evidence that can
 1606 distinguish between single single-pulse or single multipulse turbidites from multiple single-pulse
 1607 or multiple multipulse turbidites is that the particle size and geophysical parameter values return
 1608 to some background pelagic or hemipelagic value. An example of this is in core 96 where
 1609 density values in T-4 decrease upcore and reach a low value that corresponds to an oxidized
 1610 hemipelagic layer beneath T-3. There is a correlation between oxidized layers and low
 1611 geophysical parameter values for many of the hemipelagites in core 96. In core 103, T-3 and T-4
 1612 are muddier (lower sediment dynamic range) and lack oxidation laminae, so these deposits are
 1613 less confidently correlated. In core 104, T-3 has underlying oxidized laminae, but T-4 does not.
 1614 Considering these data as a whole, for turbidites T-1–T-4, core 96 contains the balance of the
 1615 correlated turbidites and other cores contain at least a subset of these turbidites. We note that
 1616 some turbidites are absent across some intervals in the 2004 rupture region. For example, T-2, T-
 1617 4, T-6–T-9, T-11–T-13, and T-15–T-20 may not present in core 108 (Fig. 8; Supplemental File
 1618 S3). Likewise, T-1 and T-2 appear to be absent in core 103 (missing top), but appear in core 102.
 1619 These omissions may be due to site conditions, erosion, ability to core the entire stratigraphic
 1620 section, or rupture characteristics (slip, directivity, duration and energy content of shaking;
 1621 Kramer and Lindwall, 2004). If this were due to the result of site physiography and source
 1622 proximity, cores that are more proximal than ideal in most cases would be expected to generate
 1623 greater variability, as has been observed in Cascadia (Goldfinger et al., 2008, 2012a). The
 1624 missing top in core 103 is probably the result of overpenetration or erosion of the seafloor while
 1625 coring, because core 102MC includes an uppermost turbidites that are missing in core 103. The
 1626 uppermost sediment can sometimes be eroded from the seafloor by the piston core during coring



1627 due to the high velocity of the corer compared to trigger **cores**, **multicores**, and Kasten cores. In
1628 this case, the uppermost sediment is missing from both the PC and the TC. Missing section in the
1629 trigger (gravity core) can sometimes occur through overpenetration and loss of material through
1630 the upper valve in the top of the corer. The missing section in **cores 108** and **103** **[[highlighted**
1631 **cores missing letters?]]** may be the result of differences in turbiditic sedimentation rate (e.g.,
1632 finer grained and/or thinner bedded turbidites), leading to increased bioturbation in the more
1633 finely grained and thin turbidites (Goldfinger et al., 2013b), making the turbidites more difficult
1634 to distinguish from background sedimentation. Tapered ground motions, as they diminish with
1635 distance from higher slip magnitudes, could also lead to finer grained turbidites. These missing
1636 sections may also be due to erosion of previous turbidites during the emplacement of any given
1637 overlying turbidite. Natural variability of this type is expected at proximal sites, and is observed
1638 in Cascadia (Adams, 1990; Goldfinger et al., 2012a) and elsewhere (Pouderoux et al., 2012). It is
1639 also possible, and even likely, that at any single core site we did not sample in the optimal
1640 location. Thus, **the** relatively limited time for survey for each site and the reconnaissance nature
1641 of our understanding of local slope processes may have resulted in potentially missing the best
1642 depositional area for a given basin or trench area.

1643 T-1-T-11, 15, and T-17-T-21 **are** well correlated and are best explained by seismic
1644 triggering. T-12-T-14, T-16, and T-22-T-43 are less well correlated, but are attributed to a
1645 seismogenic trigger due to their spatial extent and the **isolation** of their respective sediment
1646 source areas. Other thinner and less coarse **and/or** dense turbidites are even less well correlated.
1647 While some of these other turbidites may be explained by a seismogenic trigger, they are not
1648 included in our earthquake chronology because of the low confidence for these correlations.

1649 Nonetheless, some of these other turbidites may be from foreshocks or aftershocks, or from
1650 smaller earthquakes. In the following we discuss the site controls to deposition at our core sites.

1651 **Site Effects**

1652 We have presented a few of the key correlations within which the post ~6500 yr
1653 Holocene turbidite sequences are interpreted as a coherent framework. Refer to Figures 8 and 9
1654 for the following discussion of how correlated turbidites may differ between cores. There are
1655 many reasons that might contribute to these differences in structure between turbidites correlated
1656 between different cores. Highly bioturbated sediment may alter the geophysical property
1657 (changing the shape of the fingerprint) or structural interpretation of the turbidite. Highly
1658 deformed sediment and muddy turbidites may not be well correlated if the deposit has a low
1659 signal to noise ratio (low dynamic range in density or particle size) because their geophysical
1660 property fingerprints are not unique. In addition, there are muddy turbidites that may be the
1661 result of forcing factors other than earthquakes.

1662 Autocyclic forcing factors may dominate at one site more than another, where local
1663 hydrodynamics may influence sedimentary structure or densostratigraphy. For example, sites that
1664 are within channels are more likely to have a larger dynamic range (resulting in larger
1665 geophysical peaks) than sites that are on terraces or in overbank settings. Allocyclic forcing
1666 factors may be more or less dominant at different sites, where the variations in ground motion
1667 and slope stability at the sediment source area control the initial input of sediment to the turbidity
1668 current. Subduction zone earthquake ruptures generally have nonuniform slip, leading to
1669 variations in seismic moment release through space and time (Barrientos and Ward, 1990; Konca
1670 et al., 2007; Moreno et al., 2009, 2011). Ground motions at the seafloor likely relate to these
1671 variations in slip (Arias, 1970). The ground motions also attenuate in response to a series of

1672 factors, including distance to the slip and crustal or site characteristics (e.g., rheology of
 1673 underlying seascapes; Bilek et al., 2004; Bilek, 2007; Mahani and Atkinson, 2013). One core may
 1674 be closer to a larger slip region (higher energy release) for one earthquake, but at a greater
 1675 distance for a different earthquake. The differences in coarsening or fining upward in the T-3–T-
 1676 4 sequence may be due to either site effects, hydrodynamic pathway effects, or differences in
 1677 earthquake ground motion (Fig. 9A).

1678 We observe some sites at which the individual deposits and deposit sequences have
 1679 persistent and similar sedimentary structures unique to that site. For example, cores 104PC and
 1680 104TC record what we interpret to be regional turbidites T-1–T-32 by correlation to other sites.
 1681 In these cores individual turbidite beds are commonly expanded as a sequence of many thin
 1682 coarse pulses as part of their single turbidite structure. The core location for 104 **[[PC or TC?]]**
 1683 is at the base of a steep slope, with ~1.5 km of relief, and the canyon mouth outlet is <1 km to
 1684 the east of the site (Fig. 3D; Supplemental File S3). We suggest that local retrogressive failure
 1685 accompanying each seismic event, such as observed by Piper et al. (1999), may explain the
 1686 repeated thinly laminated structures in core 104 **[[PC or TC?]]**

1687 Another example is core 96, **[[not PC, TC, or other?]]** which has fine-grained turbidites
 1688 and higher overall sedimentation rate (turbidites are thicker; Table 6). Core 96 is located in a
 1689 closed slope basin fed by very low relief terrain that does not form large channels (Fig. 6A). The
 1690 low-relief terrain might explain the fine-grained texture, while the enclosed basin may be
 1691 responsible for the relatively overthickened (ponded?) turbidites. Core 103 is in a location that
 1692 has a low gradient, wide floodplain, and wide channel directly upslope, possibly explaining the
 1693 low dynamic range of turbidite texture (Fig. 5D). Core 103 is located at the western edge of a
 1694 small (~20 km²) basin with eastward-sloping seafloor.

1695 Our interpretation for proximity control on turbidite deposition is supported by looking at
1696 trench cores 98 and 94; [[not 98TC, 94TC?]] along with some slope cores 104 and 103. Core 98
1697 is located in the trench in a position protected from higher relief mass wasting processes sourced
1698 from the slope by a landward vergent anticline (Fig. 3F; Supplemental File S5). The turbidites
1699 are thin and less sandy than core 94, possibly as a result of this effect (Supplemental File S3). In
1700 contrast, core 94 is located near the mouths of multiple canyon systems, and generally has
1701 thicker and sandier turbidites (Fig. 3G; Supplemental File S5). One amphitheater-shaped
1702 landslide source area directly feeds the seafloor surrounding core 94 (arrow designates
1703 downslope direction in Fig. 3G). Proximal dominance is further supported by the stratigraphy in
1704 cores 103 and 104. While these cores are closely spaced (34 km apart; Fig. 3D) and correlate
1705 well with each other (Figs. 8–10), they have differences in turbidite style (thickness, structure)
1706 that probably reflect autocyclic forcing.

1707 **Stratigraphic Correlation Summary**

1708 The coherence of the turbidite fingerprints and radiocarbon ages between isolated basin
1709 and trench sites over 230 km along the strike of the subduction zone suggests that many or most
1710 of the correlated turbidites have a common trigger (Figs. 7–10). The good stratigraphic
1711 correlation between sites isolated from each other, from land sediment sources, and from other
1712 triggering mechanisms, coupled with consistent radiocarbon ages, suggests that the most likely
1713 triggering mechanism is regional subduction zone earthquakes. Uncorrelated turbidites present at
1714 some sites may be random sediment failures or smaller, local earthquakes. These uncorrelated
1715 turbidites commonly are thin and have low mass with nonunique fingerprints, making it more
1716 difficult to interpret their origin. We observe no examples of major turbidite beds that have no
1717 likely correlatives in other cores.

1718 **Age Relations**

1719 Radiocarbon ages provide a test of the temporal coherence of our correlations, but we
1720 also use them as a first-order control on the age of turbidites and recurrence of the earthquakes
1721 proposed as the origin for those turbidites (detailed radiocarbon methods are described in
1722 Supplemental File S2). Trench cores do not have radiometric age control, thus correlations
1723 between these and other cores do not have an independent test for our stratigraphic correlations.
1724 Therefore all of our correlations in the trench cores are tentative (Fig. 8; Supplemental File S3).
1725 One important source of aleatory uncertainty is basal erosion (Goldfinger et al., 2012a). Erosion
1726 preceding turbidite deposition would remove the youngest sediments underlying the turbidite,
1727 causing ^{14}C ages derived from those sediments to be older than the time of deposition. Erosion
1728 may be evaluated by collecting multiple cores at a given site (methods in Goldfinger et al.,
1729 2012a; Gutiérrez-Pastor et al., 2009). These erosion estimates are minimum estimates because
1730 there are no direct observations of the seafloor prior to the deposition of these turbidites, and
1731 erosion of all sites may be missed. Due to wire handling equipment failures, we were unable to
1732 collect multiple cores at each site, limiting our ability to evaluate erosion. Therefore our age
1733 models do not include assessment of basal erosion. The effect likely produces an overestimate of
1734 turbidite ages, as well as an increased scatter of ages among sites for turbidites even if they are
1735 synchronous.

1736 **There** does not appear to be a systematic explanation for the small number of outlier ages.
1737 The excluded ages only slightly overlap with ages from underlying turbidites and **there is** no
1738 overlap with the overlying turbidite. We removed one age **for** T-33 in core 108PC (Table 5A)
1739 because it is ~310 **yr** older than the corresponding age in **core** 103PC. We removed one age for
1740 **T-41** in core 108PC (Table 5A) because it is ~400 **yr** older than the corresponding age in **core**



1741 103PC. We do not have an explanation for the older ages for T-33 or T-41 in core 108,
 1742 **[[108PC?]]** but consider the correlation strong enough to reject the age on this basis. Because
 1743 age biases due to erosion and the detrital material being dated almost always drive ages older,
 1744 and rarely younger (Goldfinger et al., 2012a), it is common to have an age that is too old and
 1745 virtually impossible to have one that is too young; thus we choose to remove the older ages in
 1746 core 108PC from the combines for T-33 and T-41. This age sample also has the lower agreement
 1747 index A_{comb} .

1748 After outlier removal, the remaining ages satisfy the measures of agreement. The age
 1749 model is therefore compatible with our stratigraphic correlations within the uncertainties inherent
 1750 in radiocarbon, and the outlier removal seems reasonable. The external criteria on which the
 1751 lithostratigraphic correlations are based support the inference that these horizons, in this context,
 1752 most likely represent the same trigger event temporally. We therefore have combined them
 1753 statistically in Table 7 and Figures 3 and 8. The OxCal code and lo^{op} output of our radiocarbon
 1754 age model with both modeled and unmodeled ages listed in Table 5 **[[A, B, C?]]** are found in
 1755 Supplemental Files S2 and S4A.

1756 Lithostratigraphy, radiocarbon age and geophysical log correlation suggest a good
 1757 correlation of turbidites T-1–T-17 in core 96 and T-1–T-21 between cores 108, 105, 104, and
 1758 103. **[[any core labels?]]** These cores span the southernmost 2004 rupture zone and the
 1759 earthquake records found in these cores likely represent earthquakes with associated spatial
 1760 limits to earthquake ground motions (Figs. 8 and 11). The turbidites that are not correlated in
 1761 core 108 may represent earthquakes with more limited rupture length than the 2004 earthquake
 1762 (i.e., smaller earthquake magnitude). It may also be that this core contains these turbidites, but
 1763 the turbidites are too bioturbated or muddy to resolve (Goldfinger et al., 2013b). Less well



1764 correlated are turbidites T-22–T-39 in cores 108, 105, and 103, T-22–T-37 in core 104, and
1765 turbidites T-39–T-43 in cores 108 and 103. **[[core labels for these?]]** Some ages (e.g., T-33 for
1766 core 108 with core 103 and T-41 for core 108 and core 103) are incompatible with the preferred
1767 stratigraphic interpretations in Figure 8, but none of the ages overlap substantially with
1768 underlying turbidite ages (Figs. 8 and 11; Supplemental File S3). These small differences in age
1769 may be due to differences in basal erosion (more erosion means an older age), to minor
1770 differences in the marine reservoir (which are not yet resolvable), **miscorrelations**, or
1771 noncorrelation.

1772 **Origin of the Sumatra Turbidites**

1773 *Sumatra Specific Factors*

1774 Of the potential triggering mechanisms proposed (Adams, 1990; Goldfinger et al., 2003,
1775 2012a; Shanmugam, 2008), only a subset of these triggers applies to outer forearc sites offshore
1776 of Sumatra. **In** addition, several mechanisms do not directly trigger slope failure, but simply
1777 precondition slopes for failure (e.g., sediment loading, tectonics oversteepening, and regional gas
1778 hydrate destabilization). The remaining mechanisms are hyperpycnal flows, wave loading, bolide
1779 impact, self-failures, and earthquakes (intraplate and interplate). Frequent gas hydrate
1780 destabilization events linked to local as opposed to regional temperature changes would likely
1781 not occur synchronously **and therefore** could not be responsible for triggering frequent submarine
1782 landslides across large areas, as found in our cores. Crustal earthquakes and structural
1783 oversteepening and self-failures would leave behind highly localized deposits because their
1784 impact is localized. Bolide impacts may also leave a regional turbidite record, but their
1785 recurrence, on the order of thousands of years, is far too long to explain the chronostratigraphy in
1786 our cores (Rampino and Stothers, 1984; Rampino, 1984, 1999, 2002; Ward, 2002; Chesley and

1787 Ward, 2006). The remaining processes that can be both regional and synchronous include
1788 hyperpycnal flows, wave loads (storm and tsunami), and earthquakes (discussed in the
1789 following).


1790 *Hyperpycnal flow.* Very large storms could potentially generate hyperpycnal flows,
1791 leaving behind hyperpycnites as the result of fluvial delivery of sediment to the coastal margin or
1792 through the resuspension of sediment along the continental shelf. In the region of the 2004 SASZ
1793 earthquake, core sites are located near landslide source areas that have no direct connection with
1794 continental shelf or fluvial sedimentary systems because the 50–70-km-wide unfilled Aceh Basin
1795 isolates the outer prism from this terrigenous input. The forearc plateau rises an average of 2.2
1796 km above the forearc basin floor, effectively trapping all terrigenous input in the basin to the
1797 east. The Sumatra forearc plateau has a number of islands that could provide terrigenous input to
1798 sites downslope in the outer forearc. The nearest island, Simeulue, is 130 km to the southeast of
1799 our nearest slope core site, and there is no sedimentary pathway linking Simeulue to any of the
1800 core sites discussed here. We also note that hyperpycnites are reported to initially coarsen
1801 upward and then fine upward, representing the waxing and then waning of the hyperpycnal flow
1802 (Mulder et al., 2003; St-Onge et al., 2004). Turbidites in our cores do not show evidence of this
1803 depositional sequence, consistent with the observations of the spatial isolation of landslide
1804 source areas that feed our core sites.

1805 *Wave Loading.* Wave loads can potentially trigger submarine landslides in two ways: (1)
1806 cyclic changes in pore pressure causing liquefaction induced slope failure and (2) shear failure of
1807 sediment on the slope, canyons, or shelf. These wave loads can be induced from storm waves or
1808 from tsunami waves.

1809 Significant wave height, H_s , and spectral mean and peak wave period, T_m and T_p , have
1810 been modeled with buoy data and measured using satellite altimetry (Young, 1999; Alves and
1811 Young, 2003; Izaguirre et al., 2011) for the northeastern Indian Ocean in the region of our
1812 paleoseismic survey. Buoy data models estimate H_s with a 100 yr return period to be 3.5–9.5 m
1813 (Caires and Sterl, 2005). Alves and Young (2003) used satellite altimetry measurements to
1814 estimate H_s with a 100 yr return period to be 6–10 m. Izaguirre et al. (2011) used satellite
1815 altimetry measurements from 1992 to 2010 to estimate H_s with a 20 yr return period at 5–7 m.
1816 Young (1999) calculated T_m and T_p using the spectral wave model WAM (Komen et al., 1994)
1817 and find T_m to range from 10 to 13 s and T_p to range from 6 to 8 s in the region of our
1818 paleoseismic investigation. Measurements collected for these estimates are short lived and may
1819 not fully capture the variability, potentially missing extreme events possibly occurring in the past
1820 6500 yr. Notwithstanding this possible limitation, we adopt these values as characteristic for the
1821 northeast Indian Ocean.

1822 Cheng et al. (2001) suggested that passing waves, whether storm or tsunami, induce pore
1823 pressure loads that increase with each successive wave. If the sediment properties result in
1824 undrained conditions, the increased pore pressure may induce liquefaction and induce slope
1825 failure. Based on models of cyclic loading and drainage tests, where pore space decreases and
1826 shear strength increases, the sediment can result in being more resistant to slope failure
1827 (Miyamoto et al., 2004). This cyclic loading, whether from passage of storm or tsunami waves, is
1828 likely to retard slope failure. Chang et al. (2004) modeled this resistance to liquefaction in
1829 saturated sandy nearshore settings offshore Taiwan. The maximum depth that liquefaction was
1830 induced was 15 m, much shallower than the source areas in this study. Storm wave heights
1831 ranged from 1.5 to 7 m and wave periods ranged from 5 to 12 s, both consistent with H_s and T_m

1832 and Ts for offshore Sumatra. We therefore conclude that wave loading at depths of 1500–5000 m
 1833 in the source areas for our turbidite cores is unlikely. We note that the lack of cyclones in
 1834 equatorial waters (Peduzzi et al., 2012) all but rules out massive regional storms as a sediment
 1835 source via either hyperpycnal flows or wave loading. Were such cyclones present in the past,
 1836 they would still fail to trigger turbidity currents on the forearc slope with the majority of
 1837 minimum depths relevant to this study of ~1500 m.

1838 Tsunami-triggered turbidity currents have been examined in several locales. A tsunami-
 1839 generated turbidite on the Tohoku shelf was reported (Ikehara et al., 2014), clearly identified by
 1840 ²³⁴Cs, sourced from the Fukushima nuclear accident, that fades with depth on the upper slope and
 1841 is not present in deep water (K. Ikehara personal commun., 2012; Ikehara et al., 2012  **[[personal**
 1842 **communications from a coauthor are not listed (only if to Ikehara from a different person);**
 1843 **this should be listed as “personal data” or other]]**). In Goldfinger et al. (2012) the sediment
 1844 transport potential for storm and tsunami waves in Cascadia was calculated, and it was
 1845 concluded that neither wave type could shear or transport sand at depths >~450 m.

1846 A turbidity current triggered by a tsunami has been proposed for as the origin of a
 1847 homogenite in the Mediterranean Sea (Kastens and Cita, 1981) sourced in water depths of 100–
 1848 2000 m. However, Kastens and Cita (1981) required a wave height of 1.9–17 m linked to a
 1849 volcanic collapse. The maximum amplitude of the 2004 tsunami based on ground deformation on
 1850 Simeulue Island and modeling the wave as imaged, in the deep sea, by the TOPEX/Poseidon
 1851 **joint satellite mission** and Jason altimetry (Wang and Liu, 2006) is 1.5–2 m, considerably
 1852 smaller. The water depths in the source areas for our basin sites are generally greater (1500–5000
 1853 m) than the proposed source areas of the Mediterranean homogenite (Mediterranean Ridge and
 1854 African shelves). In addition, sediments offshore of Sumatra are cyclically strengthened, as

1855 discussed herein, unlike the Mediterranean Ridge hemipelagites, making them less susceptible to
 1856 this type of induced failure.

1857 Weiss (2008) calculated the capability of the 2004 SASZ subduction zone tsunami to
 1858 move fine sand to a maximum depth of 985 m in the Bay of Bengal and 335 m in the region of
 1859 our paleoseismic investigation, and concluded that tsunamis of similar size or smaller than the
 1860 2004 tsunami would be unlikely to initiate motion on seafloor sediments with low cohesion (fine
 1861 sand). Potential source areas for slope cores in this study range from 1.5 to 5 km, all deeper than
 1862 the Weiss (2008) maximum modeled depth. Core 108 has a small region of
 1863 potential source area that reaches depths as shallow as ~750 m, but because the cores that have
 1864 correlatable deposits have deeper potential source areas, the potential for tsunami wave loading
 1865 as a trigger for the landslides that resulted in the turbidites in our cores is very limited.

1866 **Comparisons to Onshore Paleoseismology**

1867 We directly compare our results with records of earthquakes in the form of sandy
 1868 deposits interpreted to be paleotsunami deposits, records of uplifted abrasion platforms, and
 1869 records of coseismic paleodeformation recorded by coral microatolls. Our turbidite-based
 1870 evidence suggests that the 7 earthquakes prior to 2004 were ca. 390 ± 260 , 630 ± 110 , 740 ± 120 ,
 1871 820 ± 130 , 940 ± 180 , 1080 ± 140 , and 1220 ± 220 cal ^{14}C yr B.P.; these ages do not overlap
 1872 with any turbidite ages. [if ages are not ^{14}C dates, please use “yr ago”; “these ages”
 1873 correct?] These two northern Simeulue uplift events have smaller magnitudes of uplift and may
 1874 be the result of smaller subduction zone earthquakes, crustal earthquakes, or slow earthquakes
 1875 that would not coincide with ground motion-triggered submarine slides. There is a temporal gap
 1876 (462–20 cal yr B.P., i.e., A.D. 1488–1930) in the Meltzner et al. (2012) microatoll record during
 1877 which we do not observe any correlated turbidites. Meltzner et al. (2010, 2012) speculated about


1878 possible missing earthquakes that may have occurred between their penultimate earthquake and
1879 the 2004 earthquake, although we suggest that large earthquakes in this period are unlikely due
1880 to the absence of turbidites. Thresholds for recording earthquakes with coral microatolls are
1881 likely different than those for recording earthquakes in sedimentary deposits, making event
1882 comparisons problematic at this stage of development in the Sumatra margin paleoseismic
1883 record.

1884 We note that the timing of the paleoearthquake record of the Siberut and Enggano
1885 segments (Kopp et al., 2008; Sieh et al., 2008; Philibosian et al., 2012, 2014) and the Meltzner et
1886 al. (2012) record overlap in age range with the penultimate (T-2) and antepenultimate (T-3)
1887 turbidite ages from this study. However these uplift event ages from the Siberut and Enggano
1888 segments do not overlap with uplift event ages from Simeulue (Sieh et al., 2008; Meltzner et al.,
1889 2010, 2012; Philibosian et al., 2012). The overlap with turbidite ages is therefore due to the
1890 larger uncertainties for the turbidite ages, since the coral ages do not overlap. While long
1891 earthquake sequences such as the 2004–2010 sequence along Sumatra may have occurred in the
1892 past (Sieh et al., 2008), they are not necessarily the rule over the 6500 yr span in the turbidite
1893 record.



1894 Although these comparisons are somewhat coarse, the offshore evidence is broadly
1895 compatible with the onshore paleoseismic events. Paleotsunami, microatoll, and uplifted reefs
1896 may not record all earthquakes and thus may also represent maximum intervals for recurrence of
1897 great earthquakes sensitive to the recording thresholds of the different methods.

1898 **Temporal Pattern**

1899 We calculate mean recurrence intervals (RI) based on turbidite ages within single cores
1900 and based on turbidite ages from all cores using three methods (Tables 8 and 9). First we

1901 calculate the RI by dividing the age of the oldest turbidite in each core by the regional number of
 1902 correlated deposit intervals for that core (Table 9). We also determine the RI by determining the
 1903 mean downcore interseismic interval in each core (Tables 8 and 9). We perform these
 1904 calculations for each core and then find the mean for all cores for the purpose of intersite
 1905 comparison (Table 9), then consider how the turbidite class, along strike length of correlation,
 1906 and turbidite thickness standards might affect our RI estimates (Table 9). We also make
 1907 comparisons between our RI estimates with those of the terrestrial record, for comparable time
 1908 periods. 

1909 Based upon the oldest well-correlated seismoturbidite in cores 108, 104, 103, and 96,
 1910 **[[no core suffixes?]]** the mean RI for earthquakes large enough to generate a correlatable
 1911 geologic record in the region of the 2004 earthquake is 160, 140, 160, and 140 yr for those cores,
 1912 respectively (Table 9). The mean of these similar RI estimates is 150 yr.

1913 We consider the along-strike extent of turbidites, how well they meet turbidite 
 1914 classification criteria, and turbidite thickness, as criteria for separating potential large-magnitude
 1915 subduction zone earthquake deposits from other sources. Correlation between any of these
 1916 essentially requires an earthquake origin; however, turbidites that fail to meet these criteria
 1917 cannot be distinguished by their source from the four possibilities, crustal earthquakes, slab
 1918 earthquakes, small subduction zone earthquakes, or large subduction zone earthquakes. We
 1919 choose 150 km as the minimum strike length over which beds should be correlatable to satisfy
 1920 the length requirement, with >200 km used as a higher level of certainty. Strike length is limited
 1921 in the 2004 rupture area, because no data are available north of the border with India. We also
 1922 consider the number of beds along strike that are class 1 versus class 2 and class 3 beds **[[should** 
 1923 **identify what and/or whose classification scheme for these classes]]** as a measure of the

1924 robustness of the turbidite criteria, and also consider regionally consistent bed thickness as a
 1925 measure of levels of ground shaking. While approximate, such relative measures have proved
 1926 effective in Cascadia for both correlation and for linking the beds to the magnitudes of the source
 1927 earthquakes (Goldfinger et al., 2012a, 2013[[2013a or 2013b?]]; Rong et al., 2014). Beds that
 1928 meet all of these criteria are stronger candidates for having been generated by regional
 1929 subduction earthquakes (Supplemental File S8⁸). Using these three relative criteria, we use the
 1930 correlated turbidites to calculate three RIs (Table 9): (1) turbidites that correlate along strike for
 1931 >200 km, have the majority of turbidites from all cores that meet the majority of turbidite
 1932 classification criteria (class 1 turbidites), and have thicker turbidites in the majority of all cores;
 1933 (2) turbidites that meet the turbidite class and thicker standards, but only correlate for >150 km;
 1934 (3) turbidites that are correlated sufficiently to establish a seismogenic trigger based upon
 1935 meeting our stratigraphic correlation criteria (i.e., turbidites with T-numbers).

1936 Based on the range of standards met for discrimination between potential seismogenic
 1937 sources, using the age to T-43 of ~6520 yr, we calculate an RI for the entire series of 2200 yr for
 1938 turbidites that meet standard 1, RI of 550 yr for turbidites that meet standard 2 or higher, and RI
 1939 of 160 yr for the entire series of 43 correlated deposits in the 2004 region. [[What are standards
 1940 1 and 2? Should define here where first mentioned]] We discuss the RIs calculated for shorter
 1941 time periods in the following (see overall comparison in Table 9).

1942 If we then restrict the time ranges to make comparisons with other paleoseismic data, our
 1943 RI estimates are compatible with other RI estimates. We first compare recurrences of
 1944 earthquakes as recorded by regional paleotsunami deposits. RI estimates based on paleotsunami
 1945 records are regional in nature, and likely to be generated by large earthquakes, although the
 1946 knowledge of the spatial limits of ruptures that generated them is unknown (Dawson, 1999). We



1947 assume that the larger and regional subduction zone earthquakes are more likely to generate
 1948 tsunamis that might be preserved in the geologic record than are tsunamis generated by smaller
 1949 magnitude and more local earthquakes (Abe, 1979; Dawson and Stewart, 2007). These larger and
 1950 regional earthquake-generated tsunamis are reasonable to compare with the seismoturbidite
 1951 record because of a similar relation between trigger distance and earthquake magnitude for
 1952 seismoturbidites (Black, 2014). Based on these limitations, we do not consider historic
 1953 earthquakes in the Andaman Nicobar region that are $<M$ 8.0 (A.D. 1679, 1847, 1881, 1941) for
 1954 our RI estimate comparisons.

1955 We combine these paleotsunami records in two ways: (1) using the records as completely
 1956 unique (each paleotsunami represents a unique earthquake), and (2) using the records as
 1957 reasonably correlatable (paleotsunami records with mostly overlapping age uncertainty are
 1958 interpreted to be the result of the same earthquake; Supplemental File S8). For the first tsunami
 1959 RI estimate, considering records for the past ~ 1500 yr we find evidence for 10 earthquakes,
 1960 including the 2004 SASZ earthquake (Fig. 11; yr before present): 1470 ± 70 (A.D. 480;
 1961 Rajendran et al., 2006[[Rajendran et al., 2006 is not in the reference list.]]), 1210 ± 90 (A.D.
 1962 740; Fujino et al., 2009), 1080 ± 60 (A.D. 930; Nair et al., 2010), 1020 ± 110 (A.D. 930;
 1963 Monecke et al., 2008), 860 ± 70 (A.D. 1090; Rajendran et al., 2006), 600 ± 60 (A.D. 1350;
 1964 Monecke et al., 2008), 580 ± 50 (A.D. 1370; Jankaew et al., 2008), 370 ± 100 (A.D. 1580;
 1965 Fujino et al., 2010[[Fujino et al., 2010 is not in the reference list.]]), and 140 ± 150 (A.D.
 1966 1810; Malik et al., 2011). In the same time period, there are 10 seismoturbidites offshore of
 1967 northern Sumatra, including the 2004 SASZ earthquake seismoturbidite, with the age of the
 1968 oldest turbidite (T-10) for this span of 1500 ± 110 (Fig. 11; yr before present). The paleotsunami
 1969 RI estimate is $(1470)/(10 - 1) = 160$ yr. We consider it possible and perhaps likely that the pair

1970 of paleotsunamis of age 1080 ± 60 and 1020 ± 110 (yr before present), and the pair dated $600 \pm$
1971 60 and 580 ± 50 (yr before present) represent the same 2 earthquakes. If so, there would only be
1972 8 earthquakes in this time range, yielding an RI estimate of $(1470)/(8 - 1) = 210$ yr. The lower
1973 paleotsunami RI of 160 yr is identical to the seismoturbidite value of ~ 170 yr ($1500/10 - 1 =$
1974 167) for all correlated beds for the same period, and similar to the 210 yr RI for case where
1975 tsunamis that have closely overlapping radiocarbon ages are considered the same event. Of the
1976 10 seismoturbidites in this time range, all but T-9 have potential tsunami correlatives with
1977 significant overlap of radiocarbon ages. When we consider the more restrictive turbidite
1978 correlation standards for the same time period there are three seismoturbidites that meet standard
1979 1 and five seismoturbidites that meet standard 2 or higher. It appears, however, that the more
1980 restrictive standard yields a poorer fit to the paleotsunami record (Table 9). Our attempt to
1981 discriminate between the four earthquake sources, three of which are much less likely to generate
1982 regional tsunami, appears more likely to show that all the correlated turbidites in this time range
1983 were sourced from significant subduction earthquakes capable of generating regional tsunami.

1984 Microatoll records on Simeulue Island provide a unique record of paleodeformation that
1985 can also be compared to the seismoturbidite record. On northern Simeulue, for the past ~ 1100 yr
1986 (A.D. $2004 - 956 = 1048$ yr), Meltzner et al. (2012) reported 4 earthquakes with larger inferred
1987 fault slip and as many as 6 earthquakes if we include records of paleodeformation with smaller
1988 inferred fault slip; we find that these two scenarios constrain RI estimates of ~ 350 and ~ 210 yr,
1989 respectively. The turbidite record, at 180 yr (6 events), compares reasonably well to the record
1990 for all events on northern Simeulue of 220 yr, and is identical to the tsunami interval of 180 yr
1991 for the same time period (6 events).

1992 When we consider the turbidite correlation standards for the same time period, there is 1
 1993 seismoturbidite that meets standard 1, 3 seismoturbidites that meet standard 2 or higher, and 7
 1994 turbidites total, 3 of which only meet standard 3. The RIs for these three standards are 1080, 540,
 1995 and 180 yr, respectively. The seismoturbidites of standard 2 or higher (3 earthquakes) match the
 1996 Simeulue record in number and the total number of turbidites (7) is similar to the Simeulue
 1997 record (6); however, the individual age overlaps are poor. Only T-1 and T-6 have good age
 1998 matches. Four Simeulue events closely spaced in time between the mean ages of T-2 and T-3
 1999 overlap both those turbidite ages at the 95.4% uncertainty level (Fig. 11). Other turbidites appear
 2000 not to have good matches with the microatoll record. Given that our RI estimates and those of
 2001 Meltzner et al. (2012) describe earthquakes that generate observable records, these estimates are
 2002 maximum recurrence intervals representing an unknown completeness of record in both cases.
 2003 The reasons for a relatively poor fit to the microatoll data are unclear. The turbidite record for the
 2004 2004 rupture area covers ~270 km of strike length between the persistent (Meltzner et al., 2012)
 2005 Simeulue segment boundary and the Indian border, while the tsunami record includes the entire
 2006 Indian Ocean basin. We speculate that both the tsunami and turbidite records are more spatially
 2007 extensive, and may be less subject to any spatial bias related to long-term slip heterogeneity (or
 2008 lack thereof) or site location relative to past slip patches that might exist for what is essentially a
 2009 single site at the north end of Simeulue Island.

2010 To estimate a longer term RI, we extend our RI calculations to two longer time periods,
 2011 the temporal limit of core 96PC and the temporal limit for all of the correlated turbidites. 
 2012 Correlations that satisfy the correlation standard 1 must extend between cores 108 and 96, **[[no**
 2013 **suffix for cores?]]**  so the correlations limited by core 96 provide the longest time span for the
 2014 standard 1 RI. This RI has a more confident attribution to large subduction zone earthquakes.

2015 There are 4 seismoturbidites that satisfy standard 1, 6 seismoturbidites for standard 2, and 18
2016 seismoturbidites in total for this time period; this results in calculated RIs of 770, 460, and 140
2017 yr, respectively (Table 9). The correlations between cores 108 and 103 [[incomplete core
2018 designations?]] provide the longest time period with which to base a RI, though this is limited to
2019 a standard 2 correlation. For this RI, we cannot rule out seismogenic triggers from crustal, slab,
2020 or smaller subduction zone earthquakes. There are 4 seismoturbidites that satisfy standard 1, 13
2021 seismoturbidites for standard 2, and 43 seismoturbidites in total for this time period; this results
2022 in calculated RIs of 2200, 550, and 160 yr, respectively (Table 9).

2023 While we have more confidence in the more restrictive RI values, these restrictions are
2024 somewhat arbitrary, and belie the good fit of most turbidity current events to the onshore tsunami
2025 record for the ~1500 yr of record where multiple onshore sites are available (although we cannot
2026 rule out coincidence for this). The strike-length measurement is severely limited by the lack of
2027 data north of the Indian border, limiting the potential for along-strike correlation and therefore
2028 limiting the value of this measure. The beds emplaced during the ~1500 yr period of overlap
2029 with the tsunami record are not systematically higher or lower in quality of their characteristics
2030 or in their degree of preservation than those of earlier times; therefore we must consider the
2031 shorter recurrence interval of ~170 yr to be the preferred value from this study.

2032 Intersite Comparison

2033 We use the downcore series of recurrence intervals to make intersite comparisons.
2034 Downcore RI estimates are plotted as a function of age and correlated turbidite number in Figure
2035 12. Time is in calendar years and error bars are plotted using one standard deviation RMS. These
2036 RI estimates are calculated by dividing the time between correlated turbidites by the number of
2037 correlated turbidites that are represented by that time span. We find that all cores share similar

2038 downcore recurrence trends, supporting a common trigger mechanism, because such similarity
 2039 would not be expected for other random turbidite generating processes. Similar intersite
 2040 matching trends were found in downcore RI estimates for Cascadia subduction zone earthquakes
 2041 (Goldfinger et al., 2003, Fig. 4 therein).

2042 Longer RI times are represented by maxima in these plots centered approximately at 700
 2043 and 6500 yr. The shorter average RI between 1000–3000 yr ago **[[ok?]]** and the longer RI span
 2044 maxima centered at 0.7 and 6.5 ka are more robust examples of time length varying RIs because
 2045 these estimates have more direct ages and thus a more continuous record of correlated turbidites
 2046 in multiple cores. The RI maxima at 6.5 ka has fewer correlated turbidites in core 103 than in
 2047 core 104. The RI trends between cores 96, 103, and 104, for T-3–T-9 are similar **[[core**
 2048 **suffixes?]]** However, the maxima centered at 0.7 ka is much longer for core 96 than for the other
 2049 cores. Small variations in absolute RI length between cores may be due to age uncertainties or to
 2050 earthquake strike length variations. These downcore variations in RI may also represent
 2051 aperiodicity in subduction zone earthquakes, termed supercycles (Sieh et al., 2008; Goldfinger et
 2052 al., 2013a).

2053 **Extent of the 2004 and 2005 Turbidites and the Paleoseismic Record in Segment**

2054 **Boundaries**

2055 We note that the southernmost evidence for the 2004 turbidite is observed in core 95 in a
 2056 slope basin and core 88 in the trench (Figs. 7 and 13). Slope cores provide a better constraint to
 2057 the spatial limitations of ground shaking because their sedimentary sources and sinks are
 2058 spatially restricted. Trench cores are less reliable for this purpose because turbidity currents can
 2059 travel downtrench some unknown distance (trench mixing; Black, 2014). The slope cores nearest
 2060 to the 2004 earthquake that likely lack a 2004 deposit are 92PC-92TC and 91MC. Core 91MC



2061 has a sedimentary section not sampled in core 92, **[[core suffixes for highlighted cores?]]** an
 2062 uppermost turbidite that is highly bioturbated **with presence of** **[[meaning “and contains**
 2063 **forams” or “displays evidence of forams”?]]** forams. This supports our interpretation that this
 2064 core, at a range of ~100 km from the southern termination of 2004 slip, lacks a 2004 deposit. We
 2065 do not have radiometric age estimates for this deposit in core 91MC. In the trench, turbidites in
 2066 cores 93 and 88 have geophysical and structural similarities to the uppermost turbidite in core 96.
 2067 Because of these similarities, we correlate, in cores 93 and 88, the second turbidite from the top
 2068 with T-1 in core 96. There is a younger turbidite in cores 93 and 88 that we suggest may have
 2069 been deposited as a result of the March 2005 earthquake (Supplemental File S3). **[[core**
 2070 **suffixes?]]**

2071 There are few examples of rupture termination as observed in turbidite paleoseismic
 2072 records with enough core data to constrain them. One such example was recently published for
 2073 the Sumatra margin. Sumner et al. (2013) collected several cores ~50 km south of the rupture
 2074 zone (based on slip model of Chlieh et al., 2007) of the 2004 Sumatra M_w 9.2 earthquake (cores
 2075 labeled in yellow: 1PC, 2MC, 3PC, 4MC, 5MC, and 6PC; Fig. 13). Sumner et al. (2013) used
 2076 SO-002 core data to state that not all large earthquakes generate turbidity currents, despite using
 2077 nonideal sites and not having actually sampled the 2004 zone (Goldfinger et al., 2014**[[2014a or**
 2078 **2014b]]**). The 2004 earthquake generated a widespread turbidity current and left widespread
 2079 deposits in most of our sites (Figs. 3, 5, 7, 8, and 11). We use the SO-002 and RR0705 cores
 2080 instead as part of a sensitivity test for triggering distance along strike. The value of this test is
 2081 limited by the spatial extent of the two data sets, but suggests that in this case, distances of 50–
 2082 100 km from the 1 m slip contour along strike could be too great for reliable recording of
 2083 seismoturbidites on this part of the Sumatra margin. In addition to the limitations of spatially

2084 relevant SO-002 core sites, some were located in flat-floored, low-bathymetric-relief, wide
 2085 basins that have proven to be of limited use for paleoseismology in slope settings (Goldfinger et
 2086 al., 2014a, 2014b). We suggest that this is likely due to insufficient topography for local failures
 2087 or due to the lack of channelized turbidity flow paths. Other SO-002 cores were located >30 km
 2088 from their local canyon sources and >20 km from subdued local slopes. The slope failures
 2089 leading to these SO-002 core sites are not channelized and thus the turbidity currents rapidly
 2090 weaken as they spread across the basins (Nelson et al., 1986; Johnson et al., 2005; Patton et al.,
 2091 2013a; Goldfinger et al., 2014a, 2014b). Core 2MC of Sumner et al. (2013) includes a surficial
 2092 turbidite likely to be the 2004 turbidite based on its thickness and geophysical signature. Sumner
 2093 et al. (2013, Fig. 2B therein) agreed with our interpretation that SO-002–02MC includes a 2004
 2094 or 2005 deposit. This core is located in the trench (where there is possible sediment transport
 2095 from the north) and is close to the limit of slip for the 2004 earthquake than are any RR0705
 2096 slope cores, including core 96. **[[core suffix?]]**

2097 Given these limitations, a maximum triggering distance of ~50–100 km for the 2004
 2098 earthquake is supported by the data, subject to site sensitivities (Black, 2014). The 2004
 2099 earthquake had northward directivity, away from the core sites (Ammon et al., 2005; Ishii et al.,
 2100 2005; Chlieh et al., 2007), possibly affecting this value locally. Because of the distance and
 2101 rupture directivity, the SO-002 slope core sites were not ideal to record a turbidite from the 2004
 2102 earthquake, especially in slope basins. In addition, the main slip patch at the southern end of the
 2103 rupture (i.e., Chlieh et al., 2007) was considerably north of the core sites (>200 km), thus likely
 2104 strongly tapering ground motions southward toward the segment boundary. Ground motions in
 2105 the 2011 Tohoku-Oki earthquake at both north and south ends of the rupture diminished along
 2106 strike by an order of magnitude, from ~1 g **[[g = acceleration of gravity? Define here?]]** to

2107 ~0.1 g, over a distance of ~100 km (Goto et al., 2012). Across-strike (along dip) energy radiation
 2108 is broader because the energy is largely directed across strike in thrust earthquakes. This is a
 2109 result of the orientation of the slip vector of the earthquake, which is typically normal to the
 2110 trench. Ground shaking >0.5 g across strike extended across the forearc and well onshore, over a
 2111 distance of 300 km, for the Tohoku-Oki earthquake (Goto et al., 2012). Records of ground
 2112 shaking for the Tohoku-Oki earthquake exceeded 1 g, though these large values are thought to
 2113 have been influenced by site conditions that may have amplified the ground shaking (Zhao et al.,
 2114 2012[[Zhao et al., 2012 is not in the reference list. Zhao and Xu here instead?]]). We
 2115 therefore conclude that, while triggering distances are greater across strike, they are commonly
 2116 more limited along strike (Black, 2014). As to the general question of how commonly do great
 2117 earthquakes generate turbidity currents, we are not aware of any example of a submarine
 2118 earthquake of M_w 8.3 or greater that did not generate turbidity currents where this has been tested
 2119 (purposely or otherwise; see Black, 2014).

2120 We also observe that the turbidite record becomes less robust in the region of the segment
 2121 boundary of the 2004–2005 earthquakes, as well as the 2005 region. Segment boundaries
 2122 typically are characterized by low or no slip during earthquakes and commonly have complex
 2123 structural and slip transfer mechanisms from one segment to another (Barrientos and Ward,
 2124 1990; Bürgmann et al., 2005; Konca et al., 2005[[Konca et al., 2005 is not in the reference
 2125 list.]]; Chlieh et al., 2007, 2008; Schurr et al., 2007; Hok et al., 2011; Kiser et al., 2011[[Kiser et
 2126 al., 2011 is not in the reference list. Kiser and Ishii here instead?]]; Hayes et al., 2013). They
 2127 may also have many small earthquakes occurring between large earthquakes, leading to a
 2128 confusing and likely incomplete record (e.g., historic earthquakes offshore Sumatra; Fig. 13).
 2129 Briggs et al. (2006), Chlieh et al. (2008), and Meltzner et al. (2010, 2012) show the 2004

2130 earthquake slip along the 2004–2005 boundary diminishing to near zero at the boundary, under
 2131 central Simeulue Island. We find the turbidite record in the 2004–2005 segment boundary region
 2132 (including our cores and those of Sumner et al., 2013), considered in the regional context
 2133 presented here, consistent with the presence of a persistent segment boundary; this is also
 2134 suggested by histories of land-level change deduced from coral microatolls across the boundary
 2135 (Meltzner et al., 2012).

2136 Compared to the 2004 earthquake (Ammon et al., 2005), the 2005 rupture was much
 2137 smaller (M_w 8.7), and located much further downdip on the plate boundary. Slip in the outer
 2138 forearc was not coseismic, but occurred over a span of several months (Hsu et al., 2006). For our
 2139 core sites (and those of Sumner et al., 2013) focused in the outer wedge, the distance to the areas
 2140 of greatest ground motion was much larger than in 2004, decreasing the likelihood of generating
 2141 a viable turbidite record for that and other similar earthquakes. The turbidites we infer to have
 2142 been emplaced as a result of the 2005 earthquake are much thinner (~2–3 cm thick in cores
 2143 88PC, 93PC, and 90MC; Supplemental File S3) than the turbidites emplaced following the 2004
 2144 earthquake (as much as ~3 m thick in core 96; Supplemental File S3).


2145 Further analysis of the turbidites in the 2004–2005 rupture areas may address whether the
 2146 2004–2005 stress triggering relations are persistent features along the Sumatra margin
 2147 (McCloskey et al., 2005; Meltzner et al.,
 2148 2012, 2013; Kopp et al., 2008; Kopp, 2013).
 2149 There are also significant differences in the incoming plate that may lead to variation in
 2150 magnitude and recurrence of subduction zone earthquakes (Dean et al., 2008;
 2151 Franke et al., 2008; Kopp, 2013). Offshore of Sumatra, the subductability of the oceanic lithosphere may be

2153 controlled by its thickness, buoyancy, and frictional variation generated by the ca. 36.5 Ma
2154 extinct slow spreading Wharton ridge (Jacob et al., 2014). These factors possibly explain the
2155 indentor (deviation of the curvilinear subduction zone fault) in the subduction zone fault from
2156 ~6°S to ~3°N (Jacob et al., 2014) as well as fault slip magnitude, recurrence, and the extent of
2157 updip and downdip and along-strike variations in seismic and aseismic slip (Bilek et al., 2011).

2158 **Paleoseismograms**

2159 Submarine landslides can be triggered when seismic waves propagate through the
2160 landslide source area. If the source time function (Tanioka and Ruff, 1997; Bilek et al., 2004;
2161 Bilek, 2007) of the slope failures drives the sediment flux into the landslide system, and
2162 allocyclic forcing dominates (Underwood, 2005[[Underwood et al. here instead?]]; Dennielou
2163 et al., 2006), the longitudinal structure of the resultant turbidity current will have maxima
2164 associated with the peaks in seismic energy. Therefore, the vertical structure of the turbidite is
2165 expected to have coarse pulses of sediment corresponding to each pulse (maxima) in seismic
2166 energy. The general structure would have a coarse-grained base and fine upward, with multiple
2167 coarse subunits for each peak in seismic energy; particle size might scale with seismic energy.

2168 We note that the 2004 turbidite has three major fining-upward coarse pulses and several
2169 minor coarse pulses, for a total of six subunits in the turbidite base. The 2004 SASZ earthquake
2170 has three primary slip subevents (Lay et al., 2005). The relation between the earthquake source
2171 time function and the corresponding deposit originally led to the suggestion that the deposit
2172 structure can be used as a paleoseismogram [[no quotes]] (Seilacher, 1969; Goldfinger and
2173 Morey, 2004; Goldfinger et al., 2007, 2012b). Seilacher (1969) suggested that sedimentary
2174 structures could develop as the result of seismic loads to existing sedimentary deposits, while in
2175 Goldfinger and Morey (2004) and Goldfinger et al. (2007, 2012b) it was suggested that the

2176 sediments deposited following the earthquake record the earthquake source mechanism in the
2177 deposit. The source time functions produced by others (Ishii et al., 2005, Chlieh et al., 2007;
2178 Stein and Okal, 2007; Tolstoy and Bohnenstiehl, 2006)  plotted in comparison to the
2179 uppermost turbidite in core 96PC (Supplemental File S9⁹). There is good agreement between
2180 these plots of seismic energy release and the vertical sedimentary structure leading us to our
2181 comparison (Patton et al., 2013a, Fig. 6 therein). This interpretation is supported by results from
2182 laboratory experiments that related sediment flux with changes in sequential deposition of
2183 sediments with varying density (Garrett et al., 2011; Goldfinger et al., 2012a). We speculate that
2184 this uppermost turbidite offshore Sumatra probably satisfies the definition of paleoseismogram
2185 (Goldfinger and Morey, 2004; Goldfinger et al., 2007, 2012b). Our model predicts that these
2186 subevents may be recorded as discernible coarse pulses within the turbidite that can be correlated
2187 over large distances (Figs. 9 and 10). A similar conclusion was drawn for Cascadia earthquake
2188 turbidites (Goldfinger et al., 2012a); the mechanism has been tested in flume studies, and is
2189 predicted by theory and analog models (Goldfinger et al., 2012b, and references therein; Garrett
2190 et al., 2011).

2191 CONCLUSIONS

2192 We used multibeam bathymetry and seismic reflection data to develop an understanding
2193 of catchment basins, turbidity current pathways, and depositional styles, as well as to precisely
2194 locate our gravity cores, piston cores, Kasten cores, and multicores along the outer Sumatran
2195 forearc. The physiography of the forearc high and basin isolates these sites from terrestrial
2196 sediment input from Himalayan-derived sediment, and from large storms, providing good
2197 localities to investigate the potential for turbidite paleoseismology. We collected 144 sediment
2198 cores in the trench and in lower slope piggyback basins of the Sumatra accretionary prism. Our

2199 analysis of these cores used detailed physical property data, including computed tomographic X-
2200 ray (CT), gamma density, magnetic susceptibility, grain-size analysis, faunal analysis, and smear
2201 slides to evaluate the turbidite stratigraphy and sedimentology at each site. We use radiocarbon
2202 age control for piggyback basin sites above the CCD, and use ^{210}Pb and ^{137}Cs to evaluate the
2203 timing of the most recent sedimentary deposits. Using well-log correlation methods and the
2204 radiometric age control, we tested for potential correlations between isolated sites in piggyback
2205 basins and the trench. Turbidite stratigraphy is ubiquitous in isolated outer slope basin and trench
2206 sites along the northern Sumatra margin.

2207 The youngest turbidite (21 examples) in the region of the 2004 rupture has no overlying
2208 hemipelagic sediment, no oxidation at the seafloor, and has ^{210}Pb and radiocarbon ages that
2209 overlap a zero age of emplacement. This bed was most likely emplaced within a few years of
2210 2007. We interpret this turbidite as linked to the 26 December 2004 great SASZ $M_w \sim 9.2$
2211 earthquake. This earthquake triggered turbidity currents in multiple submarine drainage systems
2212 that left stratigraphic evidence in the form of multipulse turbidites in isolated slope basin and
2213 trench depocenters.

2214 Lithostratigraphic correlation and radiocarbon ages support serial deposition of turbidites
2215 over the past ~6500 yr in outer slope basin and trench sites. While local depositional variability
2216 in slope basins is relatively high, the aggregate of core data in and near the 2004 rupture zone
2217 form a consistent stratigraphic sequence among basin and trench core sites. Local variability is
2218 observed (and expected) for various reasons, including basal erosion, heterogeneous source areas
2219 within the region, coring deformation, nonseismic events, and varying site geomorphology.
2220 Intersite correlation is strong enough that we consider most of these beds to be to have been

2221 deposited synchronously. This conclusion is supported, but cannot be proven, with consistent
2222 radiocarbon age control.

2223 The fact that these Sumatra cores, in sedimentologically isolated and hydrodynamically
2224 unique systems, share similar turbidite sequences, suggests that they also share a common trigger
2225 mechanism. Random occurrences such as local self-failure, gas hydrate destabilization, and
2226 tectonic oversteepening would not be expected to correlate among sites, develop self-similar
2227 sequences in numerous isolated basins, or have any resemblance in their temporal history.
2228 Because triggering by large storm effects (hyperpycnal flow, wave loading) and triggering by
2229 passage of tsunami waves are excluded by both water depth and physiography, earthquakes are
2230 the best explanation for regional and synchronously triggered turbidity currents. While individual
2231 deposits cannot be unequivocally linked to earthquakes, alternative mechanisms would need to
2232 affect the different regions with similar frequency and result in landslides with similar turbidite
2233 structures, in the same stratigraphic order, to explain the sediment stratigraphy found in these
2234 cores.

2235 Among slab, crustal, and subduction zone earthquakes, discrimination of these types is
2236 not straightforward. Regional correlation within the 2004 rupture zone is limited to ~270 km by
2237 the lack of data along the Indian margin. Nevertheless, for the best period of overlap comprising
2238 the last ~1500 yr, the turbidite sequence comprises 10 events, and regional evidence for
2239 significant tsunami most likely includes 8 discrete events, all of which have significant overlap
2240 in radiocarbon ages with the offshore turbidites. Comparison of the turbidite stratigraphy with
2241 earthquake records in the form of uplifted coral microatolls reveals only two to three likely
2242 temporal matches over ~1100 yr. The reasons for this difference are not clear, but may be the

2243 result of spatial aliasing of the spatially limited coral records versus the more spatially extensive
2244 tsunami and turbidite records.

2245 Previous great earthquakes in the 2004 rupture region have shaken sufficiently to trigger
2246 at least 43 turbidity currents and to deposit corresponding turbidites during the past ~6.5 k.y.,
2247 yielding an average repeat time of 160 yr. For the period of overlap with the tsunami record, the
2248 recurrence average for 8 discrete events is similar to the turbidite record at ~210 yr and 170 yr,
2249 and given the individual event overlaps in time, we prefer this recurrence interval as the best
2250 representation of significant subduction zone earthquakes in the region. Crustal, slab, and small
2251 plate boundary earthquakes may be present in the record as well, but are considered less likely
2252 sources due to the strong correspondence with the regional tsunami record.


2253 The structure of the 2004 turbidite, with numerous replicates, comprises three main
2254 fining-upward subevents. The 2004 earthquake also comprises three main subevents both
2255 temporally and along strike (Supplemental File S9). This correspondence may support a recent
2256 hypothesis that the temporal pattern of seismic energy during the mainshock may impart a
2257 longitudinal structure to the resulting turbidity currents and thus be reflected in the deposits
2258 (Goldfinger et al., 2008, 2012a). The success of turbidite correlation in Cascadia, the northern
2259 San Andreas, and Sumatra suggests that some primary structure of the turbidity current maintains
2260 integrity, at least in the case of long-source great earthquakes, despite the fluid dynamic
2261 complexity of turbidity currents. We speculate that the longitudinal heterogeneity of the turbidity
2262 current, allocyclic forcing imparted by the heterogeneous earthquake rupture (the source time
2263 function of the earthquake), may be recorded in the deposits (Goldfinger and Morey, 2004;
2264 Goldfinger et al., 2008, 2011 [**Goldfinger et al. 2011 is not in the reference list. Change to**

2265 “Goldfinger et al., 2008; Goldfinger, 2011”?]], 2012a; Garrett et al., 2011). There may be
2266 potential to correlate the seismogenic forcing of these landslides with future work.

2267 We find that selecting core sites is essential when attempting to evaluate the sedimentary
2268 record of past earthquakes. Based on the presence of a turbidite we interpret to be the result of
2269 the 2004 SASZ earthquake in the RR0705 and SO-002 cores, and a global sensitivity analysis,
2270 we find a maximum along-strike triggering distance for the southern limit of the 2004 earthquake
2271 to be ~50–100 km. The best coring sites will conjoin as many positive factors as possible: these
2272 are factors that promote seismogenic triggering of turbidity currents and promote the deposition
2273 and preservation of their turbidites. Ideal paleoseismic locales would (1) comprise core sites
2274 nearest maximum shaking intensity; (1) have high-relief sources upslope; (1) be associated with
2275 turbidity current channels and canyons; and (1) comprise sites that may promote expanded
2276 stratigraphic section (such as those within enclosed basins). Poor localities include broad flat
2277 basins without channel systems, low-relief and distant topographic source areas, and persistent
2278 segment boundaries or other areas of reduced ground motion.

2279 ACKNOWLEDGMENTS

2280 This research was funded by the Ocean Sciences and Earth Sciences Divisions of the
2281 National Science Foundation (awards OCE 0526655, OCE 1030381). We are grateful for the
2282 comprehensive and constructive comments from Aron Meltzner and an anonymous reviewer.
2283 We thank the Indonesian Agencies BPPT (Badan Pengkajian dan Penerapan Teknologi) and
2284 LIPI (Lembaga Ilmu Pengetahuan Indonesia), collaborator Haryadi Permana, and the staff of
2285 the U.S. Embassy in Jakarta, without whom this work would not have been possible. We
2286 thank the Indonesian science party members Sapta Chahyadi, Eddy Hartantyo, Gatot Fajar
2287 Suryono, Yudo Haryadi, Riza Rahardiawan, Nanang, and Prabowo, and international science

2288 party members Alexis Vizcaino, Elena Pinero, Oriol Pique, Zoraida Rosello, Ximena
2289 Moreno, Russel Wynn, Eugene Morgan, Stefan Ladage, for their hard work at sea. We thank
2290 M. Erhardt, Amy M. Garrett, and Robert H. Porter for conducting laboratory analyses; NOC
2291 (National Oceanography Centre, Southampton), IFREMER (Institut Français de Recherche
2292 pour l'Exploitation de la Mer), and BGR for providing key bathymetry and subbottom data;
2293 collaborator Eulalia Gracia and UTM-CSIC (Unitat de Tecnologia Marina–Consejo Superior
2294 de Investigaciones Científicas) Barcelona, for supporting participation of the large Spanish
2295 contingent; NOC for supporting participation of Russ Wynn; BGR for supporting
2296 participation of Stefan Ladage; and AIST-GSJ (National Institute of Advanced Industrial
2297 Science and Technology–Geological Survey of Japan) for supporting participation of Ken
2298 Ikehara. We also thank coring technicians from Oregon State University (OSU) including
2299 Chris Moser, Bob Wilson, Kurt Schultz, and Paul Walczak, and UTM coring technicians
2300 Ramon Amettler and Roberto Gonzalez. We thank Scripps resident technicians; R/V *Roger*
2301 *Revelle* Captain Tom Djardins and crew; student volunteers and faculty from OSU, including
2302 Bart DeBaere, Javier Monc  and Maureen Davies. We also thank Rob Wheatcroft (OSU)
2303 and Guillaume St-Onge **[[St-Onge , not St. Onge (as in text and references; if not, should**
2304 **change all other spellings herein)]]** (Institut des Sciences de la Mer de Rimouski) for
2305 assistance with ^{210}Pb and ^{137}Cs analyses; Jerry Thompson of Rainstory Productions for
2306 supporting videographer Chris Aikenhead; and Morgan Erhardt, Amy M. Garrett, Jeff
2307 Beeson, Handoko Wendobo, and Bran Black for identifying and collecting foraminifera tests.
2308 Further details regarding the cruise and the core locations are provided in this cruise report:
2309 <http://www.activetectonics.coas.oregonstate.edu/sumatra/report/index.html>.

2310 REFERENCES CITED

- 2311 Abdeldayem, A.L., Ikehara, K., and Yamazaki, T., 2004, Flow path of the 1993 Hokkaido-
2312 Nansei-Oki earthquake seismoturbidite, southern margin of the Japan Sea north basin,
2313 inferred from anisotropy of magnetic susceptibility: *Geophysical Journal International*,
2314 v. 157, p. 15–24, doi:10.1111/j.1365-246X.2004.02210.x.
- 2315 Abe, K., 1979, Size of great earthquakes of 1837–1974 inferred from tsunami data: *Journal of*
2316 *Geophysical Research*, v. 84, p. 1561–1568, doi:10.1029/JB084iB04p01561.
- 2317 Abercrombie, R.E., Antolik, M., and Ekstrom, G., 2003, The June 2000 Mw 7.9 earthquakes
2318 south of Sumatra: Deformation in the India-Australia plate: *Journal of Geophysical*
2319 *Research*, v. 108, no. B1, 2003, doi:10.1029/2001JB000674.
- 2320 Adams, J., 1984, Active deformation of the Pacific Northwest continental margin: *Tectonics*,
2321 v. 3, p. 449–472, doi:10.1029/TC003i004p00449.
- 2322 Adams, J., 1990, Paleoseismicity of the Cascadia subduction zone: Evidence from turbidites off
2323 the Oregon-Washington Margin: *Tectonics*, v. 9, p. 569–583,
2324 doi:10.1029/TC009i004p00569.
- 2325 Alam, M.N., Chowdhury, M.I., Kamal, M., Ghose, S., Nahmood, N., Matim, N.A.K.A., and
2326 Saikat, S.Q., 1996, Radioactivity of ¹³⁴Cs, ¹³⁷Cs and ⁴⁰K in sea-water of the Bay of Bengal:
2327  *Applied Radiation and Isotopes*, v. 47, p. 33–35, doi:10.1016/0969-8043(95)00245-6.
- 2328 **[[Not cited? See query in text.]]** Almagor, G., and Wiseman, G., 1991, Analysis of submarine
2329 slumping in the continental slope off the southern coast of Israel: *Marine Geotechnology*,
2330 v. 10, p. 303–342, doi:10.1080/10641199109379898.
- 2331 Alves, J.H.G.M., and Young, I.R., 2003, On estimating extreme wave heights using combined
2332 GeoSat, Topex/Poseidon and ERS-1 altimeter data: *Applied Ocean Research*, v. 25, p. 167–
2333 186, doi:10.1016/j.apor.2004.01.002.

- 2334 Ammon, C.J., **et al.**, 2005, Rupture process of the 2004 Sumatra-Andaman earthquake: *Science*,
2335 v. 308, p. 1133–1139, doi:10.1126/science.1112260.
- 2336 Amy, L.A., and Talling, P.J., 2006, Anatomy of turbidites and linked debrites based on long
2337 distance (120 × 30 km) bed correlation, Marnoso Arenacea Formation, Northern Apennines,
2338 Italy: *Sedimentology*, v. 53, p. 161–212, doi:10.1111/j.1365-3091.2005.00756.x.
- 2339 Amy, L.A., Talling, P.J., Peakall, J., Wynn, R.B., and Thynne, R.G.A., 2005, Bed geometry used
2340 to test recognition criteria of turbidites and (sandy) debrites: *Sedimentary Geology*, v. 179,
2341 p. 163–174, doi:10.1016/j.sedgeo.2005.04.007.
- 2342 Arias, A., 1970, A measure of earthquake intensity, *in* Hansen, F.J., ed., *Seismic design for*
2343 *nuclear power plants*: Cambridge, Massachusetts Institute of Technology Press, p. 438–483.
- 2344 Atkinson, G.M., **and** Boore, D.M., 2003, Empirical ground-motion relations for subduction-zone
2345 earthquakes and their application to Cascadia and other regions: *Seismological Society of*
2346 *America Bulletin*, v. 93, p. 1703–1729.
- 2347 Atkinson, G.M., **and** Boore, D.M., 2011, Modifications to existing ground-motion prediction
2348 equations in light of new data: *Seismological Society of America Bulletin*, v. 101, p. 1121–
2349 1135.
- 2350 Atwater, B.F., 1987, Evidence for great Holocene earthquakes along the outer coast of
2351 Washington State: *Science*, v. 236, p. 942–944, doi:10.1126/science.236.4804.942.
- 2352 Atwater, B.F., and Hemphill-Haley, E., 1997, Recurrence intervals for great earthquakes of the
2353 past 3500 years at northeastern Willapa Bay, Washington: U.S. Geological Survey
2354 Professional Paper 1576, 108 p.
- 2355 Atwater, B.F., and Griggs, G.B., 2012, Deep-sea turbidites as guides to Holocene earthquake
2356 history at the Cascadia Subduction Zone—Alternative views for a seismic-hazard workshop:


- 2357 U.S. Geological Survey Open-File Report 2012-1043, 58 p.,
2358 <http://pubs.usgs.gov/of/2012/1043/>.
- 2359 Atwater, B.F., Carson, B., Griggs, G.B., Johnson, H.P., and Salmi, M.S., 2014, Rethinking
2360 turbidite paleoseismology along the Cascadia subduction zone: *Geology*, v. 42, p. 827–830,
2361 doi:10.1130/G35902.1.
- 2362 Baas, J.H., Van Kesteren, W., and Postma, G., 2004, Deposits of depletive high-density turbidity
2363 currents: A flume analogue of bed geometry, structure and texture: *Sedimentology*, v. 51, p.
2364 1053–1088, doi:10.1111/j.1365-3091.2004.00660.x.
- 2365 Baas, J.H., McCaffrey, W.D., Haughton, P.D.W., and Choux, C., 2005, Coupling between
2366 suspended sediment distribution and turbulence structure in a laboratory turbidity current:
2367 *Journal of Geophysical Research*, v. 110, C11015, doi:10.1029/2004JC002668.
- 2368 Bacon, C.R., 1983, Eruptive history of Mount Mazama and Crater Lake caldera, Cascade Range,
2369 U.S.A.: *Journal of Volcanology and Geothermal Research*, v. 18, p. 57–115,
2370 doi:10.1016/0377-0273(83)90004-5.
- 2371 Bacon, C.R., and Lanphere, M.A., 2006, Eruptive history and geochronology of Mount Mazama
2372 and the Crater Lake region, Oregon: *Geological Society of America Bulletin*, v.
2373 118, p. 1331–1359, doi:10.1130/B25906.1.
- 2374 Bandopadhyay, A., and Bandyopadhyay, R.R., 1999, Thermogenic hydrocarbons in the mid-
2375 proximal Bengal Fan, west of the Andaman-Nicobar Islands: *Marine Georesources and*
2376 *Geotechnology*, v. 17, p. 1–16, doi:10.1080/106411999273963.
- 2377 Barnard, W.D., 1973. Late Cenozoic sedimentation on the Washington continental slope [Ph.D.
2378 thesis]: Seattle, University of Washington, 255 p.

- 2379 Barnes, P.M., Bostock, H.C., Neil, H.L., Strachan, L.J., and Gosling, M., 2013, A 2300-year
2380 paleoearthquake record of the Southern Alpine fault and Fiordland subduction zone, New
2381 Zealand, based on stacked turbidites: *Seismological Society of America Bulletin*, v. 103, p.
2382 2424–2446, doi:10.1785/0120120314.
- 2383 Barrientos, D.E., and Ward, S.N., 1990, The 1960 Chile earthquake; inversion for slip
2384 distribution from surface deformation: *Geophysical Journal International*, v. 103, p. 589–
2385 598, doi:10.1111/j.1365-246X.1990.tb05673.x.
- 2386 Bayes, M., and Price, M., 1763, An essay towards solving a problem in the doctrine of chances,
2387 by the Late Rev. Mr. Bayes, F. R. S. communicated by Mr. Price, in a letter to John Canton,
2388 A. M. F. R. S: *Royal Society of London Philosophical Transactions*, v. 53, p. 370–418,
2389 doi:10.1098/rstl.1763.0053.
- 2390 Beeson, J.W., and Goldfinger, C., 2013, Large erosional features on the Cascadia accretionary
2391 wedge imaged with new high-resolution multibeam bathymetry and seismic datasets:
2392 *American Geophysical Union, fall meeting*, abs. S21C–2419.
- 2393 Béjar-Pizarro, M., Socquet, A., Armijo, R., Carrizo, D., Genrich, J., and Simons, M., 2013,
2394 Andean structural control on interseismic coupling in the North Chile subduction zone:
2395 *Nature Geoscience*, v. 6, p. 462–467, doi:10.1038/ngeo1802.
- 2396 Bilek, S.L., 2007, Using earthquake source durations along the Sumatra–Andaman subduction
2397 system to examine fault-zone variations: *Seismological Society of America Bulletin*, v. 97,
2398 p. S62–S70, doi:10.1785/0120050622.
- 2399 Bilek, S.L., Lay, T., and Ruff, L.J., 2004, Radiated seismic energy and earthquake source
2400 duration variations from teleseismic source time functions for shallow subduction zone

- 2401 thrust earthquakes: *Journal of Geophysical Research*, v. 109, B09308,
2402 doi:10.1029/2004JB003039.
- 2403 Bilek, S.L., Engdahl, E.R., DeShon, H.R., and El Hariri, M., 2011, The 25 October 2010
2404 Sumatra tsunami earthquake: Slip in a slow patch: *Geophysical Research Letters*, v. 38,
2405 L14306, doi:10.1029/2011GL047864.
- 2406 Bilham, R., 2005, Partial and complete rupture of the Indo-Andaman plate boundary 1847–2004:
2407 *Seismological Research Letters*, v. 76, p. 299–311, doi:10.1785/gssrl.76.3.299.
- 2408 Blais-Stevens, A., and Clague, J.J., 2001, Paleoseismic signature in late Holocene sediment cores
2409 from Saanich Inlet, British Columbia: *Marine Geology*, v. 175, p. 131–148,
2410 doi:10.1016/S0025-3227(01)00132-3.
- 2411 Blais-Stevens, A., Clague, J.J., Bobrowsky, P.T., and Patterson, R.T., 1997, Late Holocene
2412 sedimentation in Saanich Inlet, British Columbia, and its paleoseismic implications:
2413 *Canadian Journal of Earth Sciences*, v. 34, p. 1345–1357, doi:10.1139/e17-107.
- 2414 Blais-Stevens, A., Rogers, G.C., and Clague, J.J., 2011, A revised earthquake chronology for the
2415 last 4,000 years inferred from varve-bounded debris-flow deposits beneath an inlet near
2416 Victoria, British Columbia: *Seismological Society of America Bulletin*, v. 101, p. 1–12,
2417 doi:10.1785/0120090360.
- 2418 Black, B., 2014, Stratigraphic correlation of seismoturbidites and the integration of sediment
2419 cores with 3.5 kHz Chirp subbottom data in southern Cascadia [M.S. thesis]: Corvallis,
2420 Oregon State University, 211 p.
- 2421 Blott, S.J., and Pye, K., 2006, Particle size distribution analysis of sand-sized particles by laser
2422 diffraction: An experimental investigation of instrument sensitivity and the effects of
2423 particle shape: *Sedimentology*, v. 53, p. 671–685, doi:10.1111/j.1365-3091.2006.00786.x.


- 2424 Bock, Y., Prawirodirdjo, L., Genrich, J.F., Stevens, C.W., McCaffrey, R., Subarya, C.,
2425 Puntodewo, S.S.O., and Calais, E., 2003, Crustal motion in Indonesia from global
2426 positioning system measurements: *Journal of Geophysical Research*, v. 108, no. B8, 2367,
2427 doi:10.1029/2001JB000324.
- 2428 Boore, D.M., and Atkinson, G.M., 2008, Ground-motion prediction equations for the average
2429 horizontal component of PGA, PGV, and 5%-damped PSA at spectral periods between 0.01
2430 s and 10.0 s: *Earthquake Spectra*, v. 24, p. 99–138, doi:10.1193/1.2830434.
- 2431 Bothara, J., Beetham, R.D., Brunston, D., Stannard, M., Brown, R., Hyland, C., Lewis, W.,
2432 Miller, S., Sanders, R., and Sulistio, Y., 2010, General observations of effects of the 30th
2433 September 2009 Padang earthquake, Indonesia: *New Zealand Society for Earthquake
2434 Engineering Bulletin*, v. 43, p. 143–173.
- 2435 Bouma, A.H., 1962, *Sedimentology of some flysch deposits; a graphic approach to facies
2436 interpretation*: New York, Elsevier Publishing, 168 p.
- 2437 Bouma, A.H., 2004, Key controls on the characteristics of turbidite systems, *in* Lomas, S.A., and
2438 Joseph, P., eds., *Confined turbidite systems: Geological Society of London Special
2439 Publication 222*, p. 9–22, doi:10.1144/GSL.SP.2004.222.01.02
- 2440 Bowman, G.M., 1985, Oceanic reservoir correction for marine radiocarbon dates from
2441 northwestern Australia: *Australian Archaeology*, v. 20, p. 58–67.
- 2442 Bowman, G., and Harvey, N., 1983, Radiocarbon dating marine shells in South Australia:
2443 *Australian Archaeology*, v. 17, p. 113–123.
- 2444 Briggs, R.W., *et al.*, 2006, Deformation and slip along the Sunda megathrust in the great 2005
2445 Nias-Simeulue earthquake: *Science*, v. 311, p. 1897–1901, doi:10.1126/science.1122602.

- 2446 Bronk Ramsey, C., 1995, Radiocarbon calibration and analysis of stratigraphy: The OxCal
2447 program: *Radiocarbon*, v. 37, p. 425–430.
- 2448 Bronk Ramsey, C., 2001, Development of the radiocarbon program OxCal: *Radiocarbon*, v. 43,
2449 p. 355–363.
- 2450 Bronk Ramsey, C., 2008, Deposition models for chronological records: *Quaternary Science*
2451 *Reviews*, v. 27, p. 42–60, doi:10.1016/j.quascirev.2007.01.019.
- 2452 Bronk Ramsey, C., 2009a, Bayesian analysis of radiocarbon dates: *Radiocarbon*, v. 51, p. 337–
2453 360.
- 2454 Bronk Ramsey, C., 2009b, Dealing with outliers and offsets in radiocarbon dating: *Radiocarbon*,
2455 v. 51, no. 3, p. 28.
- 2456 Bürgmann, R., Kogan, M.G., Steblov, G.S., Hilley, G., Levin, V.E., and Apel, E., 2005,
2457 Interseismic coupling and asperity distribution along the Kamchatka subduction zone:
2458 *Journal of Geophysical Research*, v. 110, **B07405**, doi:10.1029/2005JB003648.
- 2459 Çağatay, M.M., **et al.**, 2012, Sedimentary earthquake records in the İzmit Gulf, Sea of Marmara,
2460 Turkey: *Sedimentary Geology*, v. 282, p. 347–359, doi:10.1016/j.sedgeo.2012.10.001.
- 2461 Caires, S., **and** Sterl, A., 2005, 100-year return value estimates for ocean wind speed and
2462 significant wave height from the ERA-40 data: *Journal of Climate*, v. 18, p. 1032–1048,
2463 **doi:10.1175/JCLI-3312.1.**
- 2464 Campbell, C.V., 1967, Lamina, laminaset, bed and bedset: *Sedimentology*, v. 8, p. 7–26,
2465 doi:10.1111/j.1365-3091.1967.tb01301.x.
- 2466 Campbell, K.W., 1997, Empirical near-source attenuation relationships for horizontal and
2467 vertical components of peak ground acceleration, peak ground velocity, and pseudo-absolute

- 2468 acceleration response spectra: *Seismological Research Letters*, v. 68, p. 154–179,
- 2469  doi:10.1785/gssrl.68.1.154.
- 2470 **[[Not cited? See query in text.]]** Carlson, P.R., 1967, Marine geology of Astoria submarine
2471 canyon [Ph.D. thesis]: Corvallis, Oregon State University, 259 p.
- 2472 Chang, C.-H., Chien, L.-K., and Chang, Y.-H., 2004, 3-D liquefaction potential analysis of
2473 seabed at nearshore area: *Journal of Marine Science and Technology*, v. 12, p. 141–151.
- 2474 Cheng, L.B., Sumer, M., and Freds, J., 2001, Solutions of pore pressure build up due to
2475 progressive waves: *International Journal for Numerical and Analytical Methods in*
2476 *Geomechanics*, v. 25, p. 885–907, doi:10.1002/nag.159.
- 2477 Chesley, S.R., and Ward, S.N., 2006, A quantitative assessment of the human and economic
2478 hazard from impact-generated tsunamis: *Natural Hazards*, v. 38, p. 355–374,
2479 doi:10.1007/s11069-005-1921-y.
- 2480 Chhibber, H., 1934, *Geology of Burma*: London, England, McMillan, 538 p.
- 2481 Chlieh, M., **et al.**, 2007, Coseismic slip and afterslip of the great (Mw 9.15) Sumatra-Andaman
2482 earthquake of 2004: *Seismological Society of America Bulletin*, v. 97, p. S152–S173,
2483 doi:10.1785/0120050631.
- 2484 Chlieh, M., Avouac, J.P., Sieh, K., Natawidjaja, D.H., and Galetzka, J., 2008, Heterogeneous
2485 coupling of the Sumatran megathrust constrained by geodetic and paleogeodetic
2486 measurements: *Journal of Geophysical Research*, v. 113, B05305,
2487 doi:10.1029/2007JB004981.
- 2488 Colella, H., Dieterich, J.H., Richards-Dinger, K., and Rubin, A., 2012, Complex characteristics
2489 of slow slip events in subduction zones reproduced in multi-cycle simulations: *Geophysical*
2490 *Research Letters*, v. 39, L20312, doi:10.1029/2012GL053276.

- 2491 Cowie, G., Calvert, S., De Lange, G., and Keil, R.H., 1998, Extents and implications of organic
2492 matter alteration at oxidation fronts in turbidites from the Madeira abyssal plain, *in* Weaver,
2493 P.P.E., *et al.*, eds., Proceedings of the Ocean Drilling Program, Scientific results, **Volume**
2494 **157: College Station, Texas, Ocean Drilling Program**, p. 581–590,
2495 [doi:10.2973/odp.proc.sr.157.150.1998](https://doi.org/10.2973/odp.proc.sr.157.150.1998).
- 2496 Dallimore, A., Thomson, R.E., and Bertram, M.A., 2005, Modern to late Holocene deposition in
2497 an anoxic fjord on the west coast of Canada: Implications for regional oceanography,
2498 climate and paleoseismic history: *Marine Geology*, v. 219, p. 47–69,
2499 [doi:10.1016/j.margeo.2005.05.003](https://doi.org/10.1016/j.margeo.2005.05.003).
- 2500 Davis, E., Kinoshita, M., Becker, K., Wang, K., Asano, A., and Ito, Y., 2013, Episodic
2501 deformation and inferred slow slip at the Nankai subduction zone during the first decade of
2502 CORK borehole pressure and VLFE monitoring: *Earth and Planetary Science Letters*,
2503 v. 368, p. 110–118, [doi:10.1016/j.epsl.2013.03.009](https://doi.org/10.1016/j.epsl.2013.03.009).
- 2504 Dawson, A.G., 1999, Linking tsunami deposits, submarine slides and offshore earthquakes:
2505 *Quaternary International*, v. 60, p. 119–126, [doi:10.1016/S1040-6182\(99\)00011-7](https://doi.org/10.1016/S1040-6182(99)00011-7).
- 2506 Dawson, A.G., and Stewart, I., 2007, Tsunami deposits in the geological record: *Sedimentary*
2507 *Geology*, v. 200, p. 166–183, [doi:10.1016/j.sedgeo.2007.01.002](https://doi.org/10.1016/j.sedgeo.2007.01.002).
- 2508 Dean, S., McNeil, L.C., Henstock, T., Bull, J.M., Gulick, S.P.S., Austin, J.A., Jr., Bangs, N.L.B.,
2509 Djadjadihardja, Y., and Permana, H., 2010, Contrasting décollement and prism properties
2510 over the Sumatra 2004–2005 earthquake rupture boundary: *Science*, v. 329, p. 207–210,
2511 [doi:10.1126/science.1189373](https://doi.org/10.1126/science.1189373).
- 2512 Dennielou, B., Huchon, A., Beaudouin, C., and Berné, S., 2006, Vertical grain-size variability
2513 within a turbidite levee: Autocyclicity or allocyclicity? A case study from the Rhône neofan,


- 2514 Gulf of Lions, Western Mediterranean: *Marine Geology*, v. 234, p. 191–213,
2515 doi:10.1016/j.margeo.2006.09.019.
- 2516 Duncan, J.R., 1968. Late Pleistocene and postglacial sedimentation and stratigraphy of deep-sea
2517 environments off Oregon [Ph.D. thesis]: Corvallis, Oregon State University, 222 p.
- 2518 Dura, T., Rubin, C.M., Kelsey, H.M., Horton, B.P., Hawkes, A., Vane, C.H., Daryono, M.,
2519 Grand Pre, C., Ladinsky, T., and Bradley, S., 2011, Stratigraphic record of Holocene
2520 coseismic subsidence, Padang, West Sumatra: *Journal of Geophysical Research*,
2521 v. 116, B11306, doi:10.1029/2011JB008205.
- 2522 Dutta, K., Bhushan, R., and Somayajulu, B.L.K., 2001, ΔR correction values for the northern
2523 Indian Ocean: *Radiocarbon*, v. 43, p. 483–488.
- 2524 Enkin, R.J., Dallimore, A., Baker, J., Southon, J., Ivaniochko, T., and Lian, O., 2013, A new
2525 high-resolution radiocarbon Bayesian age model of the Holocene and late Pleistocene from
2526 core MD02–2494 and others, Effingham Inlet, British Columbia, Canada; with an
2527 application to the paleoseismic event chronology of the Cascadia Subduction Zone:
2528 *Canadian Journal of Earth Sciences*, v. 50, p. 746–760, doi:10.1139/cjes-2012-0150.
- 2529 Ericson, D.B., Ewing, M., and Heezen, B.C., 1952, Turbidity currents and sediments in the North
2530 Atlantic: *American Association of Petroleum Geologists Bulletin*, v. 36, p. 489–511.
- 2531 Fairbanks, R.G., Mortlock, R.A., Chiu, T.-C., Cao, L., Kaplan, A., Guilderson, T.P., Fairbanks,
2532 T.W., Bloom, A.L., Gootes, P.M., Nadeau, M.-J., 2005, Radiocarbon calibration curve
2533 spanning 0 to 50,000 years BP based on paired $^{230}\text{Th}/^{234}\text{U}/^{238}\text{U}$ and ^{14}C dates on pristine
2534 corals: *Quaternary Science Reviews*, v. 24, p. 1781–1796.
- 2535 Faure, G., and Mensing, T.M., 2005, *Isotopes principles and applications (third edition)*: New
2536 York, John Wiley and Sons, 928 p.

- 2537 Felix, M., and Peakall, J., 2006, Transformation of debris flows into turbidity currents:
2538 Mechanisms inferred from laboratory experiments: *Sedimentology*, v. 53, p. 107–123,
2539 doi:10.1111/j.1365-3091.2005.00757.x.
- 2540 Fisher, D., Mosher, D., Austin, J.A., Gulick, S.P., Masterlark, T., and Moran, K., 2007, Active
2541 deformation across the Sumatran forearc over the December 2004 Mw 9.2 rupture: *Geology*,
2542 v. 35, p. 99–102, doi:10.1130/G22993A.1.
- 2543 Flynn, W.W., 1968, The determination of low levels of polonium-210 in environmental
2544 materials: *Analytica Chimica Acta*, v. 43, p. 221–227, doi:10.1016/S0003-2670(00)89210-7.
- 2545 Fornes, W.L., DeMaster, D.J., and Smith, C.R., 2001, A particle introduction experiment in
2546 Santa Catalina Basin: Testing the age-dependent mixing hypothesis: *Journal of Marine*
2547 *Research*, v. 59, p. 97–112, doi:10.1357/002224001321237380.
- 2548 Fujino, S., Naruse, H., Matsumoto, D., Jarupongsakul, T., Sphawajruksakul, A., and Sakakura,
2549 N., 2009, Stratigraphic evidence for pre-2004 tsunamis in southwestern Thailand: *Marine*
2550 *Geology*, v. 262, p. 25–28, doi:10.1016/j.margeo.2009.02.011.
- 2551 **[[Fujino et al., 2010, is cited in Figure 11. Please provide full reference or delete from**
2552 **figure.]]** 
- 2553 Fukuma, K., 1998, Origin and applications of whole-core magnetic susceptibility of sediments
2554 and volcanic rocks from Leg 152, in **Saunders, A.D., et al., eds.**, *Proceedings of the Ocean*
2555 *Drilling Program, Scientific results, Volume 152: College Station, Texas, Ocean Drilling*
2556 *Program*, p. 271–280, doi:10.2973/odp.proc.sr.152.225.1998.
- 2557 Garrett, A.M., Goldfinger, C., Patton, J.R., and Morey, A.M., 2011, “Paleoseismograms”:
2558 Testing a hypothesis of source-time function recording of paleoearthquakes: *American*
2559 *Geophysical Union*, fall meeting, abs. T51F-2421.

- 2560 Gillespie, R., 1977, Sydney University natural radiocarbon measurements IV: Radiocarbon,
2561 v. 19, p. 101–110.
- 2562 Gillespie, R., and Polach, H., 1979, The suitability of marine shells for radiocarbon dating of
2563 Australian prehistory, *in* Berger, R., and Suess, H., eds., Proceedings of the 9th International
2564 Conference on Radiocarbon Dating: Los Angeles: University of California Press. p. 404–
2565 421.
- 2566 Gilmore, G., and Hemingway, J.D., 1995, Practical gamma-ray spectrometry: New York, Wiley,
2567 314 p.
- 2568 Goldfinger, C., 2009, Sub-aqueous paleoseismology, *in* McCalpin, J.P., ed., Paleoseismology
2569 (second edition): International Geophysics Series Volume 95: New York, Academic Press-
2570 Elsevier, p. 119–170.
- 2571 Goldfinger, C., 2010, Submarine paleoseismology based on turbidite records: Annual Review of
2572 Marine Science, v. 3, p. 35–66, doi:10.1146/annurev-marine-120709-142852.
- 2573 Goldfinger, C., 2011, Possible turbidite record of earthquake source characteristics: A small
2574 scale test: U.S. Geological Survey National Earthquake Hazards Reduction Program Report
2575 07HQGR0064, 18 p.
- 2576 Goldfinger, C., and Morey, A., 2004, Physical property correlations from Cascadia great
2577 earthquakes: What are they telling us about the triggering events?: Eos (Transactions,
2578 American Geophysical Union), v. 85, abs. OS21E–01.
- 2579 Goldfinger, C., Nelson, C.H., and Johnson, J.E., 2003, Holocene earthquake records from the
2580 Cascadia Subduction Zone and northern San Andreas fault based on precise dating of
2581 offshore turbidites: Annual Review of Earth and Planetary Sciences, v. 31, p. 555–577,
2582 doi:10.1146/annurev.earth.31.100901.141246.

- 2583 Goldfinger, C., Morey, A.E., Nelson, C.H., Gutierrez-Pastor, J., Johnson, J.E., Karabanov, E.,
2584 Chaytor, J., and Ericsson, A., 2007, Rupture lengths and temporal history of significant
2585 earthquakes on the offshore and north coast segments of the northern San Andreas fault
2586 based on turbidite stratigraphy: *Earth and Planetary Science Letters*, v. 254, p. 9–27,
2587 doi:10.1016/j.epsl.2006.11.017.
- 2588 Goldfinger, C., **et al.**, 2008, Late Holocene rupture of the northern San Andreas fault and
2589 possible stress linkage to the Cascadia Subduction Zone: *Seismological Society of America*
2590 *Bulletin*, v. 98, p. 861–889, doi:10.1785/0120060411.
- 2591 Goldfinger, C., **et al.**, 2012a, Turbidite event history: Methods and implications for Holocene
2592 paleoseismicity of the Cascadia Subduction Zone: **U.S. Geological Survey Professional**
2593 **1661–F, 170 p., <http://pubs.usgs.gov/pp/pp1661f/>.**
- 2594 Goldfinger, C., Garrett, A.M., Patton, J.R., and Morey, A.E., 2012b, Paleoseismograms: Can
2595 turbidite deposits record flow unsteadiness imparted by earthquakes?: *American*
2596 *Geophysical Union*, fall meeting, abs. T22D–06.
- 2597 Goldfinger, C., Ikeda, Y., Yeats, R.S., and Ren, J., 2013a, Superquakes and supercycles:
2598 *Seismological Research Letters*, v. 84, p. 24–32, doi:10.1785/0220110135.
- 2599 Goldfinger, C., Morey, A., Black, B., **and** Patton, J.R., 2013b, Spatially limited mud turbidites on
2600 the Cascadia Margin: Segmented earthquake ruptures: *Natural Hazards and Earth System*
2601 *Sciences*, v. 13, p. 2109–2146, doi:10.5194/nhess-13-2109-2013.
- 2602 Goldfinger, C., Patton, J.R., Van Daele, M., Moernaut, J., Nelson, C.H., de Batist, M., and
2603 Morey, A.E., 2014a, Can turbidites be used to reconstruct a paleoearthquake record for the
2604 central Sumatran margin?: *Comment: Geology*, v. 42, p. e344, doi:10.1130/G35558C.1.

- 2605 Goldfinger, C., Hamilton, T.S., Beeson, J., Galer, S., Nelson, C.H., Morey, A., and Udrekh,
2606 2014b, Turbidite paleoseismology: Site selection, physiography, sediment supply, current
2607 dynamics and temporal considerations as applied in Cascadia and elsewhere: American
2608 Geophysical Union, fall meeting, abs. T52A-08.
- 2609 Gonzalez-Yajimovich, O.E., Gorsline, D.S., and Douglas, R.G., 2007, Frequency and sources of
2610 basin floor turbidites in Alfonso Basin, Gulf of California, Mexico: Products of slope
2611 failures: *Sedimentary Geology*, v. 199, p. 91–105, doi:10.1016/j.sedgeo.2005.09.025.
- 2612 Gorsline, D.S., De Diego, T., and Nava-Sanchez, E.H., 2000, Seismically triggered turbidites in
2613 small margin basins: Alfonso Basin, western Gulf of California and Santa Monica Basin,
2614 California borderland: *Sedimentary Geology*, v. 135, p. 21–35, doi:10.1016/S0037-
2615 0738(00)00060-9.
- 2616 Goto, H., Morikawa, H., Inatani, M., Ogura, Y., Tokue, S., Zhang, X.-X., Iwasaki, M., Araki,
2617 M., Sawada, S., and Zerva, A., 2012, Very dense seismic array observations in Furukawa
2618 District, Japan: *Seismological Research Letters*, v. 83, p. 765–774,
2619 doi:10.1785/0220120044.
- 2620 Gràcia, E., Vizcaino, A., Escutia, C., Asioli, A., Rodés, Á., Pallàs, R., Garcia-Orellana, J.,
2621 Lebreiro, S., and Goldfinger, C., 2010, Holocene earthquake record offshore Portugal (SW
2622 Iberia): Testing turbidite paleoseismology in a slow-convergence margin: *Quaternary*
2623 *Science Reviews*, v. 29, p. 1156–1172, doi:10.1016/j.quascirev.2010.01.010.
- 2624 Gràcia, E., et al., 2012, Acoustic and seismic imaging of the Adra fault (NE Alboran Sea): In
2625 search of the source of the 1910 Adra earthquake: *Natural Hazards Earth System Sciences*,
2626 v. 12, p. 3255–3267, doi:10.5194/nhess-12-3255-2012.

- 2627 Graehl, N.A., Kelsey, H.M., Witter, R.C., Hemphill-Haley, E., and Englehart, S.E., 2014,
2628 Stratigraphic and microfossil evidence for a 4500-year history of Cascadia subduction zone
2629 earthquakes and tsunamis at Yaquina River estuary, Oregon, USA: Geological Society of
2630 America Bulletin, v. 127, p. 211–226, doi:10.1130/B31074.1.
- 2631 Graindorge, D., et al., 2008, Impact of lower plate structure on upper plate deformation at the
2632 NW Sumatran convergent margin from seafloor morphology: Earth and Planetary Science
2633 Letters, v. 275, p. 201–210, doi:10.1016/j.epsl.2008.04.053.
- 2634 Grand Pre, C., Horton, B., Kelsey, H., Rubin, C., Hawkes, A., Natawidjaja, D.H., Daryono, M.,
2635 Yulianto, E., 2008, Application of microfossils to reconstruct a paleoseismic record of the
2636 Sunda subduction megathrust, northern Sumatra: Eos (Transactions, American Geophysical
2637 Union), v. 89, abs. U51A–0010.
- 2638 Grantz, A., Phillips, R.L., Mullen, M.W., Starratt, S.W., Jones, G.A., and Naidu, A.S., 1996,
2639 Character, paleoenvironment, rate of accumulation, and evidence for seismic triggering of
2640 Holocene turbidites, Canada Abyssal Plain, Arctic Ocean: Marine Geology, v. 133, p. 51–
2641 73, doi:10.1016/0025-3227(96)00015-1.
- 2642 Griggs, G.B., 1969, Cascadia Channel—The anatomy of a deep sea channel [Ph.D. thesis]:
2643  Corvallis, Oregon State University, 183 p.
- 2644 **[[Not cited?]]** Griggs, G.B., 2011, The first ocean floor evidence of great Cascadia earthquakes:
2645 Eos (Transactions, American Geophysical Union), v. 92, p. 325–336,
2646 doi:10.1029/2011EO390001.
- 2647 Griggs, G.B., and Kulm, L.D., 1970, Sedimentation in Cascadia deep-sea channel: Geological
2648 Society of America Bulletin, v. 81, p. 1361–1384, doi:10.1130/0016-
2649 7606(1970)81[1361:SICDC]2.0.CO;2.

- 2650 Gulick, S.P.S., [Austin, J.A.](#), Jr., [McNeill, L.C.](#), Bangs, N.L.B., Martin, K.M., Henstock, T.J.,
2651 Bull, J.M., Dean, S., Djadjadihardja, Y.S., and Permana, H., 2011, Updip rupture of the
2652 2004 Sumatra earthquake extended by thick indurated sediments: *Nature Geoscience*, v. 4,
2653 p. 453–456, doi:10.1038/ngeo1176.
- 2654 Gutiérrez-Pastor, J., Nelson, C. H., Goldfinger, C., and Johnson, J. E., 2005a, Holocene turbidite
2655 and onshore paleoseismic record of great earthquakes on the Cascadia Subduction Zone:
2656 Relevance for the Sumatra 2004 great earthquake: *Eos (Transactions, American Geophysical*
2657 *Union)*, v. 86, abs. U51A–03.
- 2658 Gutiérrez-Pastor, J., Nelson, C.H., Goldfinger, C., and Johnson, J.E., 2005b, Holocene turbidite
2659 history in the Cascadia Subduction Zone shows the potential to develop paleoseismic
2660 methods for the Sumatra and other subduction zones: *Geophysical Research Abstracts*, v. 7,
2661 no. 07269, p. 3.
- 2662 Gutiérrez-Pastor, J., Nelson, C.H., Goldfinger, C., Johnson, J.E., Escutia, C., Eriksson, A.T., and
2663 Morey, A.E., 2009, Earthquake control of Holocene turbidite frequency confirmed by
2664 hemipelagic sedimentation chronology on the Cascadia and northern California active
2665 continental margins, *in* [Kneller, B.C.](#), [et al.](#), eds., *External controls of deep-water*
2666 *depositional systems: Society for Sedimentary Geology (SEPM) Special Publication 92*, p.
2667 [179–197](#), doi:10.2110/sepm.sp.092.179.
- 2668 Gutiérrez-Pastor, J., Nelson, C.H., Goldfinger, C., and Escutia, C., 2013, Sedimentology of
2669 seismo-turbidites off the Cascadia and northern California active tectonic continental
2670 margins, northwest Pacific Ocean: *Marine Geology*, v. 336, p. 99–119,
2671 doi:10.1016/j.margeo.2012.11.010.


- 2672 Hagstrum, J.T., Atwater, B.F., and Sherrod, B.L., 2004, Paleomagnetic correlation of late
2673 Holocene earthquakes among estuaries in Washington and Oregon: Geochemistry,
2674 Geophysics, Geosystems, v. 5, Q10001, doi:10.1029/2004GC000736.
- 2675 Hammond, D.E., McManus, J., Berelson, W.M., Kilgore, T.E., and Pope, R.H., 1996, Early
2676 diagenesis of organic material in equatorial Pacific sediments: stoichiometry and kinetics:
2677 Deep-Sea Research II, v. 43, p. 1365–1412, doi:10.1016/0967-0645(96)00027-6.
- 2678 Hampton, M.A., Bouma, A.H., Carlson, P.R., Molnia, B.F., Clukey, E.C., and Sangrey, D.A.,
2679 1978, Quantitative study of slope instability in the Gulf of Alaska: Houston, Texas, Offshore
2680 Technology Conference, OTC-3314-MS, p. 2307–2318, doi:10.4043/3314-MS.
- 2681 Hampton, M.A., Lee, H.J., and Locat, J., 1996, Submarine landslides: Reviews of Geophysics,
2682 v. 34, p. 33–59, doi:10.1029/95RG03287.
- 2683 Hayes, G.P., Bergman, E., Johnson, K.L., Benz, H.M., Brown, L., Meltzer, A.S., 2013,
2684 Seismotectonic framework of the 2010 February 27 M_w 8.8 Maule, Chile earthquake
2685 sequence: Geophysical Journal International, v. 195, p. 1034–1051, doi:10.1093/gji/ggt238.
- 2686 Heki, K., and Mitsui, Y., 2013, Accelerated pacific plate subduction following interplate thrust
2687 earthquakes at the Japan trench: Earth and Planetary Science Letters, v. 363, p. 44–49,
2688 doi:10.1016/j.epsl.2012.12.031.
- 2689 Hemphill-Haley, E., 1995, Diatom evidence for earthquake-induced subsidence and tsunami 300
2690 yr ago in southern coastal Washington: Geological Society of America Bulletin, v. 107,
2691 p. 367–378, doi:10.1130/0016-7606(1995)107<0367:DEFEIS>2.3.CO;2.
- 2692 Henkart, P., 2011, SIOSEIS—The introduction: Software package sponsored by the National
2693 Science Foundation and the Scripps Industrial Associates:
2694 <http://sioseis.ucsd.edu/sioseis.html>.

- 2695 Henstock, T.J., McNeill, L.C., and Tappin, J.R., 2006, Seafloor morphology of the Sumatran
2696 subduction zone: Surface rupture during megathrust earthquakes?: *Geology*, v. 34, p. 485–
2697 488, doi:10.1130/22426.1.
- 2698 Hindle, D., and Mackey, K., 2011, Earthquake recurrence and magnitude and seismic
2699 deformation of the northwestern Okhotsk plate, northeast Russia: *Journal of Geophysical*
2700 *Research*, v. 116, B02301, doi:10.1029/2010JB007409.
- 2701 Hok, S., Fukuyama, E., and Hashimoto, C., 2011, Dynamic rupture scenarios of anticipated
2702 Nankai-Tonankai earthquakes, southwest Japan: *Journal of Geophysical Research*,
2703 v. 116, B12319, doi:10.1029/2011JB008492.
- 2704 Howard, A.D., 1994, A detachment-limited model of drainage basin evolution: *Water Resources*
2705 *Research*, v. 30, p. 2261–2285, doi:10.1029/94WR00757.
- 2706 Howard, A.D., 1997, Badland morphology and evolution: Interpretation using a simulation
2707 model: *Earth Surface Processes and Landforms*, v. 22, p. 211–227, doi:10.1002/(SICI)1096-
2708 9837(199703)22:3<211::AID-ESP749>3.0.CO;2-E.
- 2709 Hsu, Y.-j., Simons, M., Avouac, J., Galetzka, J., Sieh, K., Chlieh, M., Natawidjaja, D.H.,
2710 Prawirodirdjo, L., and Bock, Y., 2006, Frictional afterslip following the 2005 Nias-Simeulue
2711 earthquake, Sumatra: *Science*, v. 312, p. 1921–1926, doi:10.1126/science.1126960.
- 2712 Hua, Q., Woodroffe, C., Barbetti, M., Smithers, S., Zoppi, U., and Fink, D., 2004, Marine
2713 reservoir correction for the Cocos (Keeling) Islands, Indian Ocean: *Radiocarbon*, v. 46,
2714 p. 603–610.
- 2715 Hughen, K., Lehman, S., Southon, J., Overpeck, J., Marchal, O., Herring, C., and Turnbull, J.,
2716 2004, ¹⁴C activity and global carbon cycle changes over the past 50,000 years: *Science*,
2717 v. 303, p. 202–207, doi:10.1126/science.1090300.

- 2718 Huh, C.A., Su, C.C., Liang, W.T., and Ling, C.Y., 2004, Linkages between turbidites in the
2719 southern Okinawa Trough and submarine earthquakes: *Geophysical Research Letters*,
2720 v. 31, L12304, doi:10.1029/2004GL019731.
- 2721 Huh, C.-A., Su, C.-C., Wang, C.-H., Lee, S.-Y., and Lin, I.-T., 2006, Sedimentation in the
2722 Southern Okinawa Trough—Rates, turbidites and a sediment budget: *Marine Geology*,
2723 v. 231, p. 129–139, doi:10.1016/j.margeo.2006.05.009.
- 2724 Ide, S., 2013, The proportionality between relative plate velocity and seismicity in subduction
2725 zones: *Nature Geoscience*, v. 6, p. 780–784, doi:10.1038/NGEO1901.
- 2726 Ikehara, K., Kanamatsu, T., Strasser, M., Fink, H., Nagahashi, Y., Usami, K., and Wefer, G.,
2727 2012, Past “earthquake/tsunami” event deposits found in the Japan Trench: Results from the
2728 Sonne SO219A and Mirai MR12–E01 cruises: American Geophysical Union, fall meeting,
2729 abs. NH41C–02.
- 2730 Ikehara, K., Irino, T., Usami, K., Jenkins, R., Omura, A., and Ashi, J., 2014, Possible submarine
2731 tsunami deposits on the outer shelf of Sendai Bay, Japan resulting from the 2011 earthquake
2732 and tsunami off the Pacific coast of Tohoku: *Marine Geology*, v. 349, p. 91–98,
2733 doi:10.1016/j.margeo.2014.01.001.
- 2734 Inouchi, Y., Kinugasa, Y., Kumon, F., Nakano, S., Yasumatsu, S., and Shiki, T., 1996,
2735 Turbidites as records of intense palaeoearthquakes in Lake Biwa: Japan: *Sedimentary*
2736 *Geology*, v. 104, p. 117–125, doi:10.1016/0037-0738(95)00124-7.
- 2737 Ishii, M., Shearer, P.M., Houston, H., and Vidale, J.E., 2005, Extent, duration and speed of the
2738 2004 Sumatra-Andaman earthquake imaged by the Hi-Net array: *Nature*, v. 435, p. 933–936,
2739 doi:10.1038/nature03675.

- 2740 Ishii, M., Shearer, P.M., Houston, H., and Vidale, J.E., 2007, Teleseismic P wave imaging of the
2741 26 December 2004 Sumatra-Andaman and 28 March 2005 Sumatra earthquake ruptures
2742 using the Hi-net array: *Journal of Geophysical Research*, v. 112, B11307,
2743 doi:10.1029/2006JB004700.
- 2744 Izaguirre, C., Mendez, F.J., Mendez, M., and Losada, I.J., 2011, Global extreme wave height
2745 variability based on satellite data: *Geophysical Research Letters*, v. 38, L10607,
2746 doi:10.1029/2011GL047302.
- 2747 Jacob, J., Dymant, J., and Yatheesh, V., 2014, Revisiting the structure, age, and evolution of the
2748 Wharton Basin to better understand subduction under Indonesia: *Journal of Geophysical*
2749 *Research*, v. 119, p. 1–22, doi:10.1002/2013JB010285.
- 2750 Jankaew, K., Atwater, B.F., Sawai, Y., Charoentitirat, T., Martin, M.E., and Prendergast, A.,
2751 2008, Medieval forewarning of the 2004 Indian Ocean tsunami in Thailand: *Nature*, v. 455,
2752 p. 1228–1231, doi:10.1038/nature07373.
- 2753 Johnson, J.E., Goldfinger, C., Trehu, A.M., Bangs, N.L.B., Torres, M.E., and Chevallier, J.,
2754 2005, North-south variability in the history of deformation and fluid venting across Hydrate
2755 Ridge, Cascadia Margin, *in* Tréhu, A.M., et al., eds., *Proceedings of the Ocean Drilling*
2756 *Program, Scientific results, Volume 204: College Station, Texas, Ocean Drilling Program*, p.
2757 1–16, doi:10.2973/odp.proc.sr.204.125.2006
- 2758 Kagan, Y.Y., Jackson, D.D., and Geller, R.J., 2012, Characteristic earthquake model, 1884–
2759 2011, R.I.P.: *Seismological Research Letters*, v. 83, p. 951–953, doi:10.1785/0220120107.
- 2760 Kanamori, H., Rivera, L., and Lee, W.H.K., 2010, Historical seismograms for unravelling a
2761 mysterious earthquake: The 1907 Sumatra earthquake: *Geophysical Journal International*,
2762 v. 183, p. 358–374, doi:10.1111/j.1365-246X.2010.04731.x.

- 2763 Karig, D.E., Lawrence, M.B., Moore, G.F., and Curray, J.R., 1980, Structural framework of the
2764 forearc basin, NW Sumatra: Geological Society of London Journal, v. 137, p. 77–91,
2765 doi:10.1144/gsjgs.137.1.0077.
- 2766 Karlin, R.E., and Abella, S.E.B., 1992, Paleoearthquakes in the Puget Sound region recorded in
2767 sediments from Lake Washington, U.S.A.: Science, v. 258, p. 1617–1620,
2768 doi:10.1126/science.258.5088.1617.
- 2769 Karlin, R.E., and Abella, S.E.B., 1996, A history of Pacific Northwest earthquakes recorded in
2770 Holocene sediments from Lake Washington: Journal of Geophysical Research, v. 101, no.
2771 B3, p. 6137–6150.
- 2772 Karlin, R., and Seitz, G., 2007, Final Technical Report for 07HQGR0014 and 07HQGR0008: A
2773 basin wide record of earthquakes at Lake Tahoe: Validation of the earthquake induced
2774 turbidite model with sediment core analysis: Collaborative Research with UNR and SDSU:
2775 U.S. Geological Survey National Earthquake Hazards Reduction Program, 18 p.
- 2776 Karlin, R.E., Holmes, M., Abella, S.E.B., and Sylwester, R., 2004, Holocene landslides and a
2777 3500-year record of Pacific Northwest earthquakes from sediments in Lake Washington:
2778 Geological Society of America Bulletin, v. 116, p. 94–108, doi:10.1130/B25158.1.
- 2779 Kastens, K.A., and Cita, M.B., 1981, Tsunami-induced sediment transport in the abyssal
2780 Mediterranean Sea: Geological Society of America Bulletin, v. 92, p. 845–857,
2781 doi:10.1130/0016-7606(1981)92<845:TSTITA>2.0.CO;2.
- 2782 Kayen, R.E., and Mitchell, J.K., 1997, Assessment of liquefaction potential during earthquakes
2783 by Arias intensity: Journal of Geotechnical and Geoenvironmental Engineering, v. 123, p.
2784 1162–1174, doi:10.1061/(ASCE)1090-0241(1997)123:12(1162).

- 2785 Keefer, D.K., 1984, Landslides caused by earthquakes: Geological Society of America Bulletin,
2786 v. 95, p. 406–421, doi:10.1130/0016-7606(1984)95<406:LCBE>2.0.CO;2.
- 2787 Kelsey, H.M., Witter, R.C., and Hemphill-Haley, E., 2002, Plate-boundary earthquakes and
2788 tsunamis of the past 5500 yr, Sixes River estuary, southern Oregon: Geological Society of
2789 America Bulletin, v. 114, p. 298–314, doi:10.1130/0016-
2790 7606(2002)114<0298:PBEATO>2.0.CO;2.
- 2791 Kelsey, H.M., Nelson, A.R., Hemphill-Haley, E., and Witter, R.C., 2005, Tsunami history of an
2792 Oregon coastal lake reveals a 4600 yr record of great earthquakes on the Cascadia
2793 subduction zone: Geological Society of Society of America Bulletin, v. 117, p. 1009–1032,
2794  doi:10.1130/B25452.1.
- 2795 **[[Not cited? See query in text.]]** Kiser, E., and Ishii, M., 2011, The 2010 Mw 8.8 Chile
2796 earthquake: Triggering on multiple segments and frequency dependent rupture behavior:
2797 Geophysical Research Letters, v. 38, L07301, doi:10.1029/2011GL047140.
- 2798 Klug, C., Cashman, K.V., and Bacon, C.R., 2002, Structure and physical characteristics of
2799 pumice from the climactic eruption of Mount Mazama (Crater Lake), Oregon: Bulletin of
2800 Volcanology, v. 34, p. 486–501, doi:10.1007/s00445-002-0230-5.
- 2801 Kneller, B., and Buckee, C., 2000, The structure and fluid mechanics of turbidity currents: A
2802 review of some recent studies and their geological implications: Sedimentology, v. 47,
2803 p. 62–94, doi:10.1046/j.1365-3091.2000.047s1062.x.
- 2804 Kneller, B., and McCaffrey, B., 1995, Modeling the effects of salt-induced topography on
2805 deposition from turbidity currents, *in* Travis, C., **et al., eds.**, Gulf Coast Section Society of
2806 Economic Paleontologists and Mineralogists Foundation Sixteenth annual research

- 2807 conference: Houston, Texas, Gulf Coast Section Society of Economic Paleontologists
2808 Foundation, p. 137–145.
- 2809 Kneller, B.C., and McCaffrey, W.D., 2003, The interpretation of vertical sequences in turbidite
2810 beds: The influence of longitudinal flow structure: *Journal of Sedimentary Research*, v. 73,
2811 p. 706–713, doi:10.1306/031103730706.
- 2812 Komen, G.J., Cavaleri, L., Donelan, M., Hasselmann, K., Hasselmann, S., and Janssen,
2813 P.A.E.M., 1994, *Dynamics and modeling of ocean waves*: Cambridge, Cambridge
2814 University Press, 556 p.
- 2815 Konca, A.O., Hjorleifsdottir, V., Song, T.A., Avouac, J., Helmberger, D., Ji, C., Briggs, R.W.,
2816 and Meltzner, A.J., 2007, Rupture kinematics of the 2005 Mw 8.6 Nias–Simeulue
2817 earthquake from the joint inversion of seismic and geodetic data: *Seismological Society of*
2818 *America Bulletin*, v. 97, p. S307–S322, doi:10.1785/0120050632.
- 2819 Konca, A.O., *et al.*, 2008, Partial rupture of a locked patch of the Sumatra Megathrust during the
2820 2007 earthquake sequence: *Nature*, v. 456, p. 631–635, doi:10.1038/nature07572.
- 2821 Kopp, H., 2013 The control of subduction zone structural complexity and geometry on margin
2822 segmentation and seismicity: *Tectonophysics*, v. 589, p. 1–16,
2823 doi:10.1016/j.tecto.2012.12.037.
- 2824 Kopp, H., *et al.*, 2008, Lower slope morphology of the Sumatra trench system: *Basin Research*,
2825 v. 20, p. 519–529, doi:10.1111/j.1365-2117.2008.00381.x.
- 2826 Kramer, S.L., and Lindwall, N.W., 2004, Dimensionality and directionality effects in Newmark
2827 sliding block analyses: *Journal of Geotechnical and Geoenvironmental Engineering*, v. 130,
2828 p. 303–315, doi:10.1061/(ASCE)1090-0241(2004)130:3(303).

- 2829 Ladage, S., Weinrebe, W., Gaedicke, C., Barckhausen, U., Flueh, E.R., Heyde, I., Krabbenhoeft,
2830 A., Kopp, H., **Fahar, S., and Djadjadihardja, Y.**, 2006, Bathymetric survey images structure
2831 off Sumatra: **Eos (Transactions, American Geophysical Union)**, v. 87, p. 165–172.
- 2832 Lamb, M.P., Tonolio, H., and Parker, G., 2006, Trapping of sustained turbidity currents by
2833 intraslope minibasins: *Sedimentology*, v. 53, p. 147–160, doi:10.1111/j.1365-
2834 3091.2005.00754.x.
- 2835 Lay, T., **et al.**, 2005, The great Sumatra-Andaman earthquake of 26 December 2004: *Science*, v.
2836 308, p. 1127–1133, doi:10.1126/science.1112250.
- 2837 Lees, J.A., Flower, R.J., Ryves, D., Vologina, E., and Sturm, M., 1998a, Identifying
2838 sedimentation patterns in Lake Baikal using whole core and surface scanning magnetic
2839 susceptibility: *Journal of Paleolimnology*, v. 20, p. 187–202,
2840 doi:10.1023/A:1008043230549.
- 2841 Lees, J.A., Fowler, R.J., and Appleby, P.G., 1998b, Mineral magnetic and physical properties of
2842 surficial sediments and onshore samples from the southern basin of Lake Baikal, Siberia:
2843 *Journal of Paleolimnology*, v. 20, p. 175–186, doi:10.1023/A:1008040824614.
- 2844 Leonard, L.J., Hyndman, R.D., and Mazzotti, S., 2004, Coseismic subsidence in the 1700 great
2845 Cascadia earthquake: Coastal estimates versus elastic dislocation models: *Geological*
2846 *Society of Society of America Bulletin*, v. 116, p. 655–670, doi:10.1130/B25369.1.
- 2847 Leonard, L.J., Currie, C.A., Mazzotti, S., and Hyndman, R.D., 2010, Rupture area and
2848 displacement of past Cascadia great earthquakes from coastal coseismic subsidence:
2849 *Geological Society of Society of America Bulletin*, v. 122, p. 1951–1968,
2850 doi:10.1130/B30108.1.

- 2851 Levesque, C.L., Locat, J., and Leroueil, S., 2006, Dating submarine mass movements triggered
2852 by earthquakes in the Upper Saguenay Fjord, Quebec, Canada: *Norwegian Journal of*
2853 *Geology*, v. 86, p. 231–242.
- 2854 Lorenzoni, L., Thunell, R.C., Benitez-Nelson, C.R., Hollander, D., Martinez, N., Tappa, E.,
2855 Varela, R.N., Astor, Y., Muller-Karger, F.E., 2012, The importance of subsurface nepheloid
2856 layers in transport and delivery of sediments to the eastern Cariaco Basin, Venezuela: *Deep-*
2857 *Sea Research I*, v. 56, p. 2249–2262, doi:10.1016/j.dsr.2009.08.001.
- 2858 Lovlie, R., and Van Veen, P., 1995, Magnetic susceptibility of a 180 m sediment core:
2859 Reliability of incremental sampling and evidence for a relationship between susceptibility
2860 and gamma activity, *in* Turner, P., and Turner, A., eds., *Palaeomagnetic applications in*
2861 *hydrocarbon exploration and production: Geological Society of London Special Publication*
2862 98, p. 259–266, doi:10.1144/GSL.SP.1995.098.01.16.
- 2863 Lowe, D.R., 1982, Sediment gravity flows: II. Depositional models with special reference to the
2864 deposits of high-density turbidity currents: *Journal of Sedimentary Petrology*, v. 52, p. 279–
2865 297, doi:10.1306/212F7F31-2B24-11D7-8648000102C1865D.
- 2866 Mahani, A.B., and Atkinson, G.M., 2013, Regional differences in ground-motion amplitudes of
2867 small-to-moderate earthquakes across North America: *Seismological Society of America*
2868 *Bulletin*, v. 103, p. 2604–2620, doi:10.1785/0120120350.
- 2869 Major, C.O., Pirmez, C., Goldberg, D., and Party, L.S., 1998, High-resolution core-log
2870 integration techniques: Examples from the Ocean Drilling Program, *in* Harvey, P.K., and
2871 Lovell, M.A., eds., *Core-log integration: Geological Society of London Special Publication*
2872 136, p. 285–295, doi:10.1144/GSL.SP.1998.136.01.24.

- 2873 Malik, J.N., Shishikura, M., Echigo, T., Ikeda, Y., Satake, K., Kayanne, H., Sawai, Y., Murty,
2874 C.V.R., and Dikshit, D., 2011, Geologic evidence for two pre-2004 earthquakes during
2875 recent centuries near Port Blair, South Andaman Island, India: *Geology*, v. 39, p. 559–562,
2876 [doi:10.1130/G31707.1](https://doi.org/10.1130/G31707.1).
- 2877 Martin, W.R., and Sayles, F.L., 2003, The recycling of biogenic material at the seafloor, *in*
2878 [Mackenzie, F.T., ed.](#), *Treatise on Geochemistry Volume 7*: Amsterdam, Elsevier, p. 37–65,
2879 [doi:10.1016/B0-08-043751-6/07089-4](https://doi.org/10.1016/B0-08-043751-6/07089-4).
- 2880 Masson, D.G., Harbitz, C.B., Wynn, R.B., Pedersen, G., Løvholt, F., 2006, Submarine
2881 landslides: Processes, triggers and hazard prediction: Royal Society of London Philosophical
2882 Transactions, v. 364, p. 2009–2039, [doi:10.1098/rsta.2006.1810](https://doi.org/10.1098/rsta.2006.1810).
- 2883 Matson, R.G., and Moore, G., 1992, Structural influence on Neogene subsidence in the central
2884 Sumatra fore-arc basin: Southwest Pacific and eastern Indian Ocean margins, *in* [Watkins,](#)
2885 [J.S., et al., eds.](#), *Geology and geophysics of continental margins*: American Association of
2886 Petroleum Geologists *Memoir 53*, p. 157–181.
- 2887 McCalpin, J.P., 2009, Field techniques in paleoseismology—Terrestrial environments, *in*
2888 McCalpin, J.P., ed., *Paleoseismology*: San Diego, California, Academic Press, p. 29–118.
- 2889 McCalpin, J.P., and Nelson, A.R., 1996, Introduction to paleoseismology, *in* McCalpin, J.P., ed.,
2890 *Paleoseismology*: San Diego, California, Academic Press, p. 1–32.
- 2891 McGregor, H., Gagan, M., McCulloch, M., Hodge, E., and Mortimer, G., 2008, Mid-Holocene
2892 variability in the marine ¹⁴C reservoir age for northern coastal Papua New Guinea:
2893 *Quaternary Geochronology*, v. 3, p. 213–225, [doi:10.1016/j.quageo.2007.11.002](https://doi.org/10.1016/j.quageo.2007.11.002).
- 2894 McHugh, C.M.G., Seeber, L., Cormier, M.-H., Dutton, J., Çağatay, N., Polonia, A., Ryan,
2895 W.B.F., and Gorur, N., 2006, Submarine earthquake geology along the North Anatolia fault


- 2896 in the Marmara Sea, Turkey: A model for transform basin sedimentation: *Earth and*
2897 *Planetary Science Letters*, v. 248, p. 661–684, doi:10.1016/j.epsl.2006.05.038.
- 2898 McHugh, C.M.G., Braudy, N., Çağatay, M.M., Sorlien, C., Cormier, M., Seeber, L., and Henry,
2899 P., 2014, Seafloor fault ruptures along the North Anatolia fault in the Marmara Sea, Turkey:
2900 Link with the adjacent basin turbidite record: *Marine Geology*, v. 353, p. 65–83,
2901 doi:10.1016/j.margeo.2014.03.005.
- 2902 Meltzner, A.J., Sieh, K., Abrams, M., Agnew, D.C., Hudnut, K.W., Avouac, J.-P., and
2903 Natawidjaja, D.H., 2006, Uplift and subsidence associated with the great Aceh-Andaman
2904 earthquake of 2004: *Journal of Geophysical Research*, v. 111, B02407,
2905 doi:10.1029/2005JB003891.
- 2906 Meltzner, A.J., Sieh, K., Chiang, H., Shen, C., Suwargadi, B.W., Natawidjaja, D.H., Philibosian,
2907 B., Briggs, R.W., and Galetzka, J., 2010, Coral evidence for earthquake recurrence and an
2908 A.D. 1390–1455 cluster at the south end of the 2004 Aceh-Andaman rupture: *Journal of*
2909 *Geophysical Research*, v. 115, B10402, doi:10.1029/2010JB007499.
- 2910 Meltzner, A.J., Sieh, K., Chiang, H.-W., Shen, C.-C., Suwargadi, B.W., Natawidjaja, D.H.,
2911 Philibosian, B., and Briggs, R.W., 2012, Persistent termini of 2004- and 2005-like ruptures
2912 of the Sunda megathrust: *Journal of Geophysical Research*, v. 117, B04405,
2913 doi:10.1029/2011JB008888.
- 2914 Meunier, P., Hovius, N., and Haines, A.J., 2007, Regional patterns of earthquake-triggered
2915 landslides and their relation to ground motion: *Geophysical Research Letters*, v. 34, L20408,
2916 doi:10.1029/2007GL031337.

- 2917 Michels, K.H., Suckow, A., Breitzke, M., Kudrass, H.R., and Kottke, B., 2003, Sediment
2918 transport in the shelf canyon “Swatch of No Ground” (Bay of Bengal): Deep-Sea Research
2919 II, v. 50, p. 1003–1022, doi:10.1016/S0967-0645(02)00617-3.
- 2920 Middleton, G.V., 1967, Experiments on density and turbidity currents 111: Deposition of
2921 sediment: Canadian Journal of Earth Sciences, v. 4, p. 475–505, doi:0.1139/e67-025.
- 2922 Miyamoto, J., Sassa, S., and Sekiguchi, H., 2004, Progressive solidification of a liquefied sand
2923 layer during continued wave loading: Geotechnique, v. 54, p. 617–629,
2924 doi:10.1680/geot.2004.54.10.617.
- 2925 Moernaut, J., Batist, M.D., Charlet, F., Heirman, K., Chapron, E., Pino, M., Brümmer, R., and
2926 Urrutia, R., 2007, Giant earthquakes in south-central Chile revealed by Holocene mass-
2927 wasting events in Lake Puyehue: Sedimentary Geology, v. 195, p. 239–256,
2928 doi:10.1016/j.sedgeo.2006.08.005.
- 2929 Monecke, K., Anselmetti, F.S., Becker, A., Schnellmann, M., Sturm, M., and Giardini, D., 2006,
2930 Earthquake-induced deformation structures in lake deposits: A late Pleistocene to Holocene
2931 paleoseismic record for central Switzerland: Eclogae Geologicae Helvetiae, v. 99, p. 343–
2932 362, doi:10.1007/s00015-006-1193-x.
- 2933 Monecke, K., Finger, W., Klarer, D., Kongo, W., McAdoo, B., Moore, A., Sudrajat, S., 2008, A
2934 1,000-year sediment record of tsunami recurrence in northern Sumatra: Nature, v. 455, p.
2935 1232–1234, doi:10.1038/nature07374.
- 2936 Moore, D.G., Curray, J.R., and Emmell, F.J., 1976, Large submarine slide (olistostrome)
2937 associated with Sunda arc subduction zone, northeast Indian Ocean: Marine Geology, v. 21,
2938 p. 211–226, doi:10.1016/0025-3227(76)90060-8.


- 2939 Moore, G.F., and Karig, D.E., 1980, Structural geology of Nias Island, Indonesia: Implications
2940 for subduction zone tectonics: *Science*, v. 280, p. 193–223, doi:10.2475/ajs.280.3.193.
- 2941 Moreno, M.S., Bolte, J., Klotz, J., and Melnick, D., 2009, Impact of megathrust geometry on
2942 inversion of coseismic slip from geodetic data: Application to the 1960 Chile earthquake:
2943 *Geophysical Research Letters*, v. 36, L16310, doi:10.1029/2009GL039276.
- 2944 Moreno, M.S., et al., 2011, Heterogeneous plate locking in the south-central Chile subduction
2945 zone: Building up the next great earthquake: *Earth and Planetary Science Letters*, v. 305,
2946 p. 413–424, doi:10.1016/j.epsl.2011.03.025.
- 2947 Morgenstern, N.R., 1967, Submarine slumping and the initiation of turbidity currents, *in*
2948 **Richards, A., ed.**, *Marine géotechnique*: Urbana, University of Illinois Press, p. 189–220.
- 2949 Mosher, D.C., Moscardelli, L., Shipp, R.C., Chaytor, J.D., Baxter, C.D.P., Lee, H.J., and
2950 Urgeles, R., 2010, Submarine mass movements and their consequences, *in* Mosher, D.C., et
2951 **al., eds.**, *Submarine mass movements and their consequences*: New York, Springer, p. 1–8.
- 2952 Muck, M.T., and Underwood, M.B., 1990, Upslope flow of turbidity currents: A comparison
2953 among field observations, theory, and laboratory models: *Geology*, v. 18, p. 54–57,
2954 doi:10.1130/0091-7613(1990)018<0054:UFOTCA>2.3.CO;2.
- 2955 Mulder, T., Syvitski, J.P.M., Migeon, S., Faugeres, J.-C., and Savoye, B., 2003, Marine
2956 hyperpycnal flows: initiation, behavior and related deposits. A review: *Marine and*
2957 *Petroleum Geology*, v. 20, p. 861–882, doi:10.1016/j.marpetgeo.2003.01.003.
- 2958 Murray, J., and Segall, P., 2002, Testing time-predictable earthquake recurrence by direct
2959 measurement of strain accumulation and release: *Nature*, v. 419, p. 287–291,
2960 doi:10.1038/nature00984.

- 2961 Nair, R.R., Buynevich, I., Goble, R.J., Srinivasan, P., Murthy, S.G.N., Kandipal, S.C., Lakshmi,
2962 C.S.V., and Trivedi, I.D., 2010, Subsurface images shed light on past tsunamis in India: Eos
2963 (Transactions, American Geophysical Union), v. 91, p. 489–490,
2964 doi:10.1029/2010EO500002.
- 2965 Nakajima, T., 2000, Initiation processes of turbidity currents; implications for assessments of
2966 recurrence intervals of offshore earthquakes using turbidites: Geological Survey of Japan
2967 Bulletin, v. 51, p. 79–87.
- 2968 Nakajima, T., and Kanai, Y., 2000, Sedimentary features of seismoturbidites triggered by the
2969 1983 and older historical earthquakes in the eastern margin of the Japan Sea: Sedimentary
2970 Geology, v. 135, p. 1–19, doi:10.1016/S0037-0738(00)00059-2.
- 2971 Natawidjaja, D.H., Sieh, K., Ward, S.N., Cheng, H., Edwards, R.L., Galetzka, J., and Suwargadi,
2972 B.W., 2004, Paleogeodetic records of seismic and aseismic subduction from central
2973 Sumatran microatolls, Indonesia: Journal of Geophysical Research, v. 109, B04306,
2974 doi:10.1029/2003JB002398.
- 2975 Natawidjaja, D.H., Sieh, K., Chlieh, M., Galetzka, J., Suwargadi, B., Cheng, H., Edwards, R.L.,
2976 Avouac, J., and Ward, S.N., 2006, Source parameters of the great Sumatran megathrust
2977 earthquakes of 1797 and 1833 inferred from coral microatolls: Journal of Geophysical
2978 Research, v. 111, B06403, doi:10.1029/2005JB004025.
- 2979 Nelson, A.R., Kelsey, H.M., and Witter, R.C., 2006, Great earthquakes of variable magnitude at
2980 the Cascadia subduction zone: Quaternary Research, v. 65, p. 354–365,
2981 doi:10.1016/j.yqres.2006.02.009.
- 2982 Nelson, C.H., 1968, Marine geology of Astoria deep-sea fan [Ph.D. thesis]: Corvallis, Oregon
2983 State University, 289 p.

- 2984 Nelson, C.H., Kulm, L.D., Carlson, P.R., and Duncan, J.R., 1968, Mazama ash in the
2985 northeastern Pacific: *Science*, v. 161, p. 47–49, doi:10.1126/science.161.3836.47.
- 2986 Nelson, C.H., Meyer, A.W., Thor, D., and Larsen, M., 1986, Crater Lake, Oregon: A restricted
2987 basin with base-of-slope aprons of nonchanellized turbidites: *Geology*, v. 14, p. 238–241,
2988 doi:10.1130/0091-7613(1986)14<238:CLOARB>2.0.CO;2.
- 2989 Nelson, C.H., Pastor, J.G., Goldfinger, C., and Escutia, C., 2012, Great earthquakes along the
2990 western United States continental margin: Implications for hazards, stratigraphy and
2991 turbidite lithology: *Natural Hazards and Earth System Sciences*, v. 12, p. 3191–3208,
2992 doi:10.5194/nhess-12-3191-2012.
- 2993 Newcomb, K.R., and McCann, W.R., 1987, Seismic history and seismotectonics of the Sunda
2994 Arc: *Journal of Geophysical Research*, v. 92, p. 421–439, doi:10.1029/JB092iB01p00421.
- 2995 Newman, A.V., Hayes, G.P., Wei, Y., and Convers, J., 2011, The 25 October 2010 Mentawai
2996 tsunami earthquake, from real-time discriminants, finite-fault rupture, and tsunami
2997 excitation: *Geophysical Research Letters*, v. 38, L05302, doi:10.1029/2010GL046498.
- 2998 Ninis, D., Little, T.A., Van Dissen, R.J., Litchfield, N.J., Smith, E.G.C., Wang, N., Reiser, U.,
2999 and Henderson, C.M., 2013, Slip rate on the Wellington fault, New Zealand, during the late
3000 Quaternary: Evidence for variable slip during the Holocene: *Seismological Society of
3001 America Bulletin*, v. 103, p. 559–579, doi:10.1785/0120120162.
- 3002 Nittrouer, C.A., 1978, Detrital sediment accumulation in a continental shelf environment of the
3003 Washington shelf [Ph.D. thesis]: Seattle, University of Washington, 243 p.
- 3004 Noda, A., 2004, Turbidites along Kushiro Canyon, *in* Satake, K., and Goldfinger, C., eds.,
3005 Workshop on turbidites as earthquake recorders: Tsukuba, Geological Survey of Japan.

- 3006 Noda, A., Tuzino, T., Kanai, Y., Furukawa, R., and Uchida, J.-I., 2008, Paleoseismicity along the
3007 southern Kuril Trench deduced from submarine-fan turbidites: *Marine Geology*, v. 254,
3008 p. 73–90, doi:10.1016/j.margeo.2008.05.015.
- 3009 Noller, J.S., 2000, Lead-210 geochronology, *in* Noller, J.S., *et al.*, eds., *Quaternary*
3010  geochronology: American Geophysical Union Reference Shelf 4, p. 115–120.
- 3011 **[[Not cited? See query in the text.]]** Obermeier, S.F., and Dickenson, S.E., 2000, Liquefaction
3012 evidence for the strength of ground motions resulting from late Holocene Cascadia
3013 subduction earthquakes, with emphasis on the event of 1700 A.D: *Seismological Society of*
3014 *America Bulletin*, v. 90, p. 876–896, doi:10.1785/0119980179.
- 3015 O’Connor, S., Ulm, S., Fallon, S., Barham, A., and Loch, I., 2010, Pre-bomb marine reservoir
3016 variability in the Kimberley region, Western Australia: *Radiocarbon*, v. 52, p. 1158–1165.
- 3017 Park, J., *et al.*, 2005, Earth’s free oscillations excited by the 26 December 2004 Sumatra-
3018 Andaman earthquake: *Science*, v. 308, p. 1139–1144, doi:10.1126/science.1112305.
- 3019 Parsons, T., 2012, Paleoseismic interevent times interpreted for an unsegmented earthquake
3020 rupture forecast: *Geophysical Research Letters*, v. 39, L13302, doi:10.1029/2012GL052275.
- 3021 Parsons, T., Console, R., Falcone, G., Murru, M., *and* Yamashima, K., 2012, Comparison of
3022 characteristic and Gutenberg-Richter models for time-dependent $M \geq 7.9$ earthquake
3023 probability in the Nankai-Tokai subduction zone, Japan: *Geophysical Journal International*,
3024 v. 190, p. 1673–1688, doi:10.1111/j.1365-246X.2012.05595.x.
- 3025 Patton, J.R., Goldfinger, C., Djadjadihardja, Y., Udrek, and *Shipboard Scientific Party*, 2007,
3026 Roger Revelle Cruise RR0705 Superquakes07 Cruise Report: Oregon State University,
3027 Active Tectonics Laboratory; Agency for the Assessment and Application of Technology,
3028 Indonesia (BPPT), 66 p.


- 3029 Patton, J.R., Goldfinger, C., Morey, A., Romsos, C., Black, B., Djadjadihardja, Y., and Udrekh,
3030 2013a, Seismoturbidite record as preserved at core sites at the Cascadia and Sumatra-
3031 Andaman subduction zones: *Natural Hazards and Earth System Sciences*, v. 13, p. 833–867,
3032 doi:10.5194/nhess-13-833-2013.
- 3033 Patton, J.R., Goldfinger, C., Djadjadihardja, Y., and Udrekh, 2013b, Slope stability: Factor of
3034 safety along the seismically active continental slope offshore Sumatra: American
3035 Geophysical Union, fall meeting, abs. T23I–03.
- 3036 Peduzzi, P., Chatenoux, B., Dao, H., De Bono, A., Herold, C., Kossin, J., Mouton, F., and
3037 Nordbeck, O., 2012, Global trends in tropical cyclone risk: *Nature Climate Change*, v. 2,
3038 p. 289–294, doi:10.1038/nclimate1410.
- 3039 Peterson, C.D., and Madin, I.P., 1997, Coseismic paleoliquefaction evidence in the central
3040 Cascadia margin, USA: *Oregon Geology*, v. 59, p. 51–74.
- 3041 Philibosian, B., Sieh, K., Natawidjaja, D.H., Chiang, H., Shen, C., Suwargadi, B., Hill, E.M., and
3042 Edwards, R.L., 2012, An ancient shallow slip event on the Mentawai segment of the Sunda
3043 megathrust, Sumatra: *Journal of Geophysical Research*, v. 117, B05401,
3044 doi:10.1029/2011JB009075.
- 3045 Philibosian, B., Sieh, K., Avouac, J., Natawidjaja, D.H., Chiang, H., Wu, C., Perfettini, H., Shen,
3046 C., Daryono, M., and Suwargadi, B., 2014, Rupture and variable coupling behavior of the
3047 Mentawai segment of the Sunda megathrust during the supercycle culmination of 1797 to
3048 1833: *Journal of Geophysical Research*, v. 119, p. 7258–7287, doi:10.1002/2014JB011200.
- 3049 Piper, D.J.W., 1978, Turbidite muds and silts on deep-sea fans and abyssal plains, *in* Stanley,
3050 D.J., and Kelling, G., eds., *Sedimentation in submarine canyons, fans and trenches*:
3051 Stroudsburg, Pennsylvania, Dowden, Hutchinson & Ross, p. 163–176.

- 3052 Piper, D.J.W., Cochonat, P., and Morrison, M.L., 1999, The sequence of events around the
3053 epicentre of the 1929 Grand Banks earthquake: Initiation of debris flows and turbidity
3054 current inferred from sidescan sonar: *Sedimentology*, v. 46, p. 79–97, doi:10.1046/j.1365-
3055 3091.1999.00204.x.
- 3056 Polonia, A., Romano, S., Çağatay, M.N., Capotondi, L., Gasparotto, G., Gasperini, L., Panieri,
3057 G., and Torelli, L., 2015, Are repetitive slumpings during sapropel S1 related to paleo-
3058 earthquakes?: *Marine Geology*, v. 361, p. 41–52, doi:10.1016/j.margeo.2015.01.001.
- 3059 Polonia, A., Bonatti, E., Camerlenghi, A., Lucchi, R.G., Panieri, G., and Gasperini, L., 2013a,
3060 Mediterranean megaturbidite triggered by the AD 365 Crete earthquake and tsunami:
3061 *Scientific Reports*, v. 3, **1285**, doi:10.1038/srep01285.
- 3062 Polonia, A., Panieri, G., and Gasperini, L., 2013b, Turbidite paleoseismology in the Calabrian
3063 Arc subduction complex (Ionian Sea): *Geochemistry, Geophysics, Geosystems*, v. 14,
3064 p. 112–140, doi:10.1029/2012GC004402.
- 3065 Pouderoux, H., Proust, J.-N., Lamarche, G., Orpin, A., and Neil, H., 2012, Postglacial (after 18
3066 ka) deep-sea sedimentation along the Hikurangi subduction margin (New Zealand):
3067 Characterisation, timing and origin of turbidites: *Marine Geology*, v. 295–298, p. 51–76,
3068 doi:10.1016/j.margeo.2011.11.002.
- 3069 Prell, W.L., Imbrie, J., Martinson, D.G., Morley, J.J., Pisias, N.G., Shackleton, N.J., and Streeter,
3070 H.F., 1986, Graphic correlation of oxygen isotope stratigraphy application to the late
3071 Quaternary: *Paleoceanography*, v. 1, p. 137–162, doi:10.1029/PA001i002p00137.
- 3072 **[[Rajendran et al., 2006, is cited in Figure 11. Please provide full reference or delete from**
3073 **figure.]]** 

- 3074 Rajendran, C.P., Rajendran, K., Anu, R., Earnest, A., Machado, T., Mohan, P.M., and
3075 Freymueller, J., 2007, Crustal deformation and seismic history associated with the 2004
3076 Indian Ocean earthquake: A perspective from the Andaman–Nicobar Islands: *Seismological*
3077 *Society of America Bulletin*, v. 97, p. S174–S191, doi:10.1785/0120050630.
- 3078 Rajendran, K., Rajendran, C.P., Earnest, A., Ravi Prasad, G.V., Dutta, K., Ray, D.K., and Anu,
3079 R., 2008, Age estimates of coastal terraces in the Andaman and Nicobar Islands and their
3080 tectonic implications: *Tectonophysics*, v. 455, p. 53–60, doi:10.1016/j.tecto.2008.05.004.
- 3081 Rajendran, C.P., Rajendran, K., Andrade, V., and Srinivasalu, S., 2013, Ages and relative sizes
3082 of pre-2004 tsunamis in the Bay of Bengal inferred from geologic evidence in the Andaman
3083 and Nicobar Islands: *Journal of Geophysical Research*, v. 118, p. 1–18,
3084 doi:10.1029/2012JB009541.
- 3085 Rampino, M.R., 1984, Terrestrial mass extinctions, cometary impacts and the sun’s motion
3086 perpendicular to the galactic plane: *Nature*, v. 308, p. 709–712, doi:10.1038/308709a0.
- 3087 Rampino, M.R., 1999, Impact crises, mass extinctions, and galactic dynamics: The case for a
3088 unified theory, *in Dressler, B.O., and Sharpton, V.L., eds., Large meteorite impacts and*
3089 *planetary evolution; II*: Geological Society of America Special Paper 339, p. 241–248,
3090 doi:10.1130/0-8137-2339-6.241.
- 3091 Rampino, M.R., 2002, Role of the galaxy in periodic impacts and mass extinctions on the Earth,
3092 *in Koeberl, C., and MacLeod, K., eds., Catastrophic events and mass extinctions: Impacts*
3093 *and beyond*: Geological Society of America Special Paper 356, p. 667–678, doi:10.1130/0-
3094 8137-2356-6.667.
- 3095 Rampino, M.R., and Stothers, R.B., 1984, Geological rhythms and cometary impacts: *Science*, v.
3096 226, p. 1427–1431, doi:10.1126/science.226.4681.1427.

- 3097 Ratzov, G., Collot, J.-Y., Sosson, M., and Migeon, S., 2010, Mass-transport deposits in the
3098 northern Ecuador subduction trench: Result of frontal erosion over multiple seismic cycles:
3099 Earth and Planetary Science Letters, v. 296, p. 89–102, doi:10.1016/j.epsl.2010.04.048.
- 3100 Reimer, P.J., *et al.*, 2009, INTCAL09 and MARINE09 radiocarbon age calibration curves, 0–
3101 50,000 years cal BP: Radiocarbon, v. 51, p. 1111–1150,.
- 3102 Reimer, P.J., *et al.*, 2013, IntCal13 and Marine13 radiocarbon age calibration curves 0–50,000
3103 years cal BP: Radiocarbon, v. 55, p. 1869–1887, doi:10.2458/azu_js_rc.55.16947.
- 3104 Rhodes, B.P., Kirby, M.E., Jankaew, K., and Choowong, M., 2011, Evidence for a mid-Holocene
3105 tsunami deposit along the Andaman coast of Thailand preserved in a mangrove
3106 environment: Marine Geology, v. 282, p. 255–267, doi:10.1016/j.margeo.2011.03.003.
- 3107 Rivera, L., Sieh, K., Helmberger, D., *and* Natawidjaja, D.H., 2002, A comparative study of the
3108 Sumatran subduction-zone earthquakes of 1935 and 1984: Seismological Society of
3109 America Bulletin, v. 92, p. 1721–1736, doi:10.1785/0120010106.
- 3110 Robbins, J.A., Edgington, D.N., and Kemp, A.L.W., 1978, Comparative ^{210}Pb , ^{137}Cs , and pollen
3111 geochronologies of sediments from Lakes Ontario and Erie: Quaternary Research, v. 10,
3112 p. 256–278, doi:10.1016/0033-5894(78)90105-9.
- 3113 Robison, W.L., Conrado, C.L., Bogen, K.T., and Stoker, A.C., 2003, The effective and
3114 environmental half-life of ^{137}Cs at Coral Islands at the former US nuclear test site: Journal of
3115 Environmental Radioactivity, v. 69, p. 207–223, doi:10.1016/S0265-931X(03)00080-8.
- 3116 Rong, Y., Jackson, D.D., Magistrale, H., and Goldfinger, C., 2014, Magnitude limits of
3117 subduction zone earthquakes: Seismological Society of America Bulletin, v. 104, p. 2359–
3118 2377, doi:10.1785/0120130287.


- 3119 Ross, D.A., 1971, Mass physical properties and slope stability of sediments of the northern
3120 Middle America Trench: *Journal of Geophysical Research*, v. 76, p. 704–712,
3121 doi:10.1029/JC076i003p00704.
- 3122 Ruff, L., and Kanamori, H., 1980, Seismicity and the subduction process: *Physics of the Earth
3123 and Planetary Interiors*, v. 23, p. 240–252, doi:10.1016/0031-9201(80)90117-X.
- 3124 Salisbury, M., Kent, A., Patton, J., Goldfinger, C., Djadjadihardja, Y., and Udrek, U., 2010,
3125 Deep-sea ash layers reveal evidence of large Pleistocene and Holocene volcanic eruptions
3126 from Sumatra, Indonesia: *American Geophysical Union*, fall meeting, abs. V11D–2330.
- 3127 Salisbury, M., Patton, J., Kent, A., Goldfinger, C., Djadjadihardja, Y., and Udrek, U., 2012,
3128 Newly discovered deep-sea ash layers reveal evidence of large Holocene volcanic eruptions
3129 from Sumatra, Indonesia: *Journal of Volcanology and Geothermal Research*, v. 231–232,
3130 p. 61–71, doi:10.1016/j.jvolgeores.2012.03.007.
- 3131 Sari, E., and Çağatay, M., 2006, Turbidites and their association with past earthquakes in the
3132 deep Çınarcık Basin of the Marmara Sea: *Geo-Marine Letters*, v. 26, p. 69–76,
3133 doi:10.1007/s00367-006-0017-3.
- 3134 Satake, K., and Atwater, B., 2007, Long-term perspectives on giant earthquakes and tsunamis at
3135 subduction zones: *Annual Review of Earth and Planetary Sciences*, v. 35, p. 349–374,
3136 doi:10.1146/annurev.earth.35.031306.140302.
- 3137 Sayles, F.L., Martin, W.R., and Deuser, W.G., 1994, Response of benthic oxygen demand to
3138 particulate organic carbon supply in the deep sea near Bermuda: *Nature*, v. 371, p. 686–689,
3139 doi:10.1038/371686a0.
- 3140 Sayles, F.L., Martin, W.R., Chase, Z., and Anderson, R.F., 2001, Benthic remineralization and
3141 burial of biogenic SiO₂, CaCO₃, organic carbon, and detrital material in the Southern Ocean

- 3142 along a transect at 170° west: *Deep-Sea Research, Part II, Topical Studies in Oceanography*,
3143 v. 48, p. 4323–4383, doi:10.1016/S0967-0645(01)00091-1.
- 3144 Schlagenhauf, A., Manighetti, I., Benedetti, L., Gaudemer, Y., Finkel, R., Malavieille, J., and
3145 Pou, K., 2011, Earthquake supercycles in central Italy, inferred from ^{36}Cl exposure dating:
3146 *Earth and Planetary Science Letters*, v. 307, p. 487–500, doi:10.1016/j.epsl.2011.05.022.
- 3147 Schulz, W.H., Galloway, S.L., and Higgins, J.D., 2012, Evidence for earthquake triggering of
3148 large landslides in coastal Oregon, USA: *Geomorphology*, v. 141–142, p. 88–98,
3149 doi:10.1016/j.geomorph.2011.12.026.
- 3150 Schurr, B., Asch, G., Rosenau, M., Wang, R., Oncken, O., Barrientos, D.E., Salazar, P., and
3151 Vilotte, J.P., 2007, The 2007 M7.7 Tocopilla northern Chile earthquake sequence:
3152 Implications for along-strike and downdip rupture segmentation and megathrust frictional
3153  behavior: *Journal of Geophysical Research*, v. 117, B05305, doi:10.1029/2011JB009030.
- 3154 **[[Not cited? See query in text.]]** Scott, E.M., 2003, The Fourth International Radiocarbon
3155 Intercomparison (FIRI): *Radiocarbon*, v. 45, p. 135–285.
- 3156 Seilacher, A., 1969, Fault-graded beds interpreted as seismites: *Sedimentology*, v. 13, p. 155–
3157 159, doi:10.1111/j.1365-3091.1969.tb01125.x.
- 3158 Shanmugam, G., 2008, The constructive functions of tropical cyclones and tsunamis on deep-
3159 water sand deposition during sea level highstand: Implications for petroleum exploration:
3160 *American Association of Petroleum Geologists Bulletin*, v. 92, p. 443–471,
3161 doi:10.1306/12270707101.
- 3162 Shiki, T., 1996, Reading of the trigger records of sedimentary events—A problem for future
3163 studies: *Sedimentary Geology*, v. 104, p. 249–255, doi:10.1016/0037-0738(95)00132-8.

- 3164 Shiki, T., Kumon, F., Inouchi, Y., Kontani, Y., Sakamoto, T., Tateishi, M., Matsubara, H., and
3165 Fukuyama, K., 2000, Sedimentary features of the seismo-turbidites, Lake Biwa, Japan:
3166 *Sedimentary Geology*, v. 135, p. 37–50, doi:10.1016/S0037-0738(00)00061-0.
- 3167 Shimazaki, K., and Nakata, T., 1980, Time-predictable recurrence model for large earthquakes:
3168 *Geophysical Research Letters*, v. 7, p. 279–282, doi:10.1029/GL007i004p00279.
- 3169 Shirai, M., Omura, A., Wakabayashi, T., Uchida, J.-i., and Ogami, T., 2010, Depositional age
3170 and triggering event of turbidites in the western Kumano Trough, central Japan during the
3171 last ca. 100 years: *Marine Geology*, v. 271, p. 225–235, doi:10.1016/j.margeo.2010.02.015.
- 3172 Sieh, K., and Natawidjaja, D., 2000, Neotectonics of the Sumatran fault: *Journal of Geophysical*
3173 *Research*, v. 105, no. B12, p. 28,295–28,326, doi:10.1029/2000JB900120.
- 3174 Sieh, K., Natawidjaja, D.H., Meltzner, A.J., Shen, C., Cheng, H., Li, K., Suwargadi, B.W.,
3175 Galetzka, J., Philibosian, B., and Edwards, R.L., 2008, Earthquake supercycles inferred from
3176 sea-level changes recorded in the corals of West Sumatra: *Science*, v. 322, p. 1674–1678,
3177 doi:10.1126/science.1163589.
- 3178 Smith, K.L., 1987, Food energy supply and demand: A discrepancy between particulate organic
3179 carbon flux and sediment community oxygen consumption in the deep ocean: *Limnology*
3180 *and Oceanography*, v. 32, p. 201–220, doi:10.4319/lo.1987.32.1.0201.
- 3181 Smith, S., Karlin, R.E., Kent, G.M., Seitz, G.G., and Driscoll, N.W., 2013, Holocene subaqueous
3182 paleoseismology of Lake Tahoe: *Geological Society of America Bulletin*, v. 125,
3183 p. 691–708, doi:10.1130/B30629.1.
- 3184 Smith, W.H.F., and Sandwell, D.T., 1997, Global seafloor topography from satellite altimetry
3185 and ship depth soundings: *Science*, v. 277, p. 1956–1962,
3186 doi:10.1126/science.277.5334.1956.

- 3187 Song, T.-R.A., and Simons, M., 2003, Large trench-parallel gravity variations predict
3188 seismogenic behavior in subduction zones: *Science*, v. 301, p. 630–633,
3189 doi:10.1126/science.1085557.
- 3190 Sorensen, M.B., Atakan, K., and Pulido, N., 2007, Simulated strong ground motions for the great
3191 M 9.3 Sumatra–Andaman earthquake of 26 December 2004: *Seismological Society of
3192 America Bulletin*, v. 97, p. S139–S151, doi:10.1785/0120050608.
- 3193 Southon, J., Kashgarian, M., Fontugne, M., Metivier, B., and Yim, W.W.-S., 2002, Marine
3194 reservoir corrections for the Indian Ocean and Southeast Asia: *Radiocarbon*, v. 44, p. 167–
3195 180.
- 3196 Squire, P., Joannes-Boyau, R., Scheffers, A.M., Nothdurft, L.D., Hua, Q., Collins, L.B.,
3197 Scheffers, S.R., and Zhao, J., 2013, A marine reservoir correction for the Houtman-Abrolhos
3198 Archipelago, East Indian Ocean, Western Australia: *Radiocarbon*, v. 55, p. 103–114,
3199 doi:10.2458/azu_js_rc.v55i1.16197.
- 3200 Stein, S., and Okal, E., 2007, Ultralong period seismic study of the December 2004 Indian Ocean
3201 earthquake and implications for regional tectonics and the subduction process:
3202 *Seismological Society of America Bulletin*, v. 97, p. S279–S295, doi:10.1785/0120050617.
- 3203 St-Onge, G., Mulder, T., Piper, D.J.W., Hillaire-Marcel, C., and Stoner, J.S., 2004, Earthquake
3204 and flood-induced turbidites in the Saguenay Fjord (Québec): A Holocene paleoseismicity
3205 record: *Quaternary Science Reviews*, v. 23, p. 283–294,
3206 doi:10.1016/j.quascirev.2003.03.001.
- 3207 St-Onge, G., et al., 2012, Comparison of earthquake-triggered turbidites from the Saguenay
3208 (eastern Canada) and Reloncavi (Chilean margin) fjords: Implications for paleoseismicity

- 3209 and sedimentology: *Sedimentary Geology*, v. 243–244, p. 89–107,
3210 doi:10.1016/j.sedgeo.2011.11.003.
- 3211 Stow, D.A.V., 1977, Late Quaternary stratigraphy and sedimentation on the Nova Scotian outer
3212 continental margin [Ph.D. thesis]: Halifax, Nova Scotia, Dalhousie University, 360 p.
- 3213 Stow, D.A.V., 1985, Deep-sea clastics: Where are we and where are we going?, *in* **Brenchley,**
3214 **P.J., and Williams, B.P.J., eds., *Sedimentology recent developments and applied aspects:***
3215 **Geological Society of London Special Publication 18**, p. 67–93,
3216 doi:10.1144/GSL.SP.1985.018.01.05.
- 3217 Stow, D.A.V., and Bowen, A.J., 1980, A physical model for the transport and sorting of fine-
3218 grained sediment by turbidity currents: *Sedimentology*, v. 27, p. 31–46, doi:10.1111/j.1365-
3219 3091.1980.tb01156.x.
- 3220 Stow, D.A.V., and Piper, D.J.W., 1984, Deep-water fine-grained sediments: Facies models, *in*
3221 Stow, D.A.V., and Piper, D.J.W., eds., *Fine-grained sediments: Deep-water processes and*
3222 *facies: Geological Society of London Special Publication 15*, p. 611–646,
3223 doi:10.1144/GSL.SP.1984.015.01.38.
- 3224 Stow, D.A.V., **Amano, K., Balson, P.S., Brass, G.W., Corrigan, J., Raman, C.V., Tiercelin, J.-J.,**
3225 **Townsend, M., and Wijayananda, N.P.,** 1990, Sediment facies and processes on the distal
3226 Bengal Fan, Leg 116, *in* **Cochran, J.R., et al., *Proceedings of the Ocean Drilling Program,***
3227 ***Scientific results, Volume 116: College Station, Texas, Ocean Drilling Program***, p. 377–396,
3228 doi:10.2973/odp.proc.sr.116.110.1990.
- 3229 Stuiver, M., and Braziunas, T.F., 1993, Modeling atmospheric ^{14}C influences and ^{14}C ages of
3230 marine samples to 10,000 BC: *Radiocarbon*, v. 35, p. 137–189.

- 3231 Stuiver, M., and Polach, H.A., 1977, Discussion: Reporting of ^{14}C data: *Radiocarbon*, v. 19,
3232 p. 355–363.
- 3233 Stuiver, M., Reimer, P.J., and Braziunas, T.F., 1998, High precision radiocarbon age calibration
3234 for terrestrial and marine samples: *Radiocarbon*, v. 40, p. 1127–1151.
- 3235 Subarya, C., Chlieh, M., Prawirodirdjo, L., Avouac, J., Bock, Y., Sieh, K., Meltzner, A.J.,
3236 Natawidjaja, D.H., and McCaffrey, R., 2006, Plate-boundary deformation associated with
3237 the great Sumatra–Andaman earthquake: *Nature*, v. 440, p. 46–51, doi:10.1038/nature04522.
- 3238 Sultan, N., *et al.*, 2004, Triggering mechanisms of slope instability processes and sediment
3239 failures on continental margins: A geotechnical approach: *Marine Geology*, v. 213, p. 291–
3240 321, doi:10.1016/j.margeo.2004.10.011.
- 3241 Sultan, N., Cattaneo, A., Sibuet, J.-C., and Schneider, J.-L., 2009, Deep sea in situ excess pore
3242 pressure and sediment deformation off NW Sumatra and its relation with the December 26,
3243 2004 Great Sumatra–Andaman earthquake: *International Journal of Earth Sciences*, v. 98,
3244 p. 823–837, doi:10.1007/s00531-008-0334-z.
- 3245 Sumner, E., Siti, M., McNeil, L.C., Talling, P.J., Henstock, T., Wynn, R., Djadjadihardja, Y.,
3246 and Permana, H., 2013, Can turbidites be used to reconstruct a paleoearthquake record for
3247 the central Sumatran margin?: *Geology*, v. 41, p. 763–766, doi:10.1130/G34298.1.
- 3248 Susilohadi, S., Gaedickea, C., and Ehrhardt, A., 2005, Neogene structures and sedimentation
3249 history along the Sunda forearc basins off southwest Sumatra and southwest Java: *Marine*
3250  *Geology*, v. 219, p. 133–154, doi:10.1016/j.margeo.2005.05.001.
- 3251 **[[Not cited? See query in text.]]** Syvitski, J.P.M., and Schafer, C.T., 1996, Evidence for an
3252 earthquake-triggered basin collapse in Saguenay Fjord, Canada: *Sedimentary Geology*,
3253 v. 104, p. 127–153, doi:10.1016/0037-0738(95)00125-5.

- 3254 Talling, P.J., 2014, On the triggers, resulting flow types and frequencies of subaqueous sediment
3255 density flows in different settings: *Marine Geology*, v. 352, p. 155–182,
3256 doi:10.1016/j.margeo.2014.02.006.
- 3257 Tanioka, Y., and Ruff, L.J., 1997, Source time functions: *Seismological Research Letters*, v. 68,
3258 p. 386–400, doi:10.1785/gssrl.68.3.386.
- 3259 Tearpock, D.J., and Bischke, R.E., 2002, *Applied subsurface geological mapping*: Englewood
3260 Cliffs, New Jersey, Prentice-Hall, Inc., 864 p.
- 3261 Thompson, R., and Morton, D.J., 1979, Magnetic susceptibility and particle-size distribution in
3262 recent sediments of the Loch Lomond drainage basin, Scotland: *Journal of Sedimentary*
3263 *Petrology*, v. 49, p. 801–812, doi:10.1306/212F7851-2B24-11D7-8648000102C1865D.
- 3264 Thomson, R.E., Davis, E.E., Heesemann, M., and Villinger, H., 2010, Observations of long-
3265 duration episodic bottom currents in the Middle America Trench: Evidence for tidally
3266 initiated turbidity flows: *Journal of Geophysical Research*, v. 115, C10020,
3267 doi:10.1029/2010JC006166.
- 3268 Tolstoy, M., and Bohnenstiehl, D.R., 2006, Hydroacoustic contributions to understanding the
3269 December 26th 2004 great Sumatra–Andaman earthquake: *Surveys in Geophysics*, v. 27,
3270 p. 633–646, doi:10.1007/s10712-006-9003-6.
- 3271 Travasarou, T., Bray, J.D., and Abrahamson, N.A., 2003, Empirical attenuation relationship for
3272 Arias intensity: *Earthquake Engineering and Structural Dynamics*, v. 32, p. 1133–1155,
3273 doi:10.1002/eqe.270.
- 3274 Underwood, M.B., Hoke, K.D., Fisher, A.T., Davis, E.E., Giambalvo, E., Hlsdorff, L.Z., and
3275 Spinelli, G.A., 2005, Provenance, stratigraphic architecture, and hydrogeologic influence of

- 3276 turbidites on the mid-ocean ridge flank of northwestern Cascadia Basin, Pacific Ocean:
3277 Journal of Sedimentary Research, v. 75, p. 149–164, doi:10.2110/jsr.2005.012.
- 3278 Van Daele, M., Gnudde, V., Duyck, P., Pino, M., Urrutia, R., and De Batist, M., 2014,
3279 Multidirectional, synchronously-triggered seismo-turbidites and debrites revealed by X-ray
3280 computed tomography (CT): Sedimentology, v. 61, p. 861–880, doi:10.1111/sed.12070.
- 3281 Van Daele, M., Moernaut, J., Doom, L., Boes, R., Hebbeln, D., Pino, M., Urrutia, R., Brümmer,
3282 R., and De Batist, M., 2015, A comparison of the sedimentary records of the 1960 and 2010
3283 great Chilean earthquakes in 17 lakes: Implications for quantitative lacustrine
3284 palaeoseismology: Sedimentology, doi:10.1111/sed.12193.
- 3285 van der Lingen, G.J., 1969, The turbidite problem: New Zealand Journal of Geology and
3286 Geophysics, v. 12, p. 7–50, doi:10.1080/00288306.1969.10420225.
- 3287 Völker, D., Reichel, T., Wiedicke, M., and Heubeck, C., 2008, Turbidites deposited on Southern
3288 Central Chilean seamounts: Evidence for energetic turbidity currents: Marine Geology,
3289 v. 251, p. 15–31, doi:10.1016/j.margeo.2008.01.008.
- 3290 Waldmann, N., Anselmetti, F.S., Ariztegui, D., Austin, J.A., Jr., Pirouz, M., Moy, C.M., and
3291 Dunbar, R.B., 2011, Holocene mass-wasting events in Lago Fagnano, Tierra del Fuego
3292 (54°S): Implications for paleoseismicity of the Magallanes-Fagnano transform fault: Basin
3293 Research, v. 23, p. 171–190, doi:10.1111/j.1365-2117.2010.00489.x.
- 3294 Wang, X., and Liu, P.L., 2006, An analysis of 2004 Sumatra earthquake fault plane mechanisms
3295 and Indian Ocean tsunami: Journal of Hydraulic Research, v. 44, p. 147–154,
3296 doi:10.1080/00221686.2006.9521671.
- 3297 Ward, S.N., 2002, Planetary cratering: A probabilistic approach: Journal of Geophysical
3298 Research, v. 107, p. 7-1–7-11, doi:10.1029/2000JE001343.

- 3299 Weiss, R., 2008, Sediment grains moved by passing tsunami waves: Tsunami deposits in deep
3300 water: *Marine Geology*, v. 250, p. 251–257, doi:10.1016/j.margeo.2008.01.018.
- 3301 Wells, R.E., Blakely, R.J., Sugiyama, Y., Scholl, D.W., and Dinterman, P.A., 2003, Basin-
3302 centered asperities in great subduction zone earthquakes: A link between slip, subsidence,
3303 and subduction erosion: *Journal of Geophysical Research*, v. 108, 2507,
3304 doi:10.1029/2002JB002072.
- 3305 Wesnousky, S.G., 1994, The Gutenberg-Richter or characteristic earthquake distribution, which
3306 is it?: *Seismological Society of America Bulletin*, v. 84, p. 1940–1959.
- 3307 **[[Not cited?]]**Wesnousky, S.G., 2008, Displacement and geometrical characteristics of
3308 earthquake surface ruptures: Issues and implications for seismic-hazard analysis and the
3309 process of earthquake rupture: *Seismological Society of America Bulletin*, v. 98, p. 1609–
3310 1632.
- 3311 Wheatcroft, R.A., and Sommerfield, C.K., 2005, River sediment flux and shelf accumulation
3312 rates on the Pacific Northwest margin: *Continental Shelf Research*, v. 25, p. 311–332,
3313 doi:10.1016/j.csr.2004.10.001.
- 3314 Wilson, C., and Keefer, D.K., 1985, Predicting areal limits of earthquake-induced landsliding, *in*
3315 **Ziony, J.I., ed., *Evaluating earthquake hazards in the Los Angeles region; an earth-science***
3316 ***perspective*: U.S. Geological Survey Professional Paper 1360, p. 317–345.**
- 3317 Wilson, R.C., 1993, Relation of Arias intensity to magnitude and distance in California: U.S.
3318 **Geological Survey** Open-File Report 93-556, 45 p.
- 3319 Wilson, T.R.S., Thomson, J., Colley, S., Hydes, D.J., Higgs, N.C., and Sørensen, J., 1985, Early
3320 organic diagenesis: The significance of progressive subsurface oxidation fronts in pelagic

- 3321 sediments: *Geochimica et Cosmochimica Acta*, v. 49, p. 811–822, doi:10.1016/0016-
- 3322 7037(85)90174-7.
- 3323 Wiseman, K., and Bürgmann, R., 2011, Stress and seismicity changes on the Sunda megathrust
- 3324 preceding the 2007 Mw 8.4 earthquake: *Seismological Society of America Bulletin*, v. 101,
- 3325 p. 313–326, doi:10.1785/0120100063.
- 3326 Witter, R.C., Zhang, Y., Wang, K., Priest, G.R., Goldfinger, C., Stimely, L.L., English, J.T., and
- 3327 Ferro, P.A., 2011, Simulating tsunami inundation at Bandon, Coos County, Oregon, using
- 3328 hypothetical Cascadia and Alaska earthquake scenarios: *Oregon Department of Geology and*
- 3329 *Mineral Industries Special Paper 43*, 63 p.
- 3330 Witter, R.C., Zhang, Y.J., Wang, K., Priest, G., Goldfinger, C., Stimely, L., English, J., and
- 3331 Ferro, P., 2013, Simulated tsunami inundation for a range of Cascadia megathrust
- 3332 earthquake scenarios at Bandon, Oregon, USA: *Geosphere*, v. 9, p. 1783–1803,
- 3333 doi:10.1130/GES00899.1.
- 3334 Young, I.R., 1999, Seasonal variability of the global ocean wind and wave climate: *International*
- 3335 *Journal of Climatology*, v. 19, p. 931–950, doi:10.1002/(SICI)1097-
- 3336 0088(199907)19:9<931::AID-JOC412>3.0.CO;2-O.
- 3337 Youngs, R.R., Chiou, S.J., Silva, W.J., and Humphrey, J.R., 1997, Strong ground motion
- 3338 attenuation relationships for subduction zone earthquakes: *Seismological Research Letters*,
- 3339 v. 68, p. 58–73, doi:10.1785/gssrl.68.1.58.
- 3340 Yu, K., Hua, Q., Zhao, J.-X., Hodge, E., Fink, D., and Barbetti, M., 2010, Holocene marine ¹⁴C
- 3341 reservoir age variability: Evidence from ²³⁰Th-dated corals from South China Sea:
- 3342 *Paleoceanography*, v. 25, PA3205, doi:10.1029/2009PA001831.

3343 Zdanowicz, C.M., Zielinski, G.A., and Germani, M.S., 1999, Mount Mazama eruption:
 3344 Calendrical age verified and atmospheric impact assessed: *Geology*, v. 27, p. 621–624,
 3345  doi:10.1130/0091-7613(1999)027<0621:MMECAV>2.3.CO;2.

3346 **[[Not cited? See query in text.]]** Zhao, J.X., and Xu, H., 2012, Magnitude-scaling rate in
 3347 ground-motion prediction equations for response spectra from large subduction interface
 3348 earthquakes in Japan: *Seismological Society of America Bulletin*, v. 102, p. 222–235,
 3349 doi:10.1785/0120110154.

3350


3351 Figure 1. Plate tectonic setting. Compiled multiband single beam bathymetry and Shuttle Radar
 3352 Topography Mission topography is in shaded relief and colored versus depth (Smith and
 3353 Sandwell, 1997; Graindorge et al., 2008; Ladage et al., 2006). The India-Australia plate subducts
 3354  northeastward beneath the Sunda plate (part of Eurasia; sz—subduction zone). **[[correct?]]**
 3355 Orange vectors plot India plate movement relative (rel.) to Sunda, and black vectors plot
 3356 Australia relative to Sunda (global positioning system velocity based on Nuvel-1A; Bock et al.,
 3357 2003; Subarya et al., 2006). Historic ruptures (Bilham, 2005; Malik et al., 2011) are plotted in
 3358 gray, calendar years are in white. The 2004 and 2005 slip contours are shown in orange and
 3359 green, respectively (Chlieh et al., 2007, fig. 11 therein; Chlieh et al., 2008, fig. 20 therein).
 3360 Paleotsunami and paleoearthquake sites (lowercase letters) are plotted in green and purple,
 3361 respectively: a, b—Rajendran et al. (2007), c—Grand-Pre et al. (2008), d—Monecke et al.
 3362 (2008), e—Meltzner et al. (2010, 2012), f—Jankaew et al. (2008), g—Rajendran et al. (2008),
 3363 h—Nair et al. (2010), —Rhodes et al. (2011), j—Malik et al., (2011), k—Philibosian et al.,
 3364 (2012). RR0705 cores are plotted in orange, SO-002 cores are plotted  yellow (Sumner et al.,
 3365 2013). Black rectangle indicates locations of Figure 3 and Supplemental File S2. Bengal and

3366 Nicobar fans cover structures of the India-Australia plate in the northern part of the map; are
 3367 **dashed black** lines delimit their southern boundaries (Stow et al., 1990). The 2004 and 2005
 3368 earthquake focal mechanisms are plotted.

3369

3370 Figure 2. Core geophysical data are compared with particle size data. Plots are RGB (**red-green-**
 3371 **blue**) imagery, CT (**ct, computed tomographic X-ray**) imagery, gamma density (g/cm^3 , light
 3372 blue), CT density (dn, image digital number, 0–255, dark blue), point magnetic susceptibility
 3373 (**pms**, $\text{Si} \times 10^{-5}$, dark red), loop point magnetic susceptibility (**lms**, $\text{Si} \times 10^{-5}$, light red), mean,
 3374 median, mode, and d10 particle size (μm , green; 90% of particles are larger than this size) on a
 3375 logarithmic scale, and resistivity (Ohm, brown). **(A) Core 96PC. (B) Core 55PC.** Gray rectangles
 3376 denote the three major peaks in the core geophysical data. **[[“All core geophysical data in**
 3377 **subsequent figures are shown with same colors and units.” Deleted; each figure should**
 3378 **reference Fig. 2 caption separately, if necessary; note that uppercase letters used in text for**
 3379 **e.g., CT, but are lowercase in figures]]**

3380

3381 Figure 3. Regional core sites, source areas, and key core stratigraphy. **(A)** Core locations (orange
 3382 dots) on bathymetric map; key channel flow paths (light blue) to eight core sites **are shown**.
 3383 Slope basin and trench source areas (orange) were determined by outlining drainage divides
 3384 surrounding all submarine topography contributing potential gravity flows to a given core site.
 3385 While the region that drains to core 104PC then drains to the trench, the three other slope basins
 3386 are enclosed (they do not drain to the trench). **(B)** Flow path profile depth (km) versus forearc
 3387 distance (km) is plotted in brown for basin  w paths and blue for trench flow paths. **(C)** Shaded
 3388 relief map showing core sites **108** and **107** **[[No PC, TC, etc. letter labels for the cores?]]** as

3389 orange dots. Cores are labeled with their core number and the seawater depth at the core sites in
 3390 meters. Depth contours are in meters. An intermediate contour of 50 m depicts the shape of the
 3391 low-relief basin floor where core 108 is located. (D) Core sites 103 and 104 are plotted as orange
 3392 dots, with the core depth in meters. Intermediate contours of 3475 m and 3080 m depict the
 3393 shape of the basins. (E) Core 105 is plotted with the core depth in meters. (F) Core 98 is plotted
 3394 with the core depth in meters. (G) Core 94 is plotted with the core depth in meters. (H) Five
 3395 principle cores that we use in our correlations and age models are plotted versus depth in cm.
 3396 **Multisensor core logging** geophysical data are plotted [gamma density, CT (computed
 3397 tomographic X-ray) density, point magnetic susceptibility (Mag Sus), from left to right] and CT
 3398 imagery displays lower density material in darker gray and higher density material in lighter
 3399 gray. Slope cores are labeled in light blue; trench cores are labeled in dark blue. ¹⁴C ages are
 3400 reported in calendar (cal) yr B.P. (A.D. 1950). Gray rectangles refer to Figure 8. **[[4 digit**
 3401 **numbers should not have commas; in Fig. H, all abbreviations in legend should be spelled**
 3402 **out in caption. (e.g., “Br. Lam.” Brown laminations, laminae?) 14 in ¹⁴C should be**
 3403 **superscript; yrs should be yr; “g/cc” should be g/cm³ or g cm⁻³.]]**

3404
 3405 Figure 4. Turbidite division classification. (A) Bouma (1962) and van der Lingen (1969)
 3406 turbidite structure classification for fine grained turbidites is shown at left. Divisions are
 3407 designated by letters A–F, typically designated with a preceding T. Stow (1977) and Piper (1978)
 3408 turbidite structure classification system for fine-grained turbidites is shown at right. Piper (1978)
 3409 divisions are designated by E and F. Stow (1977) divisions are designated with T-. Both Stow
 3410 and Piper divisions fit within the Bouma Te division. (B) Turbidites in cores 96PC and 108PC
 3411 are plotted with turbidite division systems in displayed in A. Plotted from left to right are gamma




3412 density, CT (**computed tomographic X-ray**) density, lithologic log (pattern), CT imagery,
 3413 turbidite division, core depth (cm), lithologic log (grayscale texture), texture (particle size phi
 3414 scale including, from left to right, clay, silt, very fine sand, fine sand, medium sand, coarse sand,
 3415 very coarse sand, and gravel), and point magnetic susceptibility (**Mag. Sus.**). The deposit type
 3416 (single pulse or multipulse) and turbidite structure divisions present (included divisions) **are**
 3417 listed for each turbidite. **[[“g/cc” should be g/cm³.]]**


3418





3419 Figure 5. The uppermost (2004?) turbidite from **site RR0705** cores 96PC and 96TC, plotted as a
 3420 composite core. **(A)** From left to right: mean particle size, point magnetic susceptibility, CT
 3421 (**computed tomographic X-ray**) density, gamma density, turbidite classification, RGB (**red-green-**
 3422 **blue**) imagery, CT imagery, turbidite structure classification division, depth (cm), turbidite
 3423 structure (lithologic log), texture, and the lithologic notes are plotted versus depth. Geophysical
 3424 log symbols **and grain sizes as** in Figure 2. **(B)** Detailed turbidite structure based on CT imagery.
 3425 From left to right: i—CT imagery uninterpreted, ii—CT imagery interpreted, iii—turbidite
 3426 structure interpretation, iv—turbidite structure division classification, and v—turbidite structure
 3427 description. **[[what is “U.F.” abbreviation? Should spell out in caption or in figure]]** **(C)**



3428 Results from smear slide based vertical biostratigraphic transects for core 96PC. Percent
 3429 biogenic (**bio**) and percent lithologic (**lith**) are plotted versus depth (in m). **(D)** The mean,
 3430 minimum, and maximum particle size distribution for sediments collected within the uppermost
 3431 turbidite (in purple) and within hemipelagic sediments underlying the uppermost turbidite (in
 3432 green) are plotted. These are compared with the combined distributions (in blue). **(E)** Core 96PC
 3433 is plotted versus depth (in cm), from left to right: gamma density, CT density, turbidite criteria,
 3434 turbidite classification, uninterpreted imagery, interpreted imagery, depth (cm), turbidite

3435 structure, and texture. Each criterion met is listed for each turbidite (numbered 1–7). The
 3436 locations for where, in the core, these criteria are  are labeled and designated by color (see
 3437 legend; criteria are listed and described in the text). **[[Note that all abbreviations in figure E
 3438 (need uppercase label for figure) should be spelled out in figure or caption (IB, EB, VHS,
 3439 UBOL, GPR, SLS). In legend, abbreviations should be spelled out; hyphenation in A is
 3440 inconsistent (e.g., greenish-gray just above greenish gray; no hyphen in sub prefix)]]**

3441 


3442 Figure 6. (A) Core sites 96 and 95 **[[no letter (PC, TC) labels?]]** are plotted as orange dots, with
 3443 the seawater depths (–3400 and –3420 m respectively). Depth contours are in meters.
 3444 Intermediate contours of –3360 m and –3340 m depict the shape of the basins. The CHIRP
 3445 (compressed high-intensity  pulse) seismic profile track line is plotted on the map as a
 3446 yellow line crossing the core  core site. (B) The CHIRP seismic profile crossing the basin at
 3447 core . The core length of 96PC-96TC is plotted in dark brown. The depth for turbidite T-18 is
 3448 plotted as a light brown vertical line (discussed in text). The turbidite boundary interpreted in
 3449 seismic data is overlain in transparent brown. Southeast-northeast profile transect has an
 3450 orientation of N45E. The lighter brown line and lighter brown polygon designates a possible
 3451 thick turbidite (T-18), the uppermost tail of which is at the base of core 96PC. **[[numbers should
 3452 not have commas]]** 

3453

3454 Figure 7. Radiometric ages of the uppermost turbidite. Several examples of the likely 2004 and
 3455 2005 deposits are presented. (A) Lithologic details and ^{210}Pb analytical results are plotted for
 3456 cores 94PC, 105TC, 96PC, 96TC, 102MC, and 90MC. Data for ^{210}Pb decay per minute are
 3457 plotted versus depth with blue dots, alongside core data. Regressions are plotted for the cores


3458 that have depth-continuous samples. Core data include core depth (cm), CT (computed
 3459 tomographic X-ray) imagery, turbidite structure, and sedimentary texture (see Fig. 2 caption).
 3460 The ^{14}C ages are listed in calendar yr B.P. (A.D. 1950) with 95.4% uncertainty.
 3461 Calibrated, Sequence, and P_Sequence ages are presented as discussed in the text (Table 3). The
 3462 ^{14}C sample locations are outlined in dashed red lines. (B) Map showing the cores that contain a
 3463 deposit that may have resulted following the 2004 Sumatra-Andaman subduction zone
 3464 earthquake. Cores with a possible 2004 seismoturbidite are plotted in light orange. Core 90MC,
 3465 with a possible 2005 seismoturbidite, is plotted in dark orange. Other RR0705 cores are plotted
 3466 in yellow and SO002 cores are plotted in pink. **[[numbers should not have commas; need
 3467 space before km, m]]**

3468
 3469 Figure 8. Regional stratigraphic correlations. Stratigraphic correlations between key cores use
 3470 lithology, CT (computed tomographic X-ray), core geophysical properties (see Fig. 2 caption),
 3471 and ^{14}C data. Multisensor core logging (MSCL) data are plotted as in previous figures. CT
 3472 imagery displays lower density material in darker gray and higher density material in lighter
 3473 gray. Slope cores are in light blue; trench cores are in dark blue. The ^{14}C ages are reported in
 3474 calendar (cal) yr B.P. (A.D. 1950). Green correlation tie lines designate correlation confidence
 3475 with line thickness and pattern and are positioned generally at the base of the turbidites.
 3476 Correlated turbidites are designated with T-, and correspond to the green tie lines, beginning with
 3477 the most recent turbidite (T-1, 2004). Orange correlation tie lines show correlations of strata that
 3478 are either sedimentary layers within turbidites or turbidites that do not have numbers. The
 3479 complete correlation diagram with all cores and turbidite classification is shown in Supplemental
 3480 File S3. Model ages are presented for T-1 in cores 102MC and 96PC (Fig. 7; Table 3). **[[4 digit**

3481 **numbers should not have commas; 14 in 14C should be superscript. “Appendix S 3” in**
 3482 **figure should be “Supplemental File S3”; “g/cc” should be g/cm³.]** 


3483

3484 Figure 9. Geophysical flattening process is displayed for some correlated turbidites. Geophysical
 3485 traces are plotted as in Figure 8. Each turbidite sequence has three panels with different core
 3486 configurations [left to right: gamma density, CT (computed tomographic X-ray) density, RGB
 3487 (red-green-blue) imagery, CT imagery, point magnetic susceptibility (Mag. Sus.), and ¹⁴C ages
 3488 with 95.4% error]. (i) Vertically true scale of core data. (ii) Geophysical data are flattened to
 3489 stratigraphic contacts. Green correlation tie lines are aligned at the general base of the turbidites
 3490 and designate correlation confidence with line thickness and pattern. (A) Turbidites T-3–T-5 are
 3491 correlated between cores 105, 104, 103, and 96. Core data are flattened to core 96. (B) Turbidites
 3492 T-6–T-8 are correlated between cores 105, 104, 103, and 96. Core data are flattened to core 104.
 3493 (C) Turbidites T-9–T-20 are correlated between cores 105, 104, and 103. Core data are
 3494 flattened to core 105. **[[A, B labels should be T-3–T-5 and T-6–T-8 (not, e.g., “T-3-5”).**

3495 **Should core numbers have PC, TC, etc., suffix? In figure, yrs should be yr; 4 number dates**
 3496 **in figure should not have commas; 14 in 14C should be superscript]** 


3497

3498 Figure 10. Turbidite T-21 is correlated between cores 108PC, 105PC, 104PC, 103PC, and 96
 3499 **[[do not see core 96 in figure?]]** using the same configuration as Figure 8. This sedimentary
 3500 sequence has **panels** **[[only 2 panels, not 3?]]** with different core configurations. **Dates are in**
 3501 **calendar years before present (A.D. 1950). [[correct, or calibrated?]]** (i) Vertically true scale of
 3502 core data [left to right: gamma density, CT (computed tomographic X-ray) density, RGB (red-
 3503 green-blue) imagery, CT imagery, point magnetic susceptibility (Mag Sus), and ¹⁴C ages with

3504 95% error]. (ii) Geophysical property data are flattened (scaled vertically) to stratigraphic
 3505 contacts. Core data are flattened to core 105PC. The green correlation tie line designates the base
 3506 of T-21. **[[4 number dates in figure should not have commas]]** 

3507

3508 Figure 11. Earthquake chronology. Space-time relations for stratigraphy cored in the 2004
 3509 rupture region are plotted (versus forearc distance, from the India-Indonesia border) as blue
 3510 circles with 95.4% error bars. Green tie lines show stratigraphic correlations (solid—correlation
 3511 more certain, dashed—less certain). Region-wide events are designated by a horizontal dotted
 3512 gray line and labeled with median ages on the left margin, along with the sequence age as gray
 3513 squares with 95.4% error bars. Red x symbols designate correlated turbidites that lack ¹⁴C age
 3514 control. Terrestrial paleoseismic and paleotsunami data are plotted (see legend). Site locations
 3515 are listed at the top of the plot. Data plotted to the left of core 108PC are not plotted versus
 3516 forearc distance as they are farther north than the extent of the coring investigation. The 2004
 3517 earthquake extent, labeled with a green arrow, extends beyond the northern latitudinal extent
 3518 shown in this figure (Chlieh et al., 2007). See Supplemental Files S2 and S4 for more detailed
 3519 radiocarbon age discussions and presentations. Coral microatoll ages (Meltzner et al., 2010,
 3520 2012) are concatenated into two groups, N. and S. Simeulue; this evidence comprises multiple
 3521 sites (Fig. 1; Supplemental File S1). **[[Dates with 4 numbers should not have commas.**

3522 **Spacing and punctuation in legends needs cleaning (e.g., “et.” (in et al.) should not have**
 3523 **period, and no comma after name and before et al. Inconsistent abbreviations (yrs instead**
 3524 **of yr)]]** 

3525

3526 Figure 12. Downcore recurrence intervals (RI) are determined by dividing the time between
3527 turbidites by the span of turbidites that time represents (Table 8). The 95.4% error is plotted as
3528 vertical error bars. The RI is plotted in a different color for each core. (A) RI is plotted versus
3529 regional turbidite number. (B) RI is plotted versus age in calendar yr before present (A.D. 1950).

3530 **[[BP on bottom axis should be B.P.]]** 

3531

3532 Figure 13. RR0705 and SO-002 core **map**; cores are plotted in orange and yellow in relation to
3533 slip regions for historic earthquakes (Bilham, 2005; Malik et al., 2011) plotted in Figure 1. **[[add**

3534 **definitions of core suffixes, i.e., PC, TC, etc.??]]** 